A Study of High-speed GaAs CCDs and Their Potential Application as an Imager

by

SHENGLI HU
M. Eng,, University of Electronic Science and Technology of Chian, 1994
B. E., Xi'an Jiaotong University, 1991

A Thesis Submitted in Partial Fulfillment of the
Requirements for the Degree of

MASTER OF APPLIED SCIENCE

in the Department of Electrical and Computer Engineering

We accept this thesis as conforming to the required standard

[redacted]

Dr. H. H. L. Kwok, Supervisor, Dept. of Electrical and Computer Engineering

[redacted]

Dr. D. Shpak, Member, Dept. of Electrical and Computer Engineering

[redacted]

Dr. M. Serra, Outside Member, Dept. of Computer Science

[redacted]

Dr. S. Dost, External Member, Dept. of Mechanical Engineering

UNIVERSITY OF VICTORIA

Supervisor: Dr. Harry H. L. Kwok

ABSTRACT

The research work in this thesis is divided into two parts. The first part is on the modeling and testing of GaAs RGCCDs (resistive-gate charge-coupled devices), which is a part of a research collaboration between TRIUMF and the University of Victoria. The second part is a project on the design of a prototype GaAs RGCCD compression circuit for use in imagery.

The research on GaAs RGCCDs in this thesis primarily focuses on the modeling of the charge transfer properties of the device, the testing of the electrical and optical properties of the device, as well as noise and non-linearity analysis of the output circuit of the CCD. On the modeling side, an equivalent circuit model for GaAs RGCCD [21] was developed and it allowed us to study the transient effects of the pixel size using SPICE type simulator. On the testing side, the electrical and optical properties were measured and a model was proposed to explain the measurement results. Three output circuits for the CCD were compared. Methods to reduce the non-linearity were studied.

The second part of the research is on the design of a prototype compression circuit for a CCD imager. CCDs were used to capture the image data as well as for data storage in the form of an analog memory. This circuit uses the conditional replenishment method to reduce the data captured by the CCD imager. The potential applications of this circuit are in high speed imaging, such as high frame-rate image sensing and high-resolution image sensing.

Examiners:

[redacted]

Dr. H H. L. Kwok, Supervisor, Dept. of Electrical and Computer Engineering

[redacted]

Dr. D. Shpak, Member, Dept. of Electrical and Computer Engineering

[redacted]

Dr. M. Serra, Outside Member, Dept. of Computer Science

[redacted]

Dr. S. Dost, External Examiner, Dept. of Mechanical Engineering

Table of Contents

List of Figures

List of Tables

Acknowledgments

I wish to express my profound gratitude to my supervisor, Dr. Harry H. L. Kwok, whose invaluable ideas, stimulating discussions, constant encouragement and unflagging support have guided this thesis research to its present state. The influence of his expertise can be seen throughout this work.

I would like to thank my supervisory committee, Dr. D. Shpak, Dr. M. Serra and Dr. S. Dost for the guidance and consultation that they provided throughout my research. Many thanks to Ms. Vicky Smith, Graduate Secretary of the Department, for making sure that the program was going through right procedure.

I would like to thank all my colleagues at CMC Lab, for their warm friendship and cooperation in numerous ways. It has been an enjoyable and academically valuable experience working in this wonderful lab.

I would like to thank Mr. J. Cresswell and Mr. R. Bula in TRIUMF for the help of GaAs CCDs fabrication and experimental setup.

I would also like to thank the computer and secretarial staff of the Department of Electrical and Computer Engineering for their assistance and technical support. Thanks to my friends for the help and encouragement.

Finally, I would like to extend my heart felt gratitude towards my parents who have always supported and encouraged me towards my goals. I express my love and appreciation to my wife, Minghong, for her support in spirit.

To
My Beloved Parents and Minghong

Chapter 1

Introduction

1.1 GaAs Semiconductor and MESFET Device

Gallium Arsenide (GaAs) is a III-V compound semiconductor which is particularly suited for high speed devices. The main reason is that GaAs has a very high intrinsic electron mobility in comparison with Silicon (Si). Room temperature electron mobility in GaAs is as high as $8500\ cm^2/v\text{-}s$ in comparison with a value of $1450\ cm^2/v\text{-}s$ in Si [1]. High electron mobility and high saturation velocity are usually required for high-speed device operation. Another advantage in using GaAs is the possibility to grow high resistivity semi-insulating (S.I.) GaAs. Semi-insulating GaAs is frequently used as the device substrate and this property makes it very suitable for the formation of a deep depletion region as required in X-ray detectors. Further more, it produces a very low parasitic capacitance. A low parasitic capacitance can give low AC power dissipation. The third superior property of GaAs is the existence of a large direct band gap which is essential for radiative recombination to occur. It also makes GaAs very useful in X-ray astronomy for the detection of X-ray with energy from *1 - 100 KeV*.

The first MEtal Semiconductor Field Effect Transistor (MESFET) using an epitaxial layer of GaAs on a semi-insulating GaAs substrate was fabricated by Hooper and Lehrer in 1967 [2]. Nowadays MESFET is the predominant device in the design of GaAs ICs for high-speed operation. In a GaAs MESFET, which the basic structure is shown in Figure 1.1, the active layer (channel) can be partially or totally depleted by the gate voltage and by the built-in voltage of the Schottky contact forming a gate. The isolation between the gate and channel, formed by the doped semiconductor material, is provided by the Schottky gate depletion layer that is controlled by the gate voltage. The gate voltage changes the width of the depletion region and, hence, the cross section of the conducting channel, modulating the electric current in the channel. The I-V characteristics of a GaAs MESFET are quite similar to those of the Si MOSFET, although the superior properties of GaAs combined with the removal of the oxide layer and a low threshold voltage give the GaAs MESFET marked advantages in speed, power consumption and radiation-tolerance over the Si MOSFET.

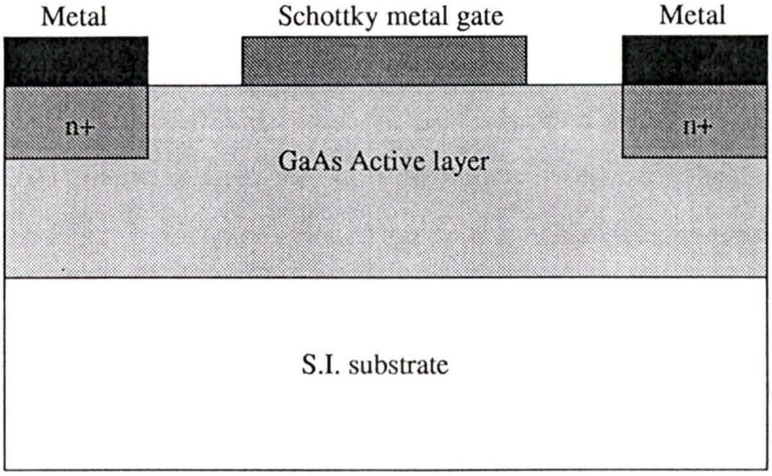

Figure 1.1 Basic GaAs MESFET structure

1.2 GaAs Charge-coupled Devices

The Charge-coupled Device (CCD) was first conceptualized by Boyle and Smith in 1970 at Bell Laboratories [3], and was experimentally verified using Si material, in the same year, by Amelio [4]. Basically, the CCD is a shift register or a delay line formed by a string of transport electrodes. An analog input signal introduced electrically or optically into the CCD can be stored in the form of charge packets in the potential wells under the CCD transport electrodes. Under the control of external voltages (clocks and bias voltages) applied to the transport electrodes, the potential wells, and hence the charge packets, can be shifted through the CCD channel. The charge packets are then detected at the output after they have sequentially passed through all the electrodes. Initially, CCDs were realized by MOS technology. In a MOS CCD, the electrodes are insulated from the semiconductor by a thin oxide layer and each electrode is a metal-insulator-semiconductor (MIS) capacitor. In 1972, the concept of Schottky-gate CCD using GaAs technology was suggested by Schuermeyer *et al* [5]. The transport electrodes of a GaAs CCD are reverse-biased metal-semiconductor Schottky diodes instead of MIS capacitance. It has been observed that a GaAs CCD inherently has low noise and a wide dynamic range due to the fact that the signal charge packets are stored and transferred in isolation in the depleted channel of the CCD, it also can operate in higher frequency due to the higher electron mobility in GaAs in comparison with Silicon [6][7][8].

In Schottky-gate GaAs CCD (also known as capacitive-gate CCD, CGCCD), the width of the interelectrode gaps is an important parameter. To avoid the formation of energy troughs in the channel under the interelectrode gaps, which can result in a significant reduction of the charge transfer efficiency (CTE), submicron gaps are required in the GaAs CGCCD [9]. This often requires more sophisticated processing steps and can cause the devices to break down easily. This problem is avoided if a suitable resistive material is used in the interelectrode gaps of the GaAs CCD, which is called resistive-gate CCD (RGCCD). The resistive material acts as a potential divider for the CCD resulting in a monotonic variation of the potential along the CCD transfer channel, this was demonstrated by Higgins, *et al.* [10][11], and Song and Fossum, *et al.* [12][13][14]. The GaAs RGCCD can work with wider interelectrode gaps and the requirement on the dimensional tolerance is relaxed, therefore it is easy to manufacture. Cermet is an insulator-metal composite containing SiO and Cr, it has a high resistance of up to mega-ohms per square and forms a low leakage Schottky contact to the GaAs. Therefore, cermet is used very frequently as the resistive-gate material in the GaAs RGCCD [15][16]. Figure 1.2 shows a basic GaAs RGCCD structure.

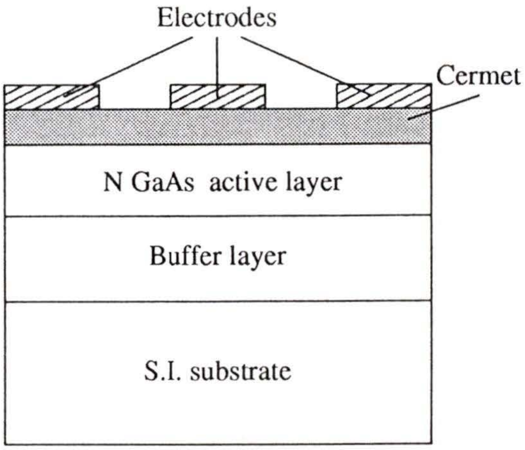

Figure 1.2 Basic GaAs RGCCD structure

1.3 Motivations

CCD is widely used in electronic systems, even though GaAs RGCCD has been less widely studied. GaAs RGCCD because of its higher absorption edge energy will likely to result in a higher absorption edge and less thermal noise for photon absorption in the visible range and the X-ray range. Also, GaAs is inherently more radiation resistant than Si [17][18]. This work examines some novel spectral measurements on the absorption properties of the GaAs RGCCD, and provides theoretical analysis of the photon interactions in the visible range and the X-ray range.

The CCD is inherently a low noise device, the main source of the noise comes from the CCD output circuit. There are three different charge sensing techniques commonly used in the CCD output circuit, and their effect on the performance of the CCD is quite important. It is necessary to examine the noise and non-linearity effects in the CCD output circuit and propose methods to reduce them.

For a high quality image, a large amount data captured by the CCD imager has to be transferred to other signal processing circuits in the electronic system. Based on the conditional replenishment method, a novel circuit used to compress the data from the CCD imager is presented.

1.4 Outline of the Thesis

The organization of this thesis is the following. Chapter 1 is the introduction, the motivation of this research and the outline of the thesis are presented.

Chapter 2 presents an equivalent circuit model for the GaAs RGCCD. Simulation results on the charge transfer efficiency (CTE) based on the CCD equivalent circuit are given.

Chapter 3 illustrates the experimental setup for the measurement of the GaAs RGCCD. The measurement results are discussed and explanations are given.

Chapter 4 analyzes the GaAs GGCCD as an X-ray detector. The interactions of X-ray with GaAs RGCCD is discussed. Theoretical analyses of the performance, quantum efficiency, charge splitting events, and noise of the GaAs RGCCD X-ray detector are presented.

Chapter 5 compares the three different charge sensing techniques in a CCD. The performance of the charge sensing techniques is evaluated.

Chapter 6 proposes a novel data compression circuit for the CCD. Circuit design, analysis and simulation are discussed. System simulation results are presented.

Chapter 7 discusses possible work that could be done in the future and makes conclusions.

Chapter 2

Operation and Modeling of GaAs RGCCD

2.1 Introduction

Functionally, CCD is similar to an analog shift-register. An analog input signal introduced electrically or optically into the CCD can be stored in the form of charge packets in the potential wells under the CCD electrodes. It consists of an input section, a string of transport electrodes and an output section. In order to transfer charge packets from under one electrode to the next, a set of clocks and bias voltages applied to the electrodes are required. The clocks can be either four-phase, three-phase, two-phase or uni-phase. In the early stage of CCD development, most of the CCD used three-phase clock [19]. It is sometimes favorable to use uni-phase CCD in specific applications. In general, the smaller the number of clock phases, the less the complexity of the clock driving circuit. In this chapter, the operation of an uni-phase GaAs RGCCD is described. An equivalent circuit model of the GaAs RGCCD is discussed. The simulation results of the GaAs RGCCD using SPICE equivalent circuit is also presented.

2.2 Operation of an Uni-phase GaAs RGCCD

A cross-sectional view of an uni-phase GaAs RGCCD is shown in Figure 2.1. The GaAs RGCCD has a N-type GaAs active layer (channel) and a semi-insulating GaAs substrate. The operation of the GaAs RGCCD can be explained with the aid of Figure 2.2, which shows the different clock waveforms, bias voltages and output signal. The clock Φ_1 and Φ_{1A} have voltage levels of $0/-4$ V and $1/-3$ V respectively, and Bias 1 and Bias 2 are set at -2 V and -1 V respectively. These clocks and bias voltages are required to transfer signal charge packets in the channel to the CCD output.

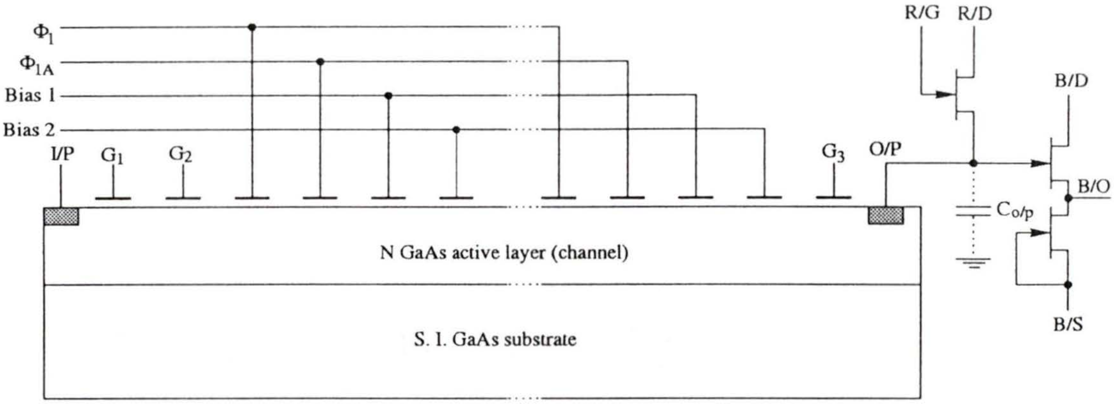

Figure 2.1 Cross-sectional view of an uni-phase GaAs RGCCD

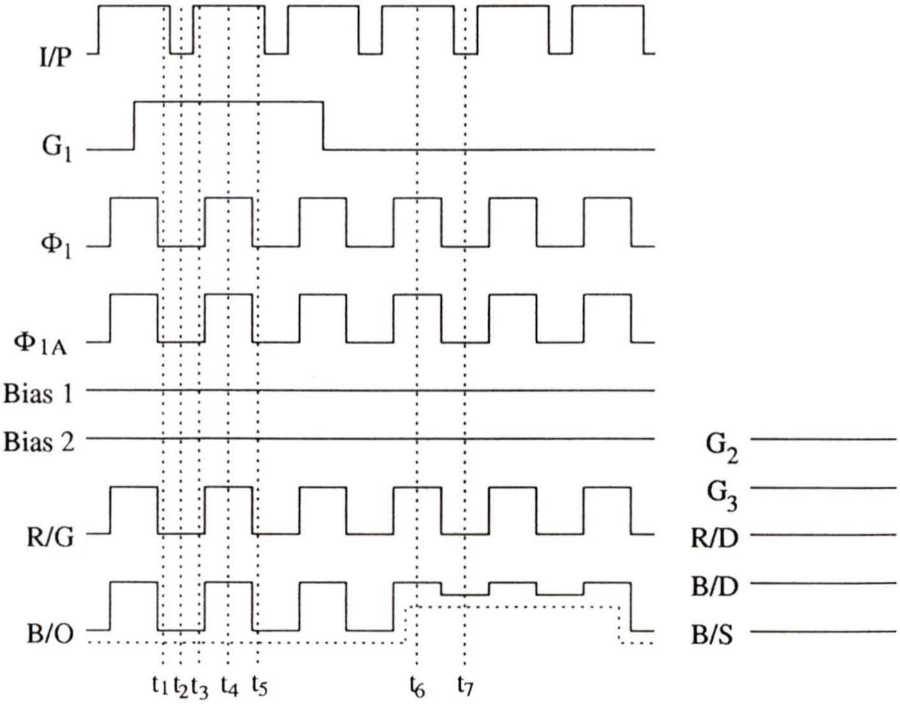

Figure 2.2 Clock waveforms, bias voltage and output signal for the device shown in Figure 2.1

The input signal V_{in} applied to the electrode G_1 is converted to a charge packet using a fill-and-spill method. This method has been widely used in CCD input section due to its advantages of low-noise and better conversion linearity [20]. Besides the input signal V_{in} applied to G_1, a reference voltage V_{ref} is applied to the electrode G_2, and an input sampling pulse $V_{I/P}$ to the input ohmic contact. Figure 2.3 shows the detail of this charge-injection scheme. The different times appearing in Figure 2.3 to Figure 2.5 correspond to those appearing in Figure 2.2. At $t = t_1$, $V_{I/P}$ is high and Φ_1 is low. Thus, the region in the active region extending from the right-hand edge of the input ohmic contact to the left-hand edge of G_2 is depleted of electrons. At $t = t_2$, $V_{I/P}$ is lowered to a voltage between the potentials under G_1 and the first transport electrode Φ_1. This causes the thermally-generated electrons to flow into and fill the potential well under G_2 from the input ohmic contact. At $t = t_3$, $V_{I/P}$ is returned to a high voltage and the electrons under G_1 as well as the excess electrons under G_2 is removed from the active region (channel) through the input ohmic contact. This creates a well-defined charge packet consisting of electrons under G_2. The size of the charge packet is proportional to $V_{ref} - V_{in}$ [20].

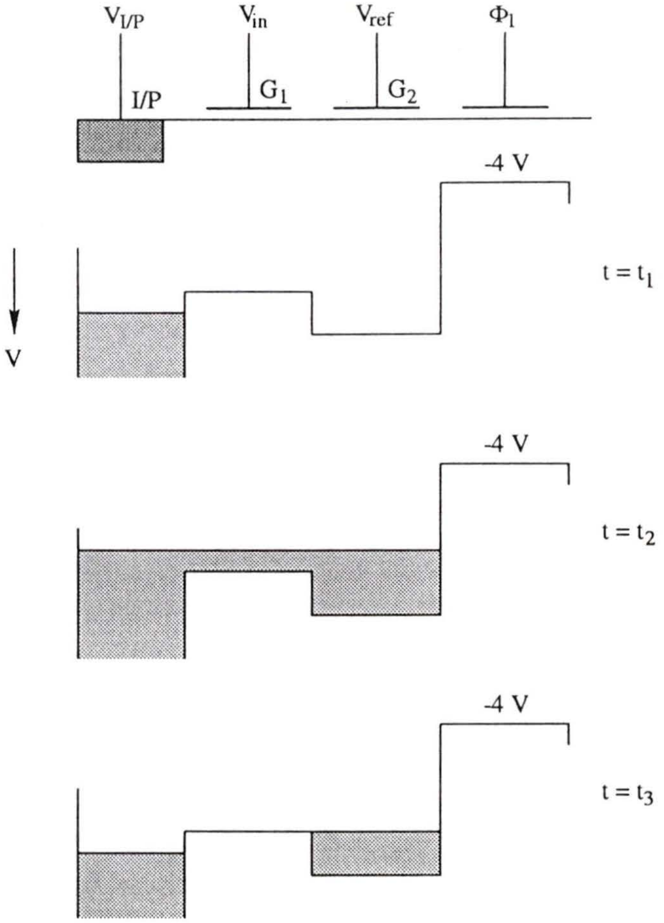

Figure 2.3 Sketch of potential and charge distribution of the GaAs RGCCD for charge injection process

The charge packet residing in the potential well under electrode G_2 is transferred to the transport region during the positive cycle of clock Φ_1 and Φ_{1A} (0 V and +1 V respectively). Figure 2.4 shows the actual transfer of a charge packet across one pixel of the GaAs RGCCD. At $t = t_4$, the charge packet under G_2 moves to the potential well under the electrode Φ_{1A} where the voltage is the highest. At $t = t_5$, both clock Φ_1 and Φ_{1A} are at the low voltage levels (-4 V and -3 V respectively) and the charge packet under the electrode Φ_{1A} moves to the potential well under the electrode Bias 2. The direction of the charge transfer is determined by the direction of the electric field due to the voltages applied to the adjacent transport electrodes.

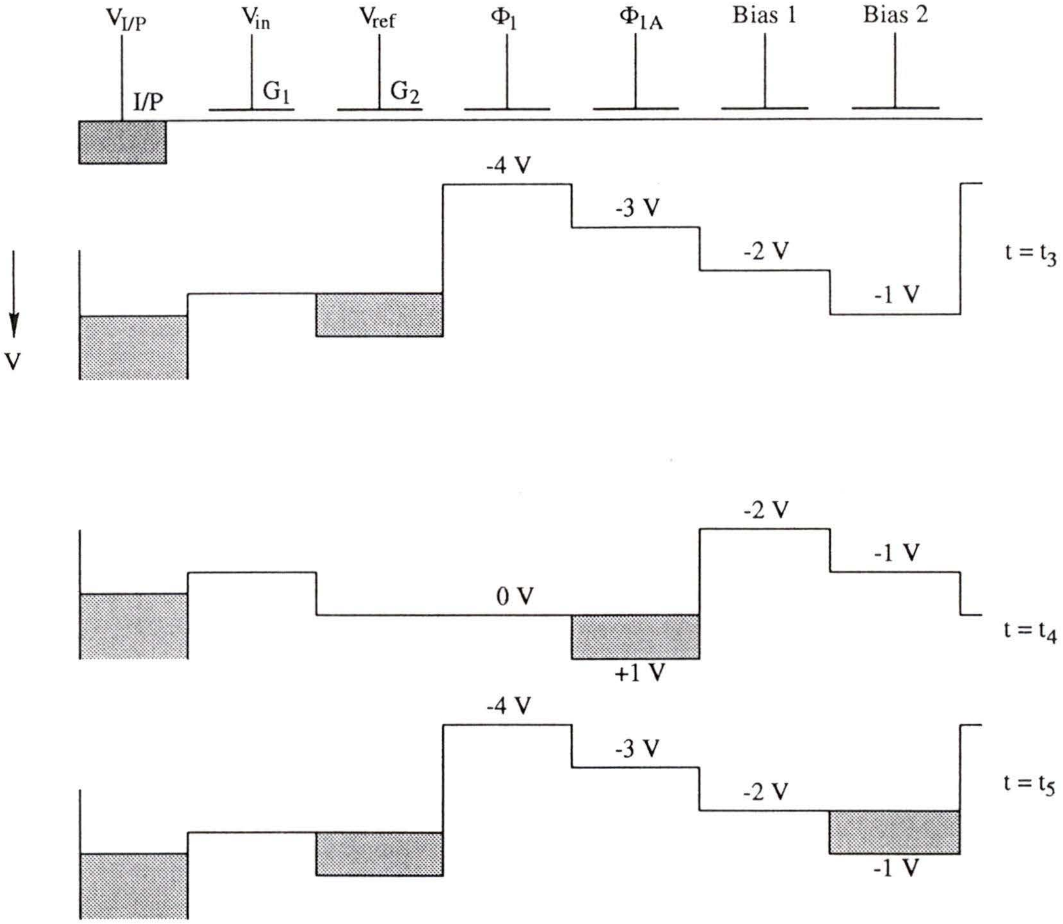

Figure 2.4 Sketch of potential and charge distribution of the GaAs RGCCD for charge transfer process

When the charge packet moves to the end of the CCD, it will be detected by the CCD output circuit. There are several ways to detect the charge packet. The details of CCD output circuit will be discussed in the Chapter 5. Here we only use the floating diffusion method as an example. Figure 2.5 shows the floating diffusion detection method. The charge packet transferred to the potential well under the final electrode Φ_{1A} moves into the output ohmic contact during the negative cycle of Φ_1 and Φ_{1A}. Prior to the charge detection, the output ohmic contact of the CCD is first reset to a high voltage by turning on the reset MESFET using the same voltage pulse as Φ_1 applied to R/G ($t = t_6$). The reset MESFET is disabled on the negative cycle of clock Φ_1 and Φ_{1A} causing the output contact to float at its reset level. At $t = t_7$, the electrons passing through the potential well under electrode G_3 exit the CCD through the floating output ohmic contact, charging the depletion capacitance Co/p and driving the output ohmic contact to a voltage negative with respect to its reset level. The signal produced at the output ohmic contact is then sent out by a MESFET source follower.

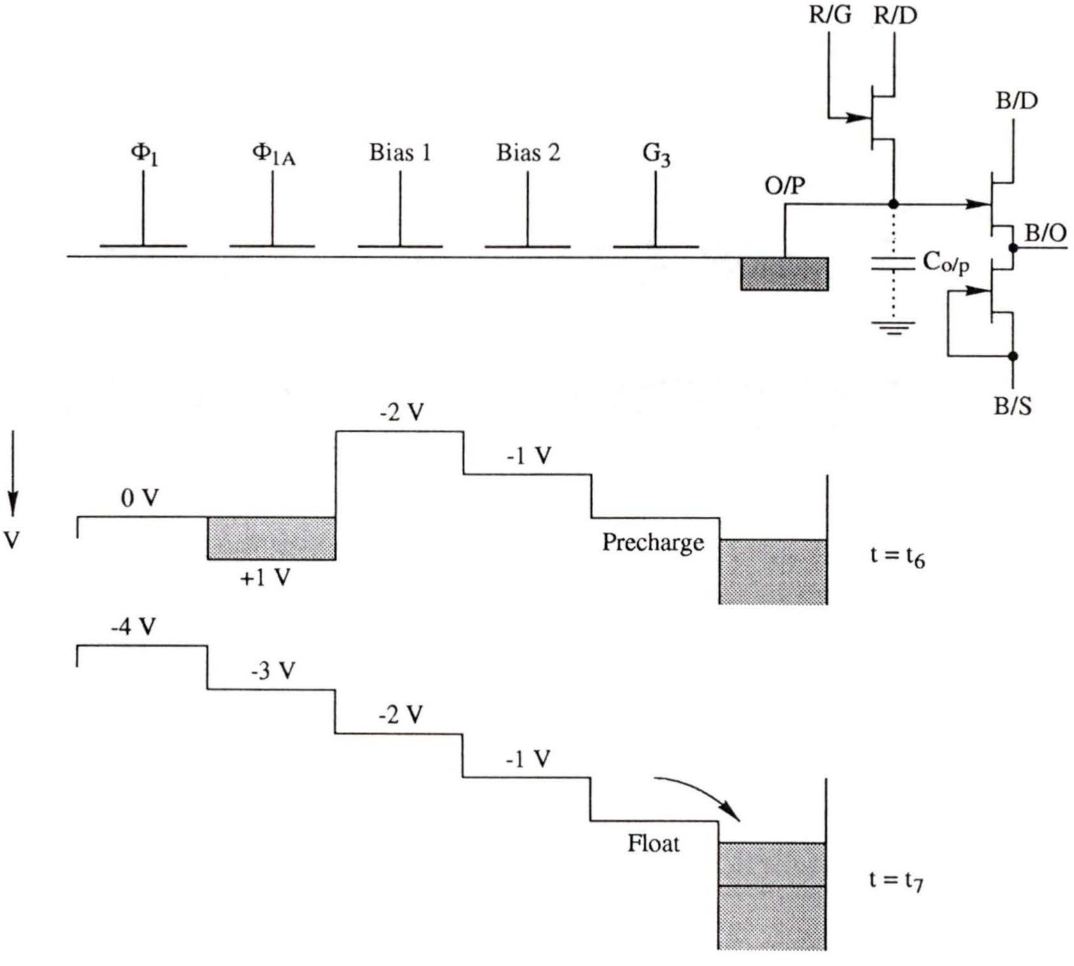

Figure 2.5 Sketch of potential and charge distribution of the GaAs RGCCD for floating diffusion charge detection scheme

If the CCD is to be used as an image sensor, the electrical input circuit is not needed. In this case the charge packets are generated by the light photon incident on the device. Thus, if the positive cycle of clock is halted for a short time, the optically generated charge packet will accumulate in the potential wells under the electrode Φ_{1A} at the rates proportional to the local light intensity. When the clock is subsequently resumed, the charge packets will be delivered to the output section.

2.3 An Equivalent Circuit for GaAs CCD

Unlike all other devices, the CCD can't be simulated using standard IC simulators. Thus an equivalent circuit model for the CCD has the advantage of being easily adaptable to usage in standard IC simulators, such as SPICE. The key elements of the CCD are the transport electrodes which can be modeled as distributed capacitors using the Poisson equation and Laplace equation. One can compute the response of the transportation of charge packets in the equivalent circuit of GaAs RGCCD. Charge packet transfer under the electrodes is facilitated by these current sources which are connected to these capacitors. Figure 2.6 shows a one-dimensional equivalent circuit model of an elemental cell of the GaAs RGCCD. The current sources were modeled to mimic the effects due to fringing field, diffusion and self-induced drift. Each pixel of the CCD is divided into a number of such elemental cells for computational purposes. These three current sources are given by the following equations [21]

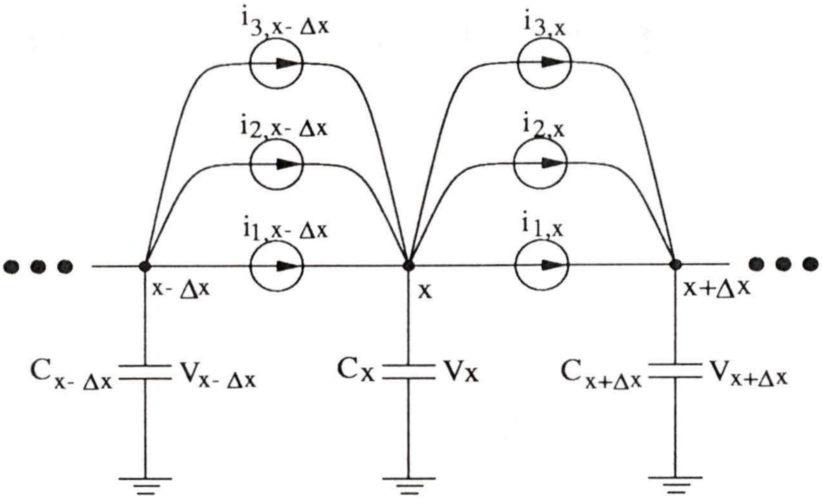

Figure 2.6 Equivalent circuit of an elemental cell of the GaAs CCD [21]

$$
\begin{aligned}
i_{1,x} &= \frac{v(E_f(x))}{\Delta x} Q_x && \text{under electrodes} \\
&= \frac{v(E_{applied})}{\Delta x} Q_x && \text{under gaps}
\end{aligned}
\tag{2.1}
$$

$$
\begin{aligned}
i_{2,x} &= \frac{D(E_f(x))}{\Delta x} (Q_x - Q_{x+\Delta x}) && \text{under electrodes} \\
&= \frac{D(E_{applied})}{\Delta x} (Q_x - Q_{x+\Delta x}) && \text{under gaps}
\end{aligned}
\tag{2.2}
$$

$$
\begin{aligned}
i_{3,x} &= \frac{\mu' V_x}{\Delta x^2} (Q_x - Q_{x+\Delta x}) && \text{under electrodes} \\
&= \frac{\mu' V_x}{\Delta x^2} (Q_x - Q_{x+\Delta x}) && \text{under gaps}
\end{aligned}
\tag{2.3}
$$

where Q_x is the charge stored at the position x, $E_f(x)$ is the fringing field at position x, $E_{applied}$ is the electric field under the electrode gaps, $v(E)$ is the field-dependent electron drift velocity, $D(E)$ is the field-dependent electron diffusivity, V_x is the voltage across the capacitor C_x, and μ' is the effective mobility of electrons which is given by

$$\mu' = \frac{v(E(x))}{E(x)} \tag{2.4}$$

The field-dependent electron drift velocity *v(E)* is given by

$$v(E) = \frac{\mu_0 E}{\sqrt{1+\left(\frac{\mu_0 E}{v_s}\right)^2}} \tag{2.5}$$

where

$$v_s = v_1 e^{-\frac{|E|}{E_1}} + \frac{v_2}{1+\left(\frac{|E|}{E_2}\right)^B} \tag{2.6}$$

The field-dependent electron diffusivity is given by

$$D(E) = D_0 + D_1 e^{-[\ln(|E|) - \ln(E_p)/\ln(A)]^2} \tag{2.7}$$

The proposed physical constants used in the above equations for a GaAs RGCCD are listed in Table 2.1 [22]

Table 2.1. Physical constants used in the equivalent circuit

Parameter	Unit	Value
v_1	cm/sec	4.77×10^7
v_2	cm/sec	3.24×10^7
E_1	V/cm	1644
E_2	V/cm	130.5
B		0.32
D_0	V/cm	129.5
D_1	cm^2/sec	312
E_p	V/cm	3394.8
A	V/cm	1.82
μ_0	cm^2/V-sec	5000

The capacitance C_x in Figure 2.6 is a charge-dependent capacitance which is given by [22]

$$C_x = \frac{C_0}{1-k_1 Q_x} \tag{2.8}$$

where $C_0 = \varepsilon_s w \Delta x / t$, and $k_1 = (q w \Delta x N_d t)^{-1}$. w is the width of the GaAs RGCCD channel, t is the thickness of the channel and N_d is the doping density of the channel. Since it is not easy to realize the charge-dependent capacitance in standard simulator such as SPICE, an equivalent circuit which is shown in Figure 2.7 is also needed to simulate the charge-dependent capacitance. The charge-dependent capacitor C_x with a terminal voltage V_x is associated with a charge $Q_x = C_x V_x$. Plugging Equation (2.8) into it and the terminal voltage V_x can be expressed

$$V_x = \frac{Q_x(1-k_1 Q_x)}{C_0} \tag{2.9}$$

To realized the charge-dependent capacitor C_x, a current meter (a zero-voltage source in Figure 2.7) is used to sense the current flowing into the capacitor. A voltage-controlled current source mimics the sensed current and feeds it to a test capacitor with a capacitance of one farad. A voltage-controlled voltage source given by Equation (2.9), with Q_x being replaced by the voltage across the 1 F capacitor, gives the terminal voltage of the charge-dependent capacitor.

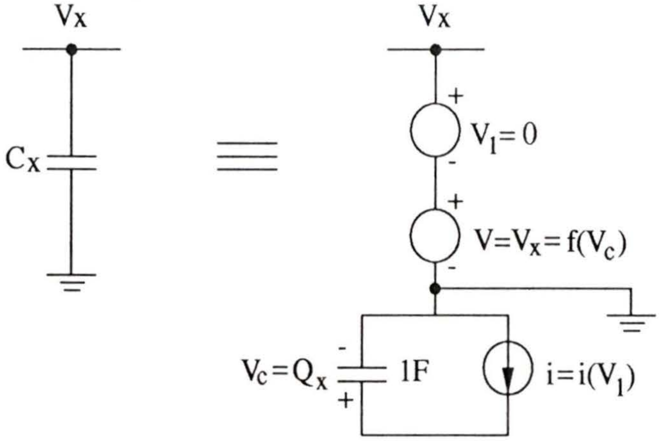

Figure 2.7 Equivalent circuit of the charge-dependent capacitance

The fringing field $E_f(x)$ under the kth electrode is given by [23]

$$E_f(x) = \frac{2\Delta V}{L} \sum_{n=1,\, n/3 \neq int}^{\infty} (-1)^{n+1}\left[\left(\sin\frac{n\pi L_g}{3L}\right) \Big/ \left(\frac{n\pi L_g}{3L}\right)\right] \cos\frac{2\pi n x}{L_l} \exp\left(\frac{2\pi n t}{3L}\right) \quad (2.10)$$

where ΔV is the voltage difference on the adjacent electrodes which is give by

$$\Delta V = \begin{cases} V_k - V_{k+1} & \text{for } E_f(x) \text{ under the left} - \text{half of the electrode} \\ V_{k+1} - V_k & \text{for } E_f(x) \text{ under the right} - \text{half of the electrode} \end{cases} \quad (2.11)$$

L_l is the transport electrode length, L_g is the gap length between the transport electrode, and $L = L_l + L_g$. The fringe field $E_f(x)$ can be easily realized using a nonlinear dependent source function in SPICE.

From the analysis above we can see, the equivalent circuit for CCD can be realized using a series nonlinear dependent source functions in SPICE. A SPICE code for the equivalent circuit model for an elemental cell of the CCD is given in Appendix A.

2.4 Simulation Results

A single uni-phase CCD pixel with different pixel size was simulated using equivalent circuits. The equivalent circuit model is distributed in nature and its accuracy will depend upon the grid spacing. I simulated different grid spacings and found when the grid spacing is 0.25 μm, the simulation results will give reasonably accurate results without using a large amount memory in the computer. Therefore the CCD pixel is simulated by a series of equivalent circuits (see Figure 2.6 and Figure 2.7) in which the size (Δx) is 0.25 μm in this study.

2.4.1 CTE versus Transfer Time

The simulation result of CTEs at different times during the charge transfer are listed in Table 2.2. The length of transport electrode is 3 μm and the gap between the electrodes is 3 μm, the total length of one CCD pixel is 24 μm. The peak area charge density Q_{peak} is $5 \times 10^{11}/\mathrm{cm}^2$. From the simulation results we can see, at the beginning, the CTE increases fast. But after 800 ps, the CTE increase less significantly. The reason for this is that near the end of the charge transfer, the self-induced drift of the electrons under the collecting electrode becomes significant. This will resist the rest charge packet flow due to the fringing field. Consequently, near the end of the charge transfer, the effective electric field is very small, and the charge transfer practically stops. Figure 2.8 is the simulation result of the charge packet transfer in CCD channel at $t = 1000\ \mathrm{ps}$.

Table 2.2. Transfer time versus CTE for uni-phase GaAs RGCCD

Transfer time (ps)	200	400	600	800	1000
CTE	0.7012	0.8643	0.9731	0.9943	0.9999

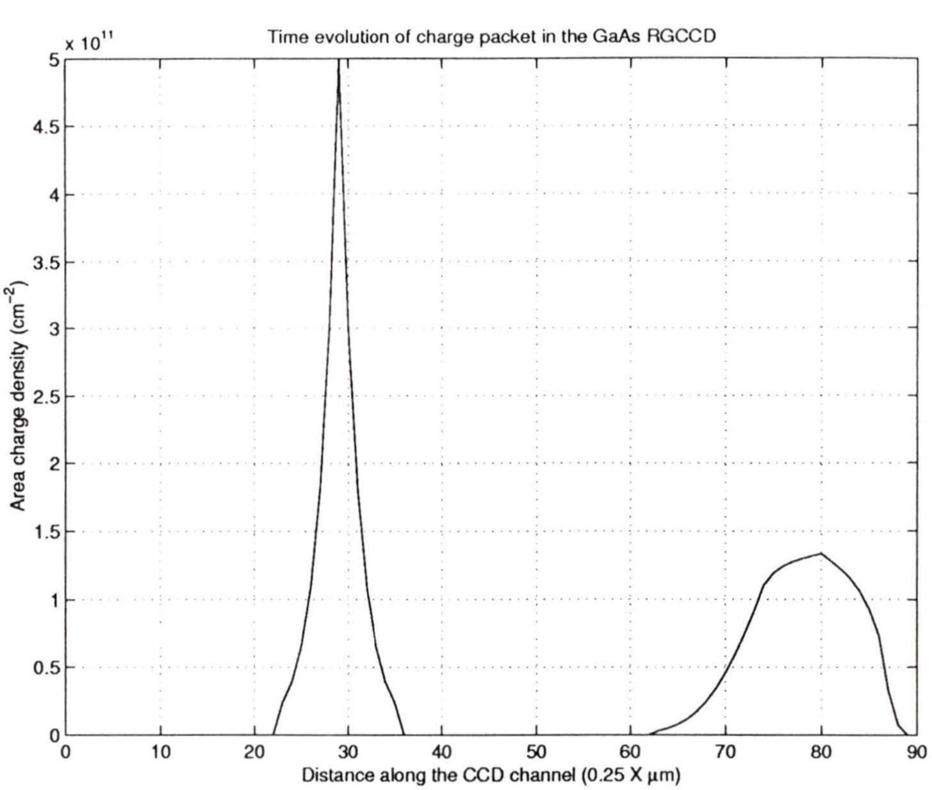

Figure 2.8 Time evolution of a one-dimensional charge packet in the GaAs RGCCD

2.4.2 CTE versus Pixel Size

To investigate how the different pixel sizes affect the CTE of the GaAs RGCCD, the time evolutions of the signal charge were simulated with different pixel sizes. The size of CCD pixel is very important for the GaAs RGCCD to be used as a X-ray detector since it influences the charge packet, which will be generated by the X-ray photons, splitting under the CCD (more detailed discussion for charge packet splitting for the GaAs RGCCD X-ray detector will be presented in Chapter 4). Some papers suggested that a large pixel size (i.e. large than 30 μm) will reduce the charge splitting in CCD for X-ray detector. But the simulation results using CCD equivalent circuit model show that a large pixel size will also reduce the CTE for the CCD and the operation speed of the CCD. Table 2.3 to Table 2.5 list the simulation results for different pixel size. For these tables, the gap between the electrodes is 3 μm and the length of electrode is 3 μm, 4 μm, and 5 μm respectively (the pixel size is 24 μm, 28 μm, and 32 μm respectively). Table 2.6 lists the simulation result when the pixel size is 60 μm, where the length of electrode is 10 μm and the gap between the electrode is 5 μm.

Table 2.3. Variation of the CTE with respect to the pixel size is 24 μm

Transfer time (ps)	200	400	600	800	1000
CTE	0.7012	0.8643	0.9731	0.9943	0.9999

Table 2.4. Variation of the CTE with respect to the pixel size is 28 μm

Transfer time (ps)	500	1000	1500	2000	3000
CTE	0.8840	0.9774	0.9881	0.9932	0.9981

Table 2.5. Variation of the CTE with respect to the pixel size is 32 μm

Transfer time (ps)	500	1000	2000	3000	4000
CTE	0.7174	0.9353	0.9842	0.9900	0.9907

Table 2.6. Variation of the CTE with respect to the pixel size is 60 μm

Transfer time (ps)	1000	2000	5000	7000	10000
CTE	0.7534	0.8679	0.9348	0.9830	0.9908

From the results in the above tables we can see that, for the larger pixel size, the CTE is smaller at the same operation speed. The reason is the change of the fringing field. It was noted that the fringing field under the emptying electrode largely determines the effectiveness of the charge transfer to the collecting electrode, and the difference of the pixel size makes an important contribution to the value of the fringing field. The larger pixel size, the smaller the fringing field under the emptying electrode. Therefore, the

CTE is smaller and charge packet will take a longer time to transfer. Table 2.7 lists the average fringing field (E_{fave}) under the emptying electrode for the different pixel size. Thus, considering the CTE and operation speed, the best size of the GaAs RGCCD pixel is 24 μm, this result is agree with the optimized result got by L. Chen [24].

Table 2.7. Average values of the fringing field under the emptying electrode

Pixel size (μm)	24	28	32	60
E_{fave} (V/cm)	464	365	302	109

Chapter 3

Measurement of GaAs RGCCD

3.1 Introduction

Two uni-phase GaAs RGCCDs (resistive gate charge coupled device), one having 128 pixels and other having 320 pixels, were fabricated at TRIUMF (Tri-University Meson Facility) using a GaAs process. Figure 3.1 shows the structure of the GaAs RGCCD. The input consists of an input ohmic contact and two Schottky barrier control gates (G_1 and G_2), which is used for electrical signal waveform sampling. Each CCD pixel in the transport region has four resistive gates (Φ_1, Φ_{1A}, Bias 1 and Bias 2) which store and transport the charge packets corresponding to the input signal. The output converts the charge packets to discrete voltage levels and it contains a Schottky barrier control gate (G_3), an output ohmic contact, a reset MESFET and an output MESFET source follower. The fabrication of the GaAs RGCCD required six mask layers, one for each of the following steps: ohmic contacts; proton isolation implants; resistive gates; Schottky gates; interconnect vias and interconnect metal. The main process parameters of the GaAs RGCCD are shown in Figure 3.1. The GaAs RGCCDs used in this study were originally used as transient digitizers [25]. The purpose of this study was to find the response of the GaAs RGCCD to electrical and optical signals. These devices were tested at room temperature at a clock frequency ranging from 1 MHz to 50 MHz. In this chapter, the setup of the experiment is briefly described, and the results are explained and discussed.

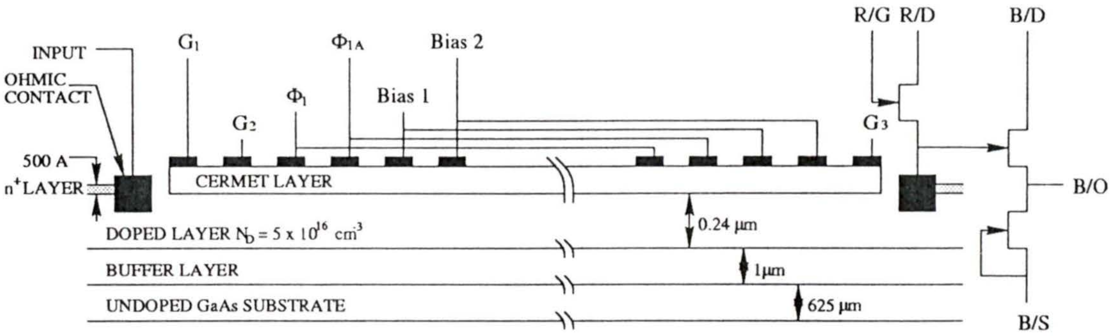

Figure 3.1 Cross-sectional view of the uni-phase GaAs RGCCD

3.2 Visible Light Interactions

The CCD was tested as an imager. When the potential wells are formed under CCD electrodes, incident light photons of a given wavelength will generate photo-excited carriers when the light photons are absorbed, the total number of which are proportional to the intensity and the time during which photons are incident. Absorption of light by a material is expressed in terms of the absorption coefficient $\alpha(h\nu)$, which is defined as the relative rates of decrease in radiant intensity, $I(h\nu)$, along its path of propagation, x. The mechanisms of absorption in the bulk regions of the semiconductor are fundamental in determining the magnitude of α but, whatever process is occurring at a given wavelength, λ, the magnitude of α is independent of the intensity $I(h\nu)$. Since α is a constant at any given wavelength, the intensity of the light, $I(x)$, passing through the absorbing medium is given by

$$I(x) = I_0 \exp(-\alpha x) \tag{3.1}$$

where I_0 is the intensity of the light just inside the semiconductor surface (*i.e.* $x = 0$). The total light absorbed by the medium is

$$I(x) = I_0(1 - \exp(-\alpha x)) \tag{3.2}$$

When incident light is absorbed in the GaAs RGCCD, photo-excited carriers are generated either by band-to-band transitions (intrinsic) or by transitions involving forbidden-gap energy levels which are generated by the impurity centers (extrinsic). This results in electrons collected in the potential well under the GaAs RGCCD electrodes. The processes of intrinsic and extrinsic photoexcitation of carriers are shown in Figure 3.2.

For the intrinsic process, the most important characteristic is the semiconductor's band-to-band energy gap since it determines the value of the longest wavelength of the incident light the material can absorb. The long wavelength cutoff in this case is given by[1]

$$\lambda_c = \frac{hc}{E_g} = \frac{1.24}{E_g(eV)} \qquad (\mu\mathrm{m}) \tag{3.3}$$

where λ_c is the longest wavelength corresponding to the semiconductor band-to-band energy gap E_g. When wavelengths is shorter than λ_c, the incident light photons will be absorbed by the semiconductor, and the electron-hole pairs will be generated in semiconductor. When wavelengths is longer than λ_c, the energy of incident light photons is not big enough and can't excite electrons from the valence band to the conduction band. Thus, no electron-hole pairs will be generated in semiconductor. For extrinsic absorption case, photoexcitation may occur between a band edge and an energy level within the energy gap. Carriers can be generated by the absorption of photons having energy equal to or greater than the energy separation of the bandgap levels and the conduction or valence band. In this case the long wavelength cutoff is determined by the depth of the forbidden-gap energy level, and it is longer than that for the intrinsic process.

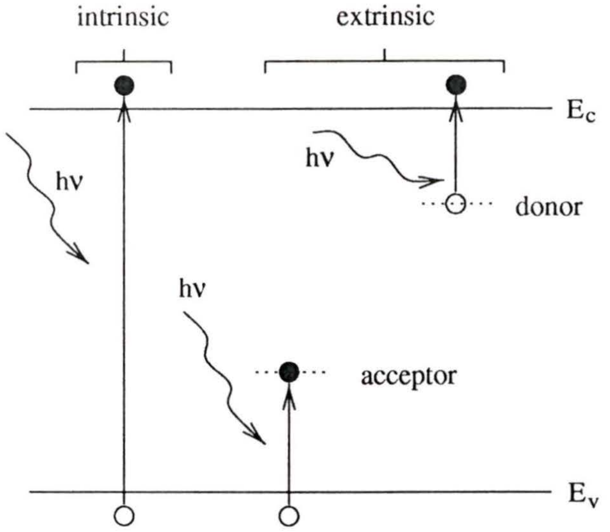

Figure 3.2 Process of intrinsic and extrinsic photoexcitation

3.3 Experimental Setup

Figure 3.3 shows the electrical test setup for the GaAs RGCCD. A HP 8131A 500 MHz signal-channel pulse generator and a HP 8130A 300 MHz dual-channel pulse generator were used to generate the clocks (ϕ1 and ϕ1A) and the input signal pulses. The clocks and input signals were synchronized by the pulse synchronizer. The output signals and input signals were measured by the Tektronix 2645 oscilloscope. The DC bias voltages and other required test signals used in this test were provided by the CCD test supporting system which was manufactured by TRIUMF. The value of signal levels and the DC bias voltages used for this GaAs RGCCD testing are listed in Table 3.1.

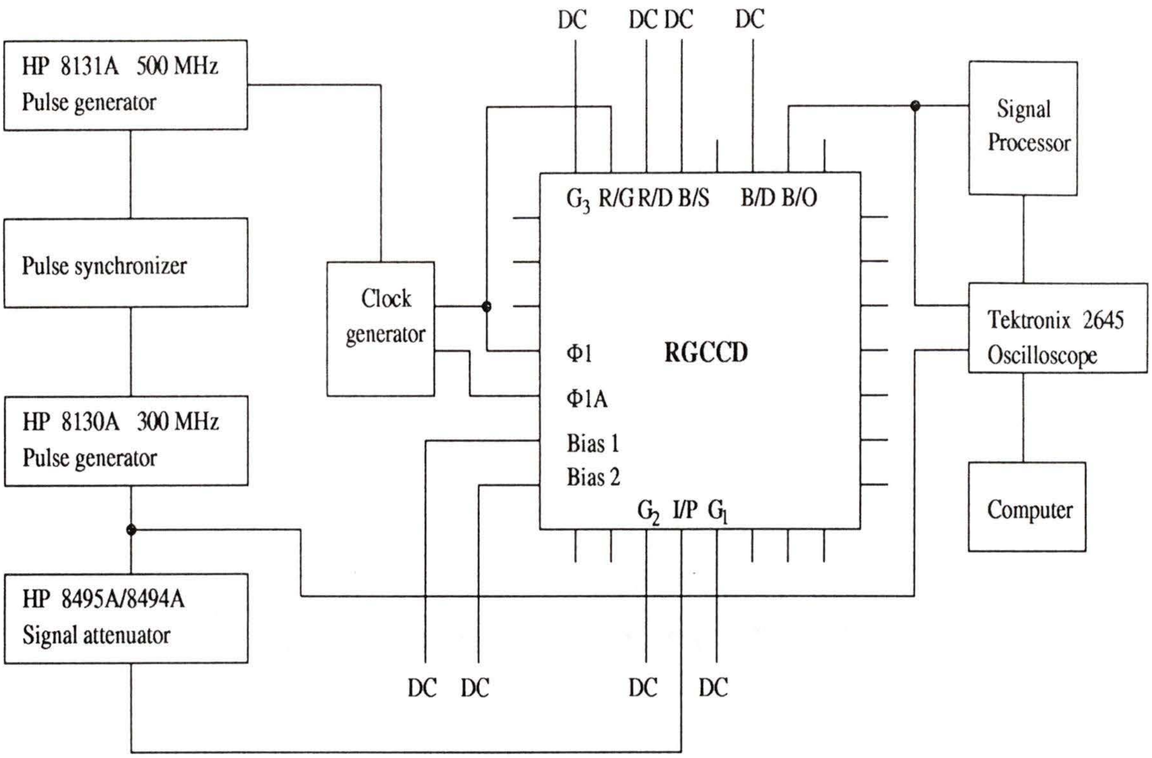

Figure 3.3 Block diagram of the RGCCD experimental setup

Table 3.1. Signal levels and DC bias voltages using for testing the RGCCD

Gate	Signal level (Volts)
ϕ_1	-4 to 0 (clock)
ϕ_{1A}	-3 to 1 (clock)
Bias 1	-2
Bias 2	-1
G_2	0
I/P	-2 to 1 (pulse)
G_1	input
B/D	4.5
B/S	-4.5
R/D	3
R/G	-4 to 0 (clock)
G_3	0

3.4 Electrical Test Results

The GaAs RGCCDs with 128 pixels and 320 pixels were tested at clock frequencies ranging from 1 MHz to 50 MHz by feeding its input (gate G1) with pulse signal. The measured input and output waveforms of the GaAs RGCCD are shown in Figure 3.4 and Figure 3.5 for 128 pixels and 320 pixels, respectively. The oscillograph display has the GaAs RGCCD input waveform along the bottom trace and the processed GaAs RGCCD output waveform along the upper trace. The pulse response of Figure 3.4 and Figure 3.5 shows the signal delay at the output. For example, the delay of output for the 128 pixel CCD and 320 pixel CCD at 20 MHz are 6.4 μs and 16 μs, respectively. These measurements agree very well with the theoretical calculations of the delay time of a

GaAs RGCCD which is given by:

$$t_{delay} = \frac{N_{pixel}}{f_c} \tag{3.4}$$

where N_{pixel} is the number of pixels of the GaAs RGCCD and f_c is the clock frequency of the transport gates.

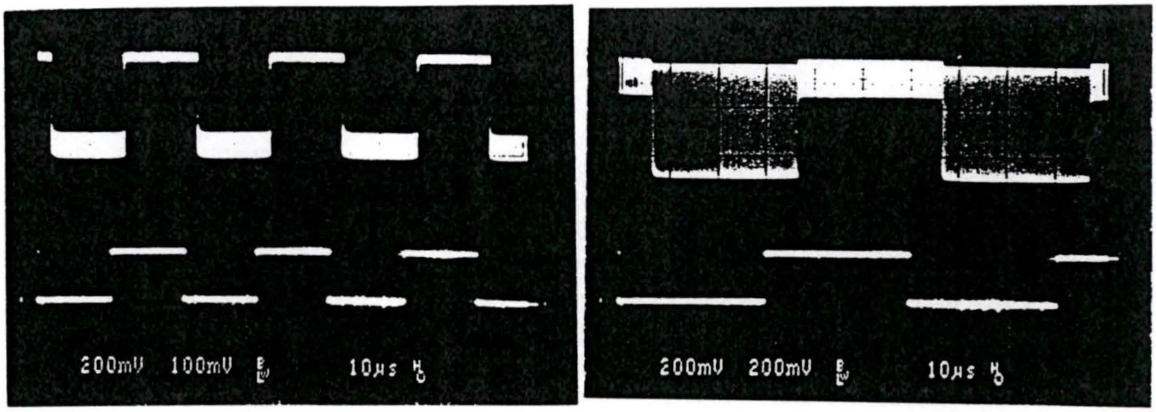

Figure 3.4 Oscillograph of the GaAs RGCCD with 128 pixel for 20 MHz (left) and 50 MHz (right) clock

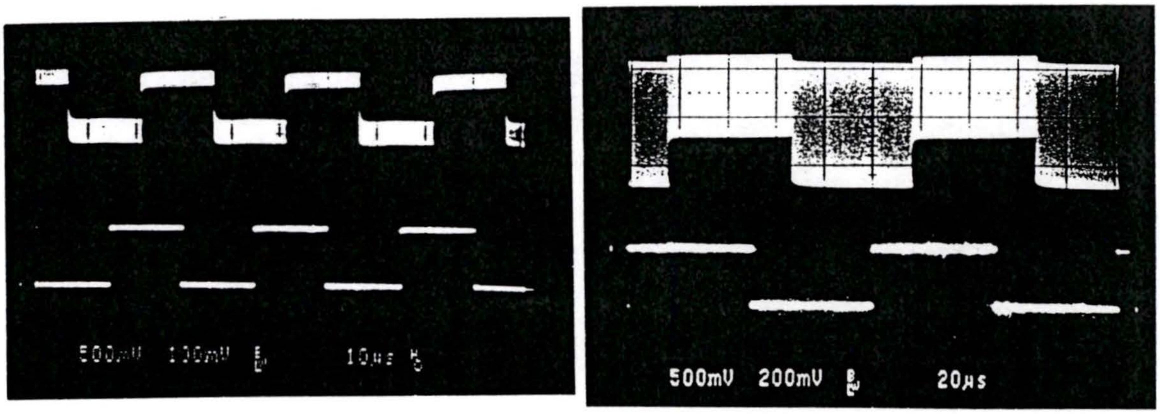

Figure 3.5 Oscillograph of the GaAs RGCCD with 320 pixel for 20 MHz (left) and 50 MHz (right) clock

A more detailed quantitative demonstration of the performance of the GaAs RGCCD is shown in Figure 3.6, where the waveforms of the input signal (upper), the output signal waveform and the clock waveform (lower) are displayed. The input signal is 5 MHz and the clock signal is 20 MHz.

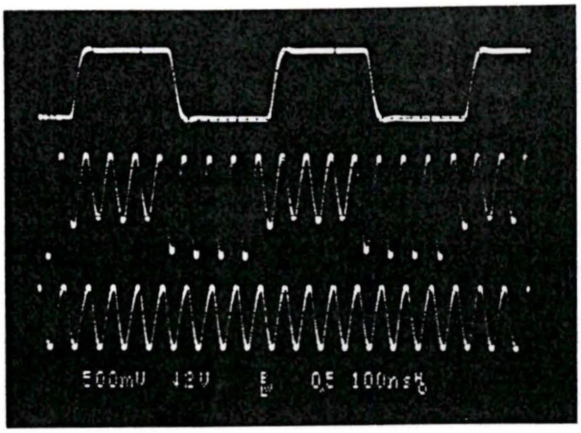

Figure 3.6 More detailed quantitative demonstration of the performance of the GaAs RGCCD

Figure 3.7 shows the oscillograph of the GaAs RGCCD for the linearity measurement, where the upper and lower traces display the output and input waveforms, respectively. By changing the amplitude of the input square waveform, we measured the amplitude of the output waveform in the negative cycle of the clock. The input-output relationship for both 128 pixels and 320 pixels RGCCDs are the same. Figure 3.8 shows the results of the 128 pixels RGCCD with different clock frequencies. The detailed discussion for the linearity of the GaAs RGCCD will be presented in Chapter 5.

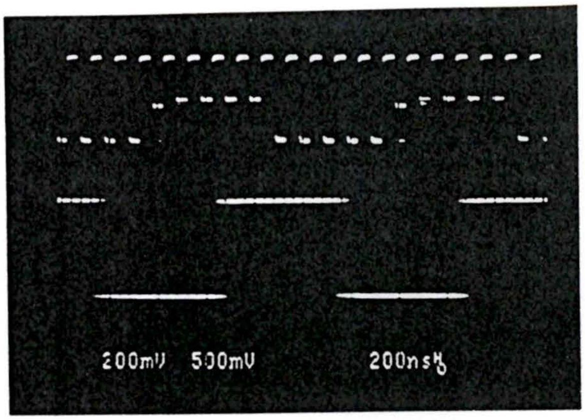

Figure 3.7 Oscillograph of the GaAs RGCCD for the linearity measurement

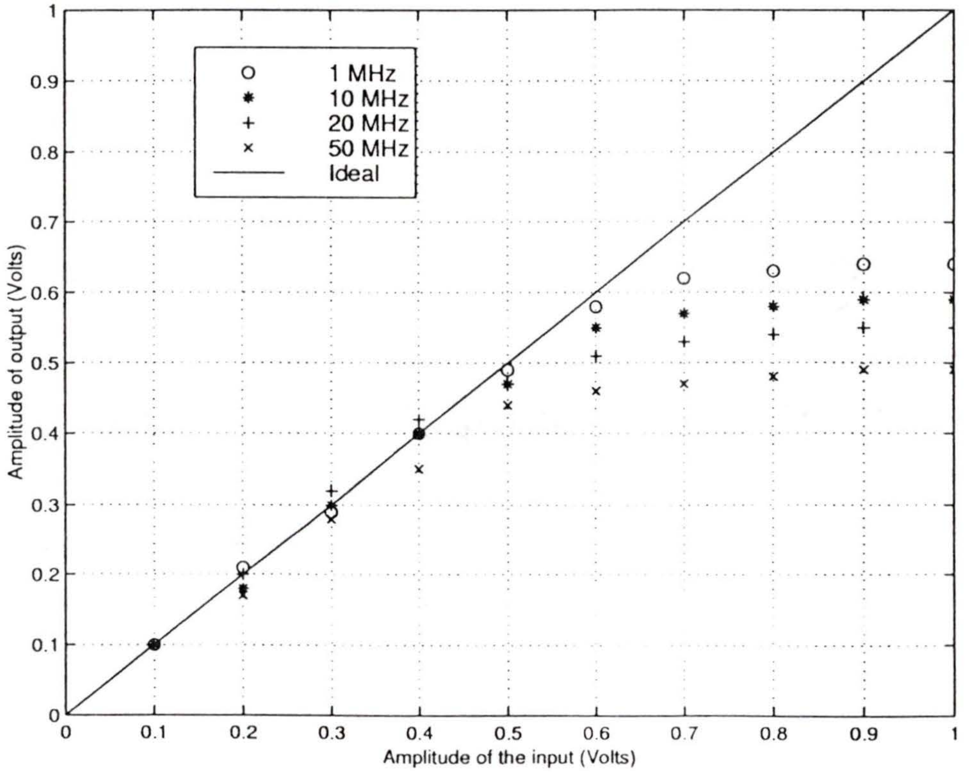

Figure 3.8 Measured linearity between the input and output of the RGCCD

3.5 Optical Test Results

Nowadays, CCDs dominate the scene for imaging processing [26][27][28]. Therefore it is of interest to investigate the optical characteristics of the GaAs RGCCD. The response of the GaAs RGCCD to white light and monochromatic light at room temperature were measured. Figure 3.9 and Figure 3.10 show the experimental setup for measuring the GaAs RGCCD response to white light and monochromatic light, respectively. The GaAs RGCCD measured here is the one with 128 pixels and the clock frequency is set to 20 MHz. The water bath is used to eliminate any heating effect due to IR absorption on the testing GaAs RGCCD. A monochromator was used to generate the light of specific wavelengths. Color filters were used to intercept and eliminate the harmonics which may come with the monochromator. Beam splitters (neural density filters) were used to uniformly reduce the intensity of the white light.

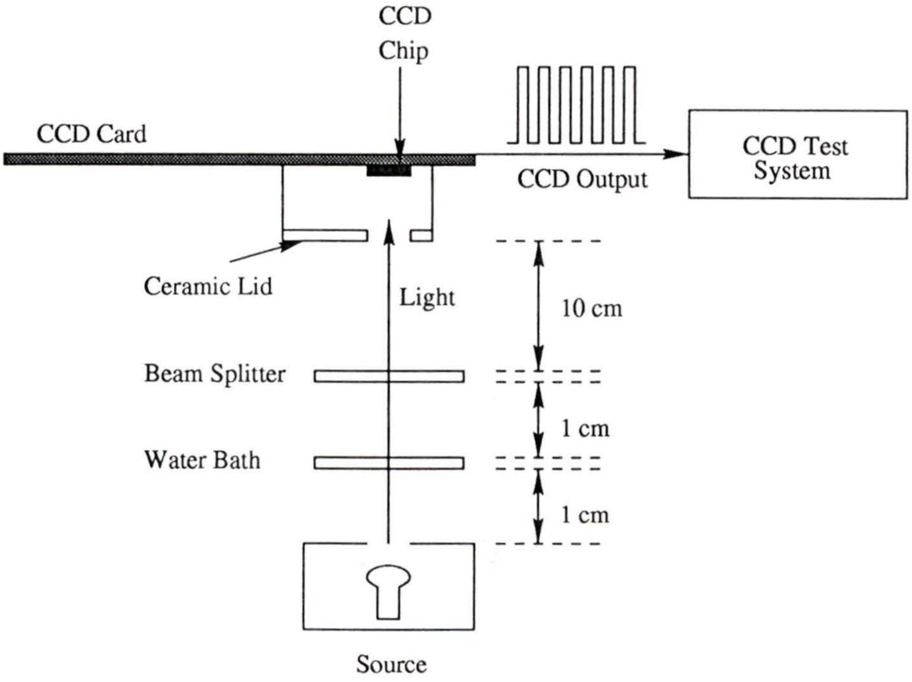

Figure 3.9 A schematic of the experimental setup used to study the white light spectra

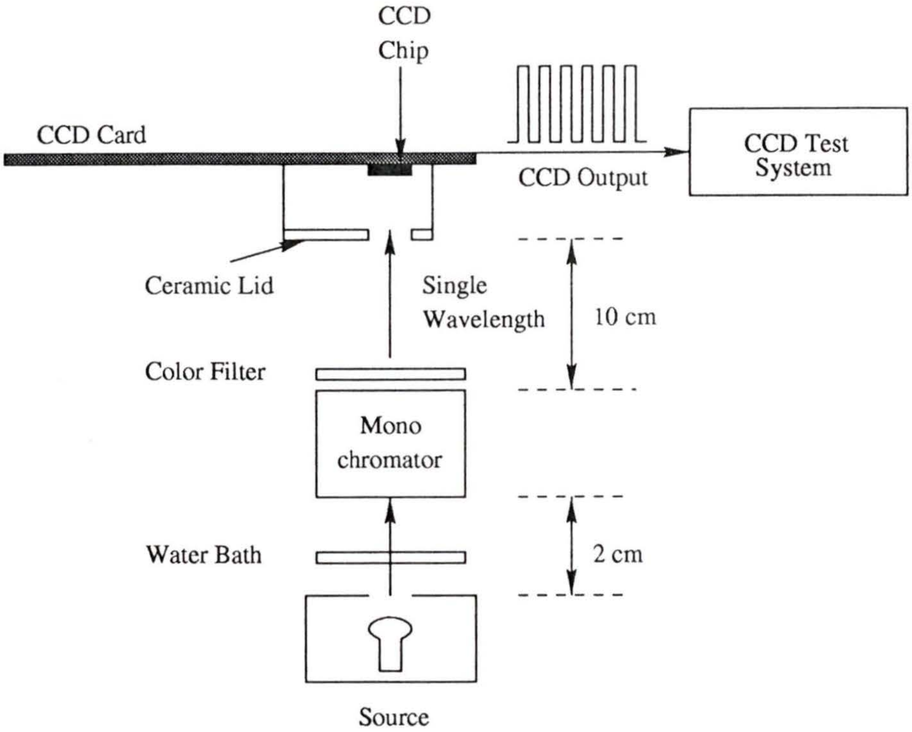

Figure 3.10 A schematic of the experimental setup used to study single wavelength light spectra

For the ideal semiconductor, when the incident light photon energy is greater than the semiconductor band-to-band energy gap E_g (*i.e.* 1.42 eV for GaAs), each photon produces one electron-hole pair (quantum efficiency is one). However, the absorption coefficient α is wavelength dependent and it decreases for longer wavelengths. This means that for the same amount of the absorbed photons, long wavelength light photons are absorbed deeper into the semiconductor than short wavelengths. Very long wavelength photons will pass through the CCD and not be absorbed. The long cutoff wavelength for intrinsic absorption can be calculated using Equation (3.3). For GaAs, the long cutoff wavelength is found to be 0.873 μm.

When the electron-hole pairs are generated by the incident light photons, the electrons must be collected in the potential well under the CCD electrodes before they recombine with each other and disappear. Thus, only the electrons generated within the depletion region have a chance to be collected in the potential well and contribute to the output. When the electrode of GaAs RGCCD has a 0 V bias, the depletion depth is about 4 μm from the surface of the doped active layer (*c.f.* Figure 3.1). Therefore it is safe to assume that all the electrons generated in active layer and buffer layer will be collected in the potential well and transferred to the output. The absorption coefficient of GaAs is obtained from [1] which is listed in Table 3.2

Table 3.2. Absorption coefficient of GaAs

wavelength	0.2 μm	0.3 μm	0.4 μm	0.5 μm	0.6 μm	0.7 μm	0.8 μm	0.85 μm
α (cm^{-1})	$1\text{x}10^6$	$9\text{x}10^5$	$8\text{x}10^5$	$1\text{x}10^5$	$3\text{x}10^4$	$1\text{x}10^4$	$7\text{x}10^3$	$4\text{x}10^2$

Using Equation (3.2) to calculate how many incident light photons were absorbed in the active layer and the buffer layer assuming each absorbed photon generates an electron hole pair, the quantum efficiency can be computed. Since our GaAs RGCCD is a front-side illuminated device and the electrodes consist of metal which is not transparent to light, the area of electrode and the area of the electrode gap is the same, only half of the incident light can pass into the active layer of the GaAs RGCCD. Therefore the peak quantum efficiency of this device is 50%. Figure 3.11 shows the ideal quantum efficiency for the GaAs RGCCD.

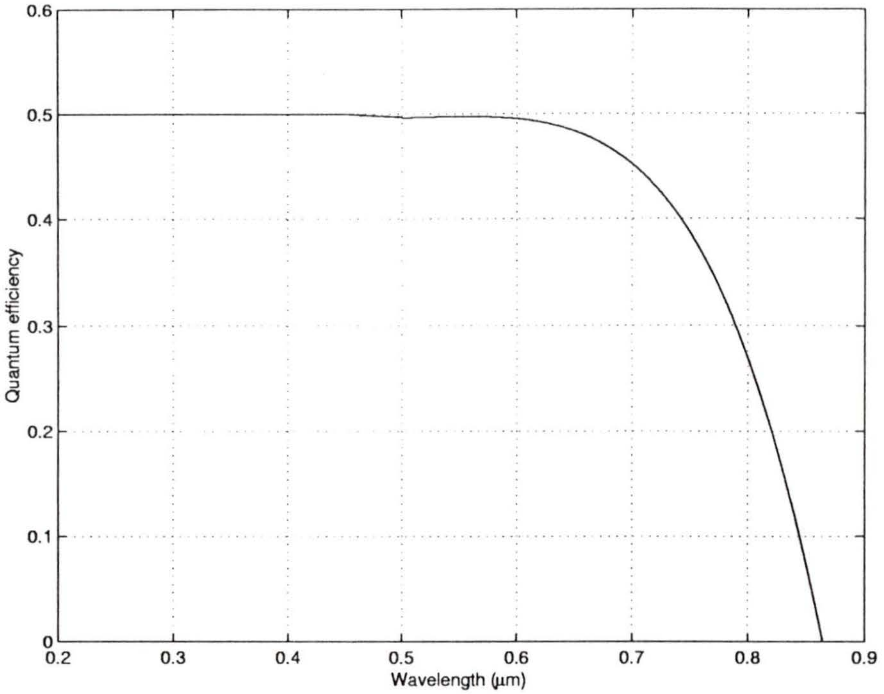

Figure 3.11 Theoretical quantum efficiency for the GaAs RGCCD

From Figure 3.11 we can see that the theoretical quantum efficiency decreases very quickly when the incident light wavelength is longer than 0.7 μm. When the wavelength is longer than 0.88 μm, the quantum efficiency becomes zero. Such an absorption tail generally agrees with the measurement result which is shown in Figure 3.12. The differential output voltage decreases when wavelength is longer than 0.7 μm is due to the GaAs intrinsic absorption. When the incident light wavelength is longer than the long cutoff wavelength, here is 0.873 μm for GaAs, there is no light absorption for the GaAs intrinsic process, thus the quantum efficiency goes to zero. For short wavelengths, the theoretical quantum efficiency is high and remains constant, but our measurement is not. In fact, the differential output voltage reduces when the wavelength is shorter. There are two possible explanations to this observation. Firstly, it may be due to surface recombination. To examine this, we propose a model for it. When a monochromatic light of wavelength λ is incident on the front surface of the GaAs RGCCD, the number of photo-excited carriers

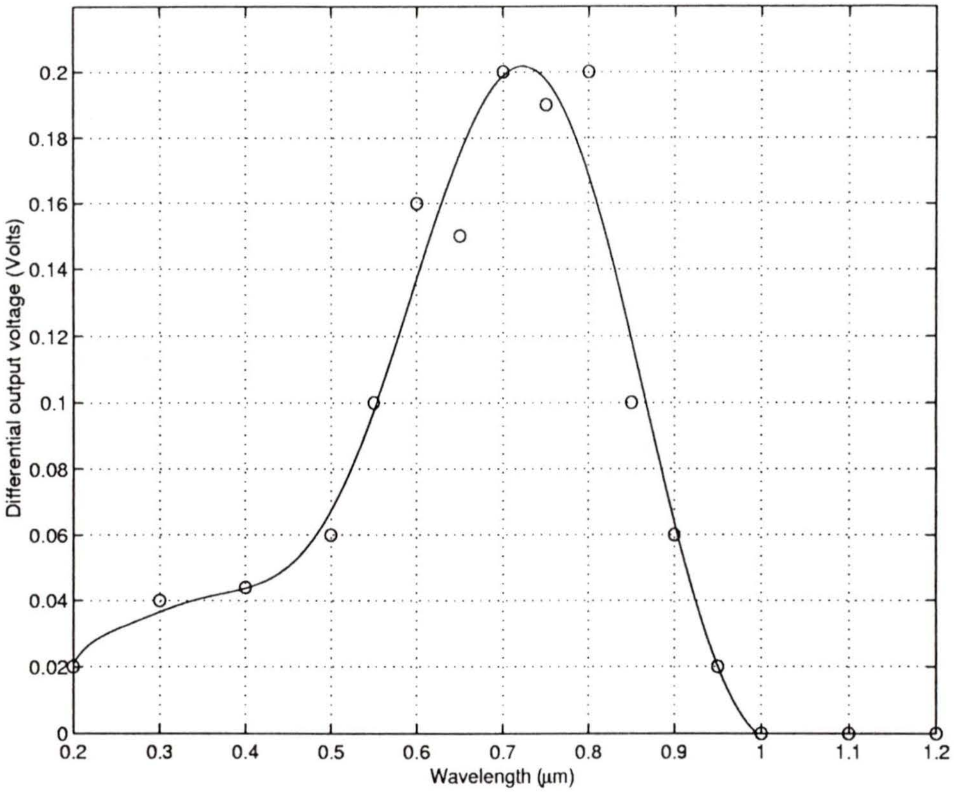

Figure 3.12 The measurement output voltage versus wavelength

collected in the potential wells under the electrodes can be derived as follows. If we do not consider the reflection at the semiconductor surface, the generation rate of electron hole pairs at the distance *x* from the surface is given by

$$G(\lambda, x) = \alpha(\lambda)F\exp[-\alpha(\lambda)x] \tag{3.5}$$

where $\alpha(\lambda)$ is the light absorption coefficient of the semiconductor, F is the number of incident photons/cm^2/s per unit bandwidth.

Under a low-injection condition, the one-dimensional, steady-state continuity equation for semiconductor is [1]

$$D_n \frac{d^2 n}{dx^2} + G - \frac{n - n_0}{\tau_n} = 0 \tag{3.6}$$

where D_n is the electron diffusion coefficient, n is the electron density, n_0 is the thermal-equilibrium electron density and τ_n is the electron lifetime in semiconductor which is [1]

$$\tau_n = \frac{1}{\sigma_n V_{th} N_t} \tag{3.7}$$

where σ_n is the cross section of electron, V_{th} is electron thermal velocity and N_t is the number of trapping centers/cm^3.

Inserting Equation (3.5) into Equation (3.6), the general solution for Equation (3.6) is

$$n - n_0 = A\cosh(x/L_n) + B\sinh(x/L_n) - \frac{\alpha F \tau_n}{\alpha^2 L_n^2 - 1} \exp(-\alpha x) \tag{3.8}$$

where $L_n = (D_n \tau_n)^{1/2}$ is the electron diffusion length. There are two boundary conditions. One is at the surface of the semiconductor, we have surface recombination with a recombination velocity S_n, that is:

$$D_n \frac{d(n - n_0)}{dx^2} = S_n(n - n_0) \qquad at \qquad x = 0 \tag{3.9}$$

where surface recombination velocity S_n is given by [30]

$$S_n = \sigma_n V_{th} N_{st} \tag{3.10}$$

where N_{st} is the number of surface trapping centers per unit area at the interface of the cermet and GaAs semiconductor. Using the parameter $V_{th} = 10^7 cm/s$, $N_{st} = 10^{12}/cm^2$, $N_t = 10^{18}/cm^3$ and assuming $\sigma_n = 10^{-11} cm^2$, the value of surface recombination velocity $S_n = 10^8 cm/s$ and the electron life time $\tau_n = 10^{-14} s$. The electron diffusion length $L_n = 5.48 \times 10^{-7} cm$ if we assume $D_n = 30 cm^2/s$. Thus, we can see that if $\alpha < 10^6 cm^{-1}$, $\alpha^2 L_n^2 \ll 1$.

Another boundary condition is at the edge of the depletion region. It can be simplified using $x = \infty$, the excess electron density is almost zero, that is:

$$n - n_0 \cong 0 \qquad at \qquad x = \infty \tag{3.11}$$

Using these two boundary conditions in Equation (3.8), the electron density is

$$\begin{aligned} n - n_0 &= A\cosh(x/L_n) - A\sinh(x/L_n) - \frac{\alpha F \tau_n}{\alpha^2 L_n^2 - 1}\exp(-\alpha x) \\ &= A\exp(x/L_n) - \frac{\alpha F \tau_n}{\alpha^2 L_n^2 - 1}\exp(-\alpha x) \end{aligned} \tag{3.12}$$

where the parameter A is calculated as follows:

$$A = \frac{\alpha F \tau_n}{\alpha^2 L_n^2 - 1} \frac{L_n(D_n \alpha + S_n)}{S_n L_n + D_n} \tag{3.13}$$

If we only consider the ideal situation without the surface recombination, *i.e.*, all the electrons generated by the incident light photons were collected in the potential wells in the CCD, that is $D_n = 0$ and $S_n = 0$, Equation (3.6) can be rewritten as

$$G - \frac{n - n_0}{\tau_n} = 0 \tag{3.14}$$

the solution for Equation (3.14) is

$$n - n_0 = \tau_n G = \alpha F \tau_n \exp(-\alpha x) \tag{3.15}$$

Integrating Equation (3.15) from $x = 0$ to ∞, the total number of the photo-excited carriers is equal to $F\tau_n$. On the other hand, we measured the output voltage of the GaAs RGCCD which is 0.2 V, the total capacitance is 71 fF, therefore the electron number collected in the potential is

$$n = \frac{0.2 \times 71 \times 10^{-15}}{1.6 \times 10^{-19}} = 88750 \tag{3.16}$$

therefore $F = 88750/\tau_n$.

Comparing Equation (3.15) with Equation (3.12), we can see that when $\alpha^2 L_n^2 \ll 1$, the second term on the right side of the Equation (3.12) is identical to the Equation (3.15), this means that the electron is generated without surface recombination. The first term on the right side of the Equation (3.12) is the influence of surface recombination. As we calculated above, the electron life time τ_n is 1×10^{-14} s, and if we assume that the electron effective diffusion coefficient at the GaAs semiconductor surface is 30 cm^2/s, then for different values of the surface recombination velocity S_n and the light absorption coefficient α, we can get the effect of the surface recombination to the quantum efficiency.

From Figure 3.13 and Figure 3.14 we can see that, when $S_n = 0$, *i.e.* without surface recombination, the solution for Equation (3.6) is very near to the solution for Equation (3.14) which is for the ideal situation (compare the dashed line and star line in both figures). When the absorption coefficient α is small, they are almost the same (*c.f.* Figure 3.13). When the surface recombination velocity $S_n = 10^8 cm/s$ (the solid line in both figures), we can see the electron concentration near the semiconductor surface is lower. As expected, when we have surface recombination, the number of electrons collected is reduced.

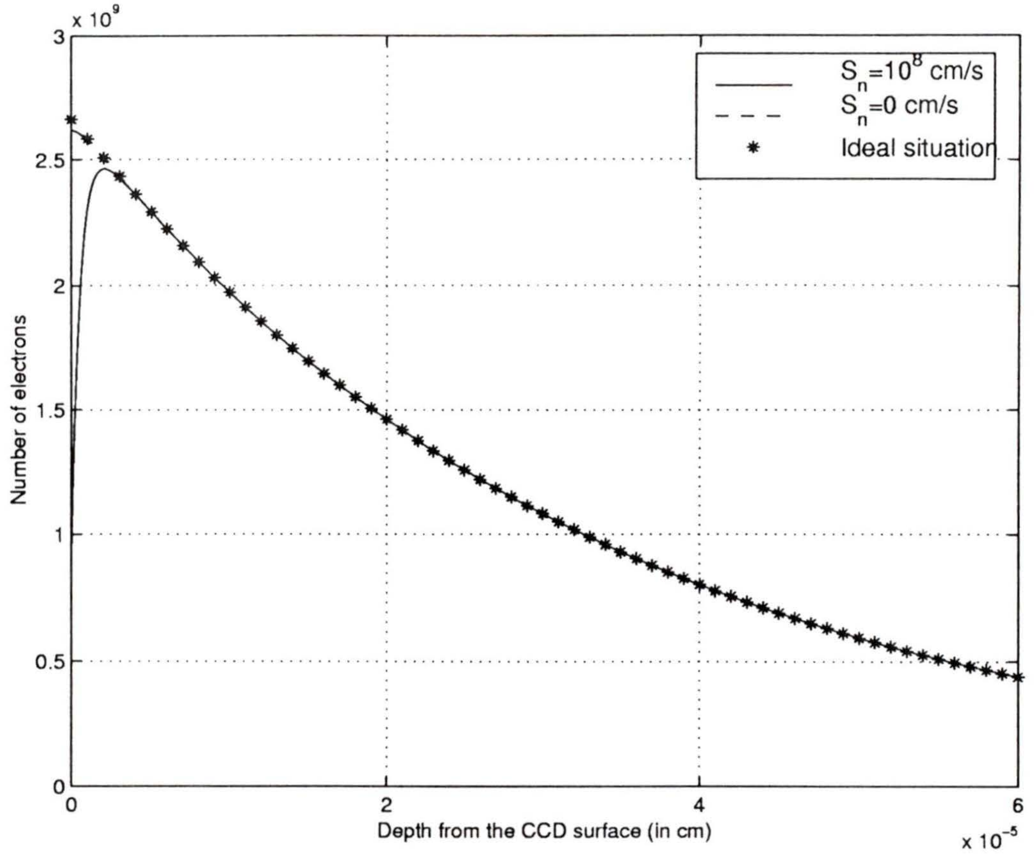

Figure 3.13 The electron concentration along the light path ($\alpha = 3\times10^{4}cm^{-1}$)

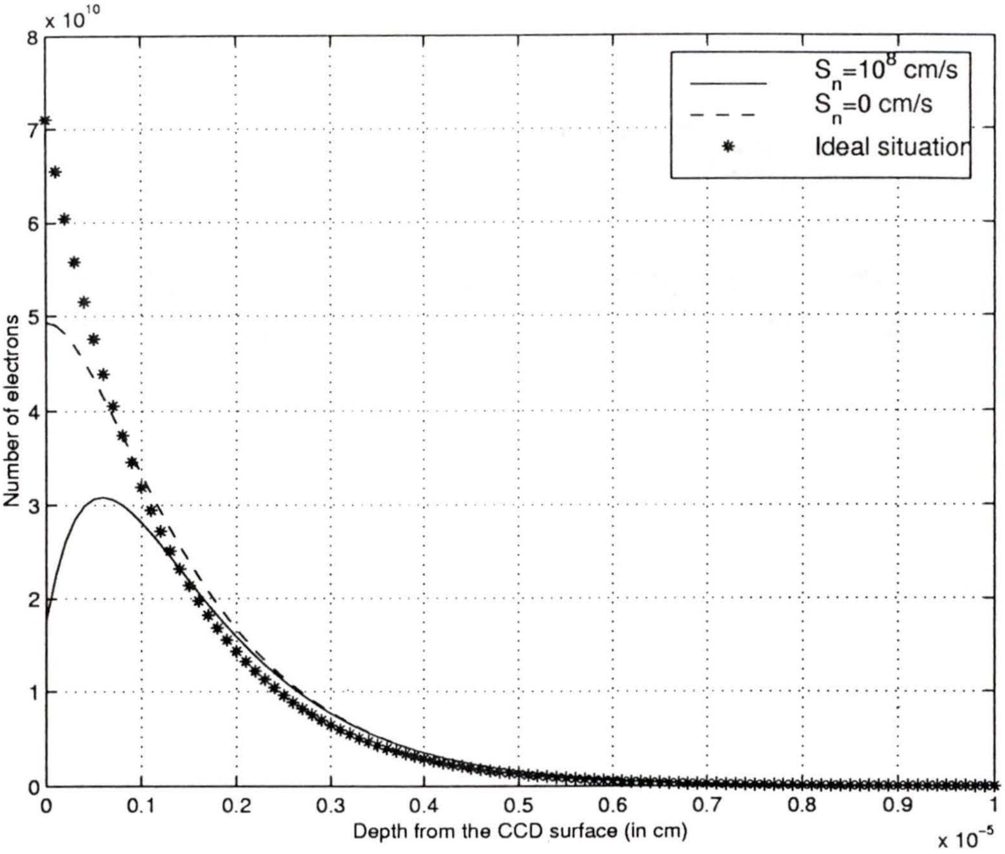

Figure 3.14 The electron concentration along the light path($\alpha = 8\times10^5 cm^{-1}$)

For the different incident light wavelength, Table 3.3 lists the relative difference of the electron calculated for the different surface recombination velocity. From the data we can see that, for the reasonable surface recombination velocity $S_n = 1\times10^8 cm/s$, the shorter the wavelength, the less the electron can be collected. Because for the shorter wavelength, the absorption coefficient α is bigger and more photo-excited carriers are generated near the semiconductor surface which the surface recombination will dominate. For example, if wavelength is 0.2 μm, only 77.2% electron will be collected, that means 22.8% electron generated by the incident light photon lost before they were collected in the potential wells in the CCD. Consider about the extreme condition, that is $S_n = \infty$, for wavelength equals to 0.2 μm, the highest loss is 35.4% based on our model.

Table 3.3. The relative portion of electrons that can be collected

Wavelength μm	0.2	0.3	0.4	0.5	0.6	0.7	0.8	0.85
α (cm^{-1})	$1x10^6$	$9x10^5$	$8x10^5$	$1x10^5$	$3x10^4$	$1x10^4$	$7x10^3$	$4x10^2$
S_n=$1x10^8$ cm/s	77.2%	78.6%	80.3%	96.6%	98.9%	99.6%	99.8%	100%
$S_n=\infty$	64.6%	67%	69.5%	94.8%	98.4%	99.5%	99.6%	99.9%

the relative portion is compared with the ideal situation $s_n=0$
parameters used here are $\tau_n=1x10^{-14}$ s, $D_n=30$ cm^2/s

The second reason for the poor quantum efficiency in short light wavelength is the cermet layer. Since GaAs RGCCDs are front-sided illuminated devices, the incident light will first pass the cermet layer before it reaches the GaAs active layer. Thus, the spectral absorption is affected by the cermet. In order to verify this, we set up another experiment to measure the resistance change of the cermet layer when light shines on it. This is shown in Figure 3.15. The three measured results are shown in Figure 3.16. From the results we can see that the resistance become smaller when the wavelength is shorter than 0.5 μm. The cermet resistance becomes smaller meaning more carriers are generated in the cermet and it indicates that the cermet can absorb more light photons when the wavelength is shorter than 0.5 μm.

From the analysis above we can see that, the surface recombination and cermet absorption reduce the quantum efficiency significantly. Therefore, the blue light response of the GaAs RGCCD decreases.

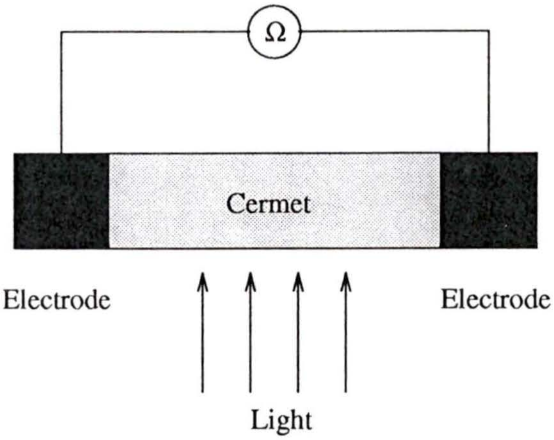

Figure 3.15 Experiment setup to measure cermet resistance

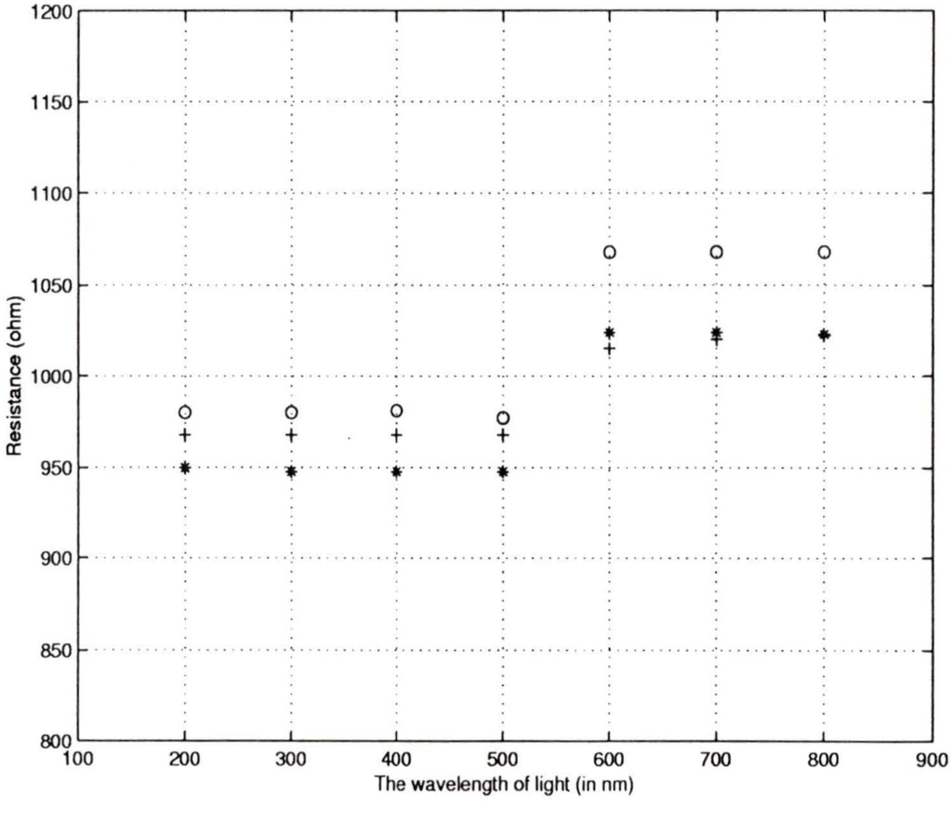

Figure 3.16 Cermet resistance vs. incident light wavelength

Figure 3.17 shows the GaAs RGCCD differential output voltage versus wavelength from 1 μm to 2.2 μm. In Figure 3.17, there is an output peak at about 1.6 μm corresponding to an energy gap which is about 0.78 eV. This was caused by the impurities in the GaAs. In GaAs this energy gap corresponds to a chromium acceptor impurity which is 0.79 eV above valence band or an oxygen donor impurity which is 0.75 eV below the conduction band [31]. This was not a band to band intrinsic response but an extrinsic response of the GaAs RGCCD.

Another experiment was to expose the GaAs RGCCD to different light intensities to examine the relationship between the input light intensity and the output voltage. It is imperative that the light source color temperature remains constant. In this experiment, an incandescent bulb is used. However, reducing the bulb voltage will reduce the light intensity but it also changes the color temperature. Changing the source temperature leads to incompatible results. Thus, in this experiment, the light source intensity was changed by inserting the beam splitters (neural density filters, *c.f.* Figure 3.9). Figure 3.18 shows the results of the output voltages versus different light intensities. From the results we can see that when the light intensity is below a certain level, the output voltage is proportional to the light intensity. When the light intensity exceeds that level, the output voltage reaches saturation. We are of the opinion that this is related to the non-linearity of the floating diffusion output, which will be discussed in Chapter 5. This problem could be resolved using the current output sensing scheme as suggest in [29].

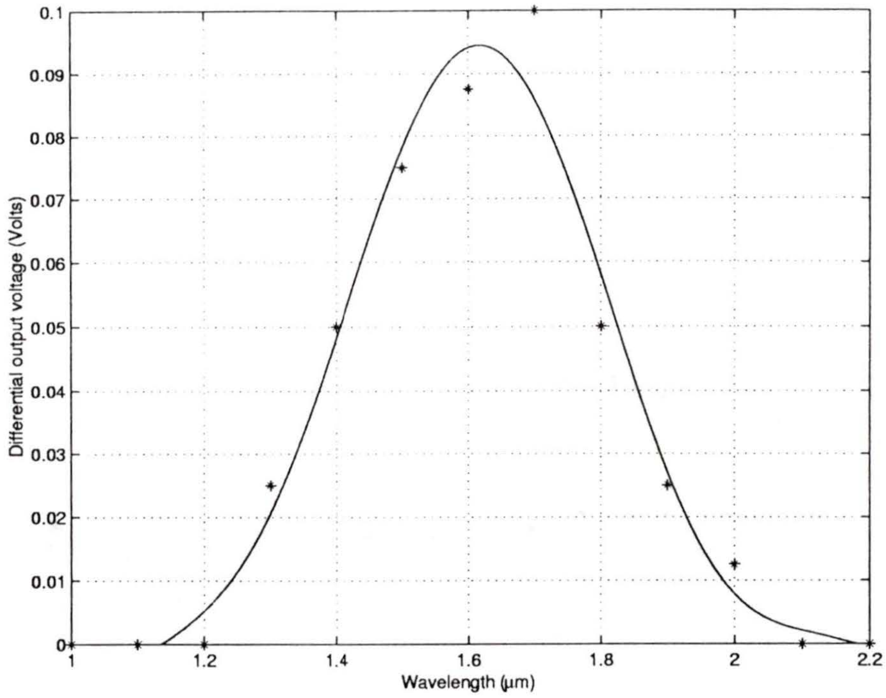

Figure 3.17 The output results versus wavelength

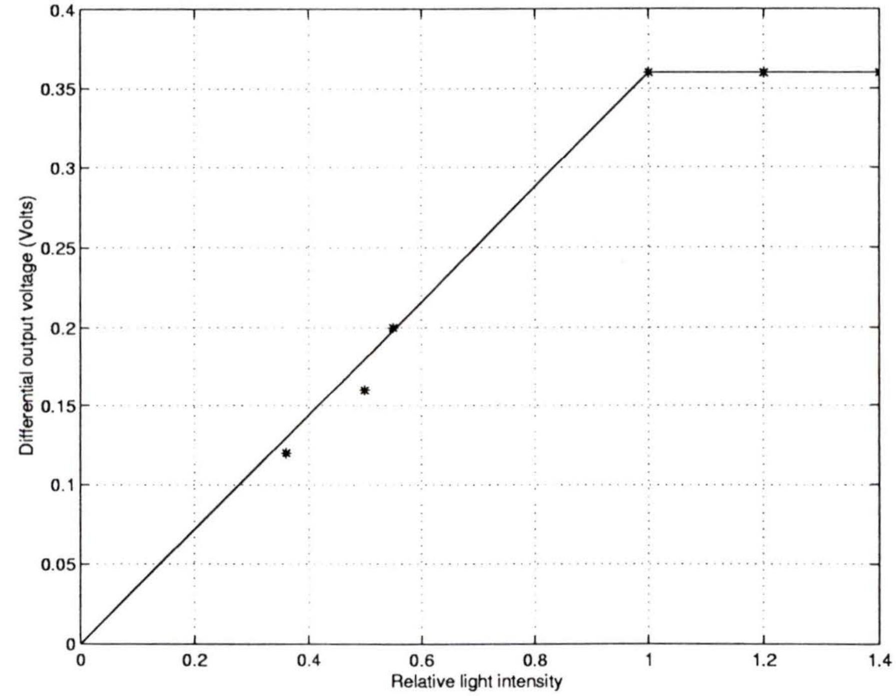

Figure 3.18 The differential output voltage versus light intensity

Chapter 4

The Study of X-ray Interactions in GaAs RGCCD

4.1 Introduction

An X-ray photon is uncharged and creates no direct ionization or excitation in the material through which it passes. The detection of X-ray is therefore critically dependent on the X-ray photon undergoing an interaction that transfers all or part of the photon energy to an electron in the absorbing material. When an X-ray is incident on a GaAs RGCCD, it will interact with the atoms in the GaAs by ejecting an energetic electron from one of the atoms through either the Compton or the photoelectric process. Both of these processes create an electron from one of the bound shells and leave an excited atom. The excited atom will relax to its ground state by either emitting a characteristic X-ray or, through an Auger process, an energetic electron. If a characteristic X-ray is released, it will then interact with other atoms and eject additional electrons similar to the incident X-ray but with a relatively low energy. These energetic electrons can continue to interact with the atoms in the GaAs RGCCD to create electron-hole pairs until their kinetic energies are too low to cause further ionization.

4.2 The Interactions of X-ray with GaAs RGCCD

Although a large number of possible interaction mechanisms are known for X-ray interaction with matter, only three major types will play an important role in radiation measurements, there are: *photoelectric absorption*, *Compton scattering*, and *pair production*.

Pair production occurs when the X-ray photon disappears and is replaced by an electron-positron pair. In order for this to happen, the photon energy must exceed twice the rest-mass energy of an electron, *i.e.* 1.02 *MeV* [32]. During Compton scattering, the incoming X-ray photon is deflected through an angle θ with respect to its original path. The photon transfers a portion of its energy to the electron which is known as a recoil electron with an energy that can vary from zero to a large fraction of the incoming X-ray energy. In the photoelectric absorption process, an X-ray photon undergoes an interaction with an absorber atom in which the X-ray photon completely disappears, and an energetic photoelectron is ejected by the atom from one of its bound shells. The relative importance of the three processes and the photon energies are conveniently illustrated in Figure 4.1 [32].

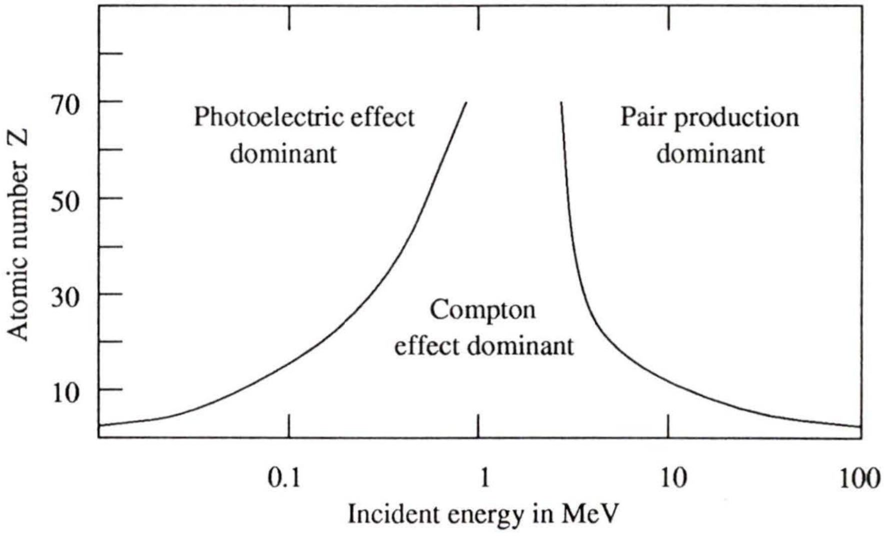

Figure 4.1 The relative importance of the three major types of interaction in matter

The X-ray used to irradiate the GaAs RGCCD in this study ranged in energy from 8 *KeV* to 45 *KeV*, much less than the 1.02 *MeV* needed in the pair production process, thus, the pair production does not happen in this study. Compared to the photoelectric absorption process, the cross-section for Compton scattering has been observed to be negligible [32]. Therefore, it will be assumed that the X-ray photon-solid interactions will be primarily photoelectric absorption process when the GaAs RGCCD is used as an X-ray detector.

4.3 The Photoelectric Absorption

During photoelectric absorption, the incident X-ray photon is absorbed. In its place, a photoelectron is produced from one of the bound shells of the absorber atom with a kinetic energy given by the incident photon energy $h\nu$ minus the binding energy of the electron in its original shell (E_b). This process is shown in Figure 4.2. For the X-ray energies used in this study, the photoelectron is most likely to emerge from the inner-most or *K* shell (~80%) and about 19% from the next higher shell, the *L* shell [33].

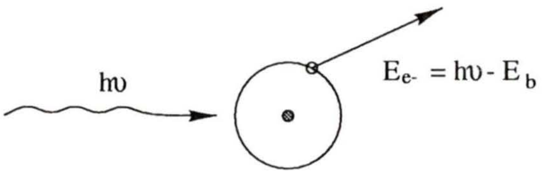

Figure 4.2 The photoelectric absorption in GaAs

The probability, *p(z)* of the incident X-ray photon being absorbed at a distance *dz* at a given depth *z* in a material is given by

$$dp(z) = \alpha \exp(-\alpha z) dz \tag{4.1}$$

where α is the linear absorption coefficient of the X-ray in the material. The cumulative probability, *P(z)*, that an X-ray photon is absorbed by the time it reaches a depth *z* is given by integrating Equation (4.1) to get

$$P(z) = 1 - \exp(-\alpha z) \tag{4.2}$$

When an X-ray photon interacts with an atom during the photoelectric effect, the excited atom may relax to its ground state in two different ways. The first one is for an electron from an outer shell to replace of the ejected electron, with the emission of an X-ray of energy $E - E_o$, where E_O is the energy of the outer shell involved in the process. This X-ray photon is called a characteristic X-ray photon. The characteristic X-ray photon may interact with other atoms and eject an electron through photoelectric effect. The second one is an Auger process. The excitation energy of the atom is transferred directly to one of the outer electrons, causing it to be ejected from the atom. This electron is called an Auger electron and appears with an energy given by the difference between the original atomic excitation energy and the binding energy of the shell from which the electron was ejected. Figure 4.3 illustrate the process. The ratio of characteristic X-ray photons to all possible atom deexcitations is defined as the fluorescent yield, and it is independent of the incident X-ray energy. For Ga and As nucleus, the fluorescent yields for the K-shell are: Ga~50.7% and As~56.2%, respectively [36].

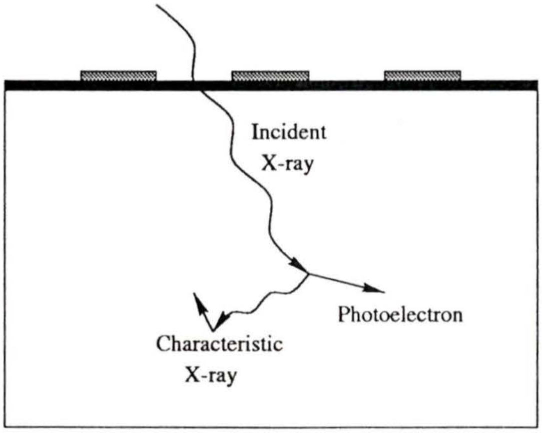

Figure 4.3 The creation of characteristic X-ray and photo-electron in CCD

4.4 Interactions of Electrons in GaAs

The photo-electrons and Auger electrons created by the incident X-ray have energies from 0 *KeV* to 35 *KeV*. These electrons will interact with other electrons and the nucleus of the GaAs through different processes and lose their energy. A large electron cloud will therefore be created along the electron trace. All of these interactions can be modeled using an analytic model proposed by Bethe based on the phenomenological continuous energy loss approximation. The energy loss dE per unit distance dx traveled by an excited electron in the solid is given by [37]

$$dE/dx = -7.85 \times 10^4 (Z\rho/AE)\log(1.1658E/J) \tag{4.3}$$

where E is the energy of the electron, Z is the atomic number, ρ is the density, A is the atomic mass and J is the average energy loss per interaction considering all possible energy loss processes. For $Z > 6$, J is given as [38]

$$J = (9.76Z + 58.5Z^{-0.19}) \times 10^{-3} KeV \tag{4.4}$$

The continuous energy loss approximation can be used to estimate the electron energy loss rate *dE/dx* in GaAs for a given electron energy, therefore it can be used to determine the mean distance an electron with the given energy would travel if the electron did not change its direction of travel during the interactions. Figure 4.4 shows the relationship between the mean distance and the electron energy. Actually, the distance an electron travels in the GaAs RGCCD X-ray detector is much less than this since there can be many scattering processes in the path.

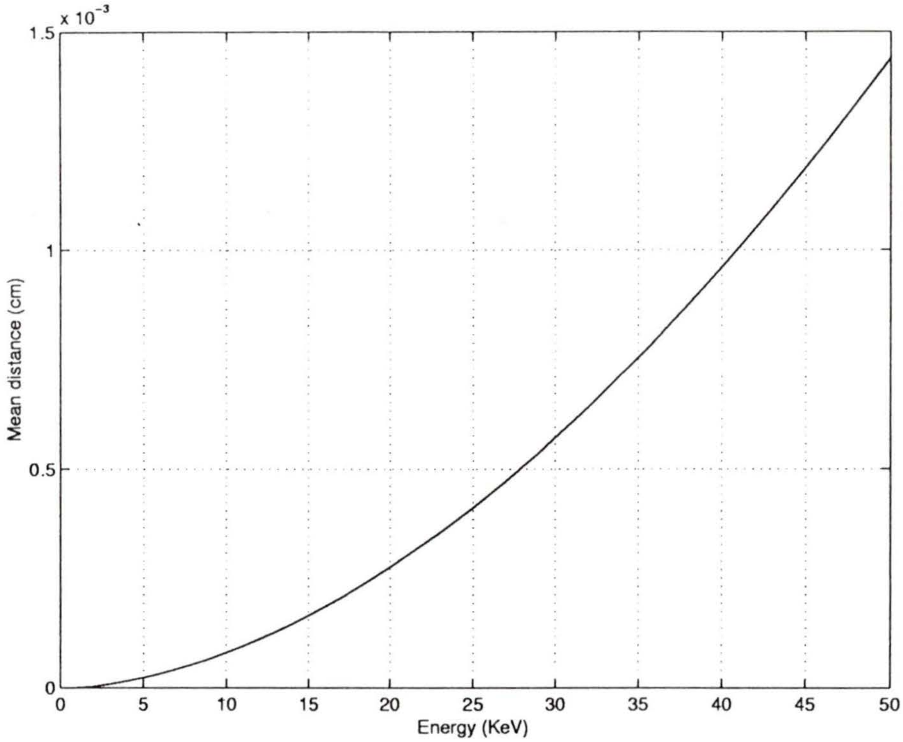

Figure 4.4 The mean distance v.s the energy

As mentioned earlier, an electron loses its energy through multiple scattering processes and these will create a large number of secondary electron-hole pairs (e.h.p.s). These e.h.p.s will also scatter and create more e.h.p.s. The cascade process continues until the energy of all the ionized e.h.p.s reduces to a few eV. The total electron-hole pairs created by this process is $N = E/w$, where w for GaAs is 4.2 eV/e.h.p.s [34]. This means that it takes 4.2 eV to create a relatively long-lived electron-hole pair in GaAs. Since the creation of electron-hole pairs is a statistical process, the number of e.h.p.s created by an electron of energy E will not be a constant. The variance of N is $(f \cdot N)^{1/2}$ and is used to account for the photon shot noise. f is called the Fano factor, which for GaAs at room temperature $f = 0.14$ [35].

If none of the energy of an incident photon of energy E escaped from the detector, then the number of electrons N collected by the GaAs RGCCD X-ray detector for a given

X-ray photon would be a Gaussian distribution with a mean value of E/w. The variance of this distribution would be $\sigma^2 = fN_{ehp}$. The X-rays used in this study had energies from 8 *KeV* to 45 *KeV*, corresponding to the creation of 1904~10714 electron-hole pairs. Using the Fano factor of $f = 0.14$, the Gaussian radius is 16 and 39 e.h.p.s, respectively.

4.5 Charge Collection from the Depletion Layer

4.5.1 The Potential Underneath an Electrode in the GaAs RGCCD

The GaAs RGCCD X-ray detector used in this study was also fabricated at TRIUMF. All the parameters of the GaAs RGCCD are the same as what we used in Chapter 3, except the thickness of the buffer layer (it is called active region in the X-ray detector). The thickness of the active region is 30 μm in this study. Figure 4.5 shows the structure of the GaAs RGCCD X-ray detector.

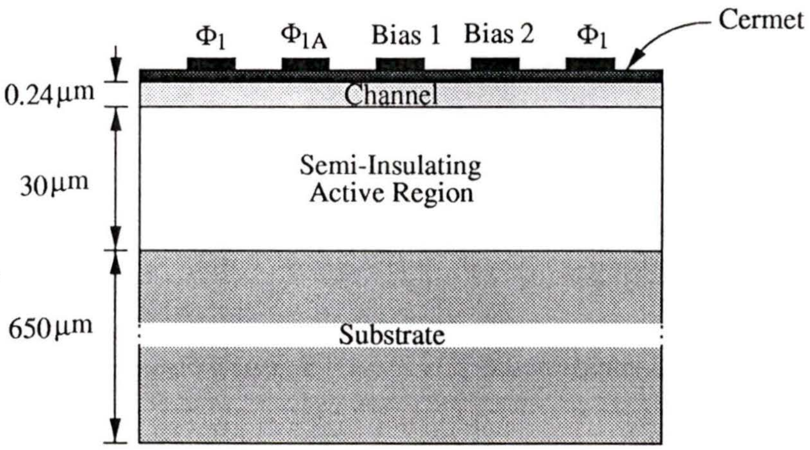

Figure 4.5 Structure of the GaAs RGCCD X-ray detector

There are two different regions under an electrode in the GaAs RGCCD active region: one is the depletion region and another is the field-free region (FFR). To find the depletion depth in the active region in the GaAs RGCCD, Poisson's equations relating the second derivative of the potential to the charge distributions in the channel and the active region should be solved. They are

$$\frac{d^2\psi}{dx^2} = -\frac{qN_d}{\varepsilon_{GaAs}}, 0 < x \le t \tag{4.5}$$

$$\frac{d^2\psi}{dx^2} = \frac{qN_a}{\varepsilon_{GaAs}}, t < x \le t + x_p \tag{4.6}$$

where t is the thickness of the channel, x_p is the thickness of the depletion layer in the SI active region, ψ is the electrostatic potential and ε_{GaAs} is the permittivity of the GaAs. N_d and N_a are the donor density in the channel and the acceptor density in S.I. GaAs active layer, respectively.

The boundary conditions are

$$\psi(0^+) = V_g - V_{bias} - \phi_b \tag{4.7}$$

$$\psi(t + x_p) = 0 \tag{4.8}$$

$$\psi(0^+) = \psi(0^-) \tag{4.9}$$

$$\left.\frac{d\psi}{dx}\right|_{t^+} = \left.\frac{d\psi}{dx}\right|_{t^-} \tag{4.10}$$

where V_g is the applied electrode voltage, V_{bias} is the reverse bias voltage applied on the bottom of the GaAs RGCCD substrate and ϕ_b is the barrier height of the Schottky diode. Equation (4.8) specifies the value of the potential at the edge of the depletion region. At the interface, Equation (4.9) and (4.10) represent the continuity of the potential and its derivative, respectively.

We solve Equation (4.5) and (4.6) using the boundary conditions and plug the parameters of the GaAs RGCCD into these equations. When the V_{bias} is 0 V, the depth of the depletion region is $d = 4\mu m$ and the depth of the FFR is $\delta = 26\mu m$. When the V_{bias} is -7V (which is the largest value to use the GaAs RGCCD safely), the depth of the depletion region is $d = 11.32\mu m$ and the depth of the FFR is $\delta = 18.68\mu m$.

4.5.2 Charge Collection

As mentioned above, photo electric absorption of an X-ray ejects an e.h.p.s of appreciable energy (*c.f.* Figure 4.2). The energetic electrons that penetrate the material are scattered inelastically, primarily by collisions with bound electrons in the material. In this process, the path of the electrons will be almost straight lines. The electrons are also scattered through large angles, primarily through elastic collisions with the shielded nuclei. Therefore the paths of the energetic electrons will be in a zigzag. The primary electrons will then lose all their energy through multiple scatterings. The number of large angle collisions per unit path length will determine the actual path of the electrons in the material. The probability of an elastic collision with the shielded nuclei is given by [39]

$$P_{ec}(\phi, E) = \frac{N_0 e^4}{16}\left(\frac{Z\rho}{A}\right)\left(\frac{Z}{E^2}\right)\frac{\Delta x}{\sin^4(\phi/2)} \qquad (4.11)$$

where the ϕ is the scatter angle.

The fractional energy loss $\Delta E/E$ is [37]:

$$\frac{\Delta E}{E} = (-2\pi e^4 N_0 Z\rho/AE^2)\log(1.1658E/J)\Delta x \qquad (4.12)$$

The path of the electron can be estimated from the ratio of the angular scattering probability $P_{ec}(\phi, E)$ to the fractional energy loss $\Delta E/E$:

$$\frac{P_{ec}(\phi, E)}{\Delta E/E} = \frac{1}{32\pi}Z\frac{1}{\log(1.1658E/J)\sin^4(\phi/2)} \qquad (4.13)$$

For the GaAs RGCCD X-ray detector, Equation (4.13) can be rewritten as

$$\frac{P_{ec}(\phi, E)}{\Delta E/E} = \frac{0.318}{(\log E + 1.225)\sin^4(\phi/2)} \qquad (4.14)$$

From Equation (4.14), it can be seen that the large angle scattering per unit fractional energy loss is rather insensitive to electron energy *E*, since it varying only logarithmically. It also can be seen that the chance for a large angle scattering is very small. Therefore, for simplicity, the shape of the charge cloud created by a given energy electron is assumed to be cyclindrical.

Using the Bethe continuous energy loss approximation Equation (4.3), for an electron with energy 30 *KeV*, the energy loss of the electron per unit length, $dE/dx = 28620$ *KeV/cm*. The average energy needed to create an electron-hole pair in GaAs, $w = 4.2$ *eV*. The number of e.h.p.s N_{ehp} created in a unit length (*i.e.* 1 *μm*) in the GaAs RGCCD is 681. We assume that such a generation rate along the electron track is constant and that the cylindrical track of the e.h.p.s has an initial radius less than 0.1 *μm* [40]. Therefore at $t = 0$, the electron density in the track is

$$N_{axis} = \frac{N_{ehp}}{\pi\sigma_0^2} = 2.168 \times 10^{16}/cm^3 \qquad (4.15)$$

We assume that the e.h.p.s can effectively screen the interior of the charge distribution from the applied field when the electron-hole pair density exceeds the background doping of the GaAs, which is 10^{14} cm^{-3} in this case. The electrons and holes outside of this radius will drift toward the top and bottom of the GaAs RGCCD X-ray detector, respectively. Electrons and holes inside of this radius of penetration will however undergo ambipolar diffusion. The speed of the diffusion for the interior charge is determined by the ambipolar diffusion constant, D_{ap}. The correct transition from ambipolar diffusion to normal diffusion depends on relative values [41].

$$D_{ap} = (n_i + 2N_{axis})D_n D_p/((n_i + N_{axis})D_n + N_{axis}D_p) \qquad (4.16)$$

where n_i is the doping density, D_n is the electron diffusion coefficient and D_p is the hole diffusion coefficient.

For $N_{axis} \gg n_i$ (in this case, $2.168\times10^{16}/cm^3 \gg 1\times10^{14}/cm^3$), Equation (4.16) can be reduced to

$$D_{ap} = 2D_n D_p/(D_n + D_p) \qquad (4.17)$$

For GaAs, D_n and D_p are 221 cm^2/s and 10.4 cm^2/s, respectively [1]. This gives an ambipolar diffusion constant of $D_{ap} = 19.87 cm^2/s$.

The transport equation of the e.h.p.s is governed by [30]

$$\frac{\partial \rho_{ehp}}{\partial t} = -D_{ap}\nabla^2\rho_{ehp} + \frac{\rho_{ehp}}{\tau} \qquad (4.18)$$

where the ρ_{ehp} is the density of electron-hole pairs.

A simplified one dimensional (depth) model is used and we assume the electron lifetime, τ, is a constant (this assumption is probably incorrect, the relaxation from high concentrations to levels where τ is a constant occurs so rapidly in GaAs that the changing lifetime will not produce a substantial error), the solution of Equation (4.18) is

$$\rho_{ehp}(x, t) = \frac{N_{ehp}}{4\pi D_{ap} t}\exp\left(-\frac{x^2}{4D_{ap}t} - \frac{t}{\tau}\right) \qquad (4.19)$$

Solving this equation, it was found that the distribution would take ~400 *ps* to diffuse to the background density, and the width of the distribution at this time is ~0.5 μm.

The worst case occurs at the bottom of the depletion region, where the X-ray photon is absorbed at $11\mu m$ from the CCD surface electrodes. The bias voltage is -7 V, which will result in an average drift field of about 6300 *V/cm*. The electron mobility μ_n is 8500 $cm^2/V\text{-}s$ and the drift velocity, v, will be $\sim 5.4 \times 10^7$ *cm/s*. It will therefore take about 20 *ps* for the electrons to drift from the bottom of the depletion region to the CCD potential well. Thus, total time need for collecting all the electron in the depletion region is about 420 *ps*. From the simulation results presented in Chapter 2, it needs about a minimum of 250 *ps* to transfer the signal charge packet from one GaAs RGCCD electrode to another electrode with a reasonable CTE, therefore this implies that the fastest operation frequency of the CCD X-ray detector should be less than 1.5 *GHz*.

4.6 Quantum Efficiency

If we assume that the S.I. GaAs active region is homogeneous (with no variations in the diffusion length for electrons and holes) and is field free, then for a simplified one dimensional model, the fraction f_1 of the incident X-ray beam that is absorbed in the depletion region is given by

$$f_1 = 1 - \exp(-\alpha d) \tag{4.20}$$

where d is the depletion depth and α is the linear absorption coefficient.

The fraction f_2 of the incident X-ray absorbed in the FFR below the depletion region is given by

$$f_2 = (1 - \exp(-\alpha\delta))(1 - f_1) \tag{4.21}$$

where δ is the depth of the field free region.

Based on the recombination losses in the field free region, the number of electron-hole pairs created in an incremental thickness at depth x is multiplied by $\exp(-x/L)$ to account for recombination, where L is the effective diffusion length. The number of electrons collected is obtained by integrating the incremental thickness contributions over the depth of the GaAs RGCCD in the field free region. Thus, the ratio of electrons collected per electron hole pairs produced in this region is given by

$$R = \frac{\alpha}{\alpha + 1/L}\left(\frac{1 - \exp(-(\alpha + 1/L)\delta)}{1 - \exp(-\alpha\delta)}\right) \tag{4.22}$$

From the analysis above, the quantum efficiency is the fraction of the total X-ray energy which is used to convert to electron-hole pairs. From Equation (4.20) to (4.22), the quantum efficiency η is

$$\eta = f_1 + f_2 R \tag{4.23}$$

the first term on the right-hand side of Equation (4.23) is the fractional probability of absorption in the depletion layer, the second term is the fractional probability of absorption in the FFR which resulted in collectible electron-hole pairs under the GaAs RGCCD electrodes.

The results of the calculation described above, along with different energy X-rays and corresponding linear absorption coefficients, are presented in Table 4.1

Table 4.1. Quantum efficiency of different X-ray energies

Element	Cu	Rb	Mo	Ag	Ba	Tb
K_α X-ray energy (KeV)	8.047	13.394	17.489	22.162	32.190	44.170
Linear absorption coefficient, $\alpha(cm^{-1})$	352.95	649.11	320.32	166.93	58.54	23.02
Quantum efficiency η	56.10%	76.98%	52.74%	32.73%	13.11%	5.39%

From the results it can be seen that when the linear absorption coefficient decreased, the quantum efficiency drops. For Tb K_α X-ray, the quantum efficiency is as low as 5.39%.

4.7 Charge Packet Splitting

The electrons created in the depletion region will diffuse radially as they drift through the depletion region. The radius of the electron cloud depends on the distance the electrons traveled. If the X-ray photon interacts in the depletion depth, $x < d$, see Figure 4.6, the 1σ radius is given by Hopkinson as [42]

$$r_d = (2D_{ap}\varepsilon_{GaAs}/\mu q N_a)^{1/2}(\ln(d/(d-x)))^{1/2} \tag{4.24}$$

where μ is the electron mobility. In order to avoid the singularity at x equals d, an offset of 0.05 μm is used at this boundary [42]. In the worst case, the events occurs at the bottom of the depletion region, therefore the maximum radius $r_{dmax} = 0.43\mu m$.

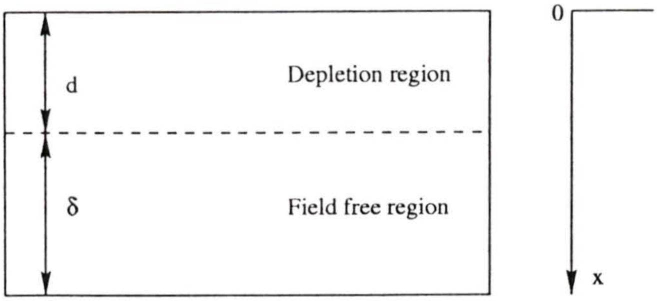

Figure 4.6 The diagram of depletion region and field free region

In the field free region, $d < x < d + \delta$, the electron-hole pairs will diffuse until they reach the depletion boundary. The 1σ radius at the depletion boundary is based on a model by Janesick *et al.* and is given by [43]

$$r_f = \delta/2(1 - ((x-d)/\delta)^2)^{1/2} \tag{4.25}$$

The singularity at the boundary of depletion region and FFR where $x - d = \delta$ is again avoided by the offset. In the worst case, the events occur at the bottom of the FFR, which $\delta = 18.68\mu\mathrm{m}$, therefore the maximum radius $r_{fmax} = 29.92\mu\mathrm{m}$.

The overall radius of the electron distribution under the electrode is

$$r = (r_d^2 + r_f^2)^{1/2} \tag{4.26}$$

Based on these calculations, the maximum overall radius $r_{max} = 29.92\mu\mathrm{m}$. The length of each pixel of the GaAs RGCCD X-ray detector is 24μm, and the GaAs RGCCD X-ray detector uses the statistical method to obtain the signal, therefore under the worst case, the charge cloud will spread to maximum of 5 pixels which is shown in Figure 4.7. This analysis results agree with the experiment results of S. Patten which are shown in Figure 4.8 [33]. $\mathrm{N_{signal}}$ here is the number of the GaAs RGCCD pixels used in the experiment to collect the charge packet. If the charge packet in a single event were contained in one pixel of the GaAs RGCCD, changing $\mathrm{N_{signal}}$ would have little effect on the shape of the spectra. In fact, if the number of CCD pixels that contain charge packet from an event is $N_{charged}$, then for $N_{signal} > N_{charged}$, there should be no change on the shape of the spectra. From the results we can see, the change in the shape of the spectra from $N_{signal} = 3$ to $N_{signal} = 5$ is quite large, and the change for N_{signal} larger than 5 is much smaller. This suggests that the charge packet in a signal from a Tb X-ray is contained in at most five pixels, and that some events have more than three pixels with the charge packet in them.

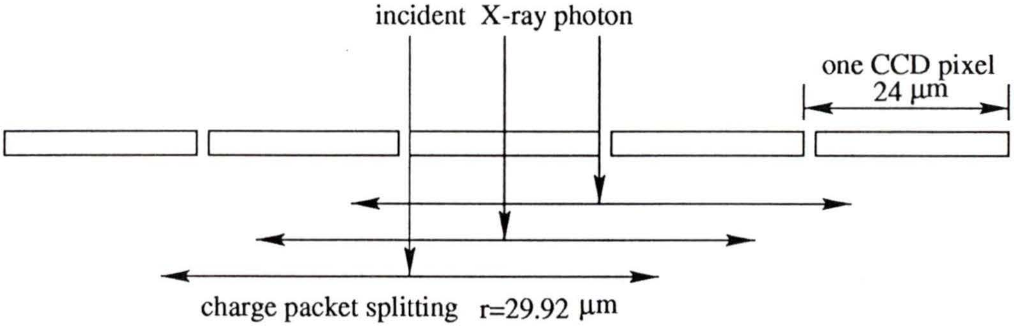

Figure 4.7 Charge packet splitting in CCD

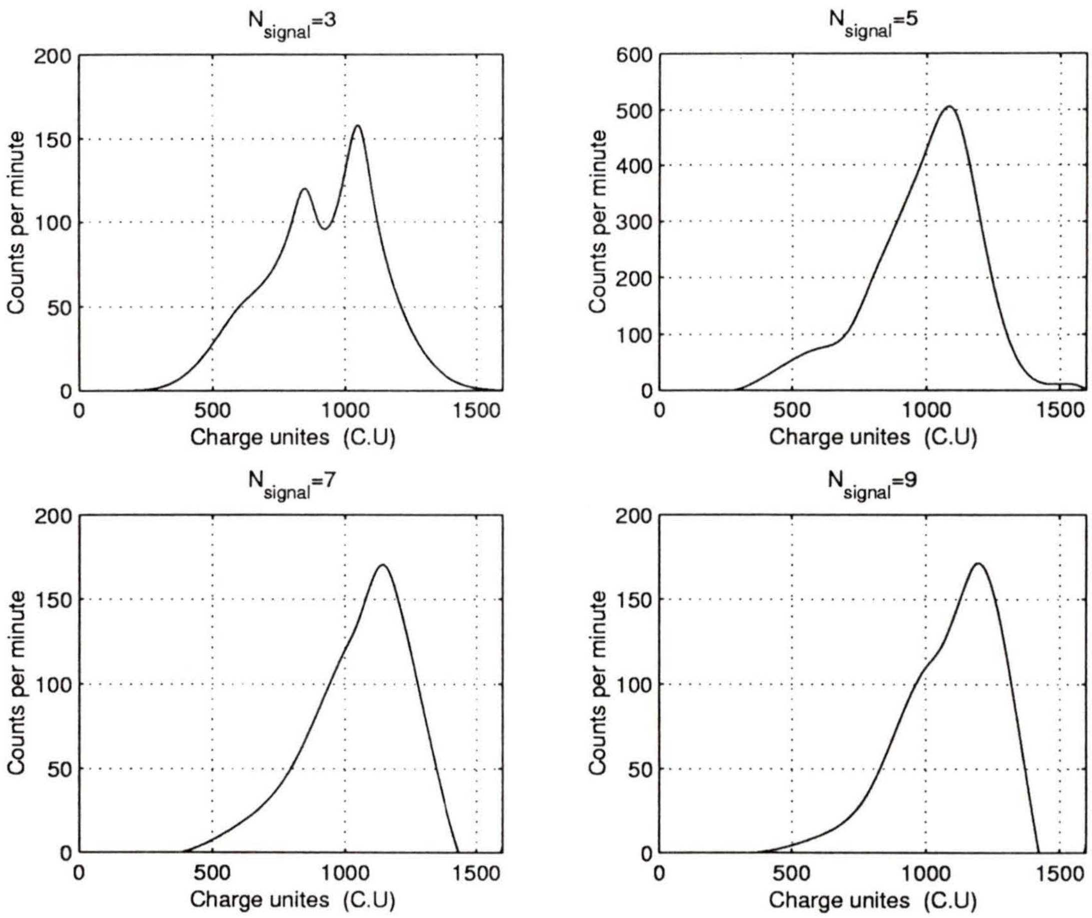

Figure 4.8 The spectra of Tb X-rays with N_{signal}=3,5,7 and 9 [33]

For a higher quantum efficiency with the GaAs RGCCD X-ray detector, the signal charge packet should be confined in one pixel, and therefore the depletion region should be deeper (*c.f.* Equation (4.24) to (4.26): the bigger the depth of depletion region, the smaller the overall radius of the electron distribution). From the analysis presented in Section 4.5 (Equation (4.5) to (4.10)), if the CCD is fabricated on a high resistivity layer (the N_a is smaller), the depletion region will essentially penetrate all of the active layer.

4.8 Noise Analysis

CCD is inherently a low noise device in the sense that information is represented by the charge packets which are kept isolated inside the semiconductor during the storage and transfer process. The noise in the GaAs RGCCD X-ray detector can be separated in four components: (1) shot noise (photon noise), (2) dark current noise, (3) bulk state trapping noise and (4) output noise. Detailed discussions on the different noise are presented below.

4.8.1 Shot Noise (photon noise)

When a packet of charge is stored in a CCD, the number of electrons in the charge packet has an amount of uncertainty. This uncertainty becomes noise in the charge packet, which is called shot noise. For a CCD X-ray detector, the charge packet is generated by an incident X-ray. This process is a random one and the number of electron hole pairs generated is described by the Poisson probability distribution, as mentioned in Section 4.4. For the GaAs RGCCD X-ray detector, the noise is

$$\sigma^2 = fN_{ehp} \tag{4.27}$$

This noise itself does not impose a serious limitation to the dynamic range of the X-ray detector since the noise power is proportional to the signal magnitude.

4.8.2 Dark Current Noise

The number of thermally generated dark current electrons is [19]

$$n_{dark} = \left(\frac{J_d A_s M}{q f_c}\right)^{1/2} \tag{4.28}$$

where A_s is area of the single pixel, M is the number of the pixels CCD has, f_c is clock frequency, and J_d is the dark current density which is depended upon the temperature,

$$J_d = ke^{-\frac{E_g}{2kT}} \tag{4.29}$$

where E_g is the band gap and for GaAs, E_g is given by [30]

$$E_g = 1.519 - \frac{4.405\times10^{-4}T^2}{T+204} \tag{4.30}$$

For the GaAs RGCCD X-ray detector used in this study, $A_s = 1\times10^{-5}cm^2$, $f_c = 10MHz$, $M = 128$, and $J_d = 10nA/cm^2$, the dark noise can be calculated by Equation (4.28) is about 3 electrons.

In principle, dark current density can be made negligible with sufficient cooling. Dark current density decreases approximately twofold for every 7 to 8 °C drop in CCD detector temperature. Therefore the dark current noise drops quickly with a decrease in the temperature.

4.8.3 Bulk State Trapping Noise

Bulk traps are the dominant source in fast interface state noise for the GaAs RGCCD X-ray detector since the signal charge packets are transferred within the bulk of the CCD channel. The bulk state can either capture an electron or emit an electron. The noise related to the bulk state emitting an electron is given by [44]

$$n_{empty} = (MV_{sig}N_t\exp(-T_t/\tau_e)(1-\exp(-T_t/\tau_e)))^{1/2} \tag{4.31}$$

where V_{sig} is the volume that the charge packet occupies, T_t is the transfer time, N_t is the number of bulk states per unit volume, typically equal to $10^{11}/cm^3$ for the GaAs RGCCD X-ray detector, and τ_e is emission time for an electron and can be varied over many orders of magnitude by changing the temperature. When $\exp\left(-\frac{T_t}{\tau_e}\right) = 0.5$, the Equation (4.31) has the maximum value. Therefore when the signal charge packet is 1×10^4 electrons, the maximum noise is $(n_{empty})_{max} = 1$ electrons.

The noise related to the bulk state capturing an electron is given by [44]

$$n_{fill} = (MV_{sig}N_t\exp(-(T_t+N_zT_c)/\tau_e)(1-\exp(-(T_t+N_zT_c)/\tau_e)))^{1/2} \tag{4.32}$$

Similarly, the maximum noise of the capture is $(n_{fill})_{max} = 1$ electrons.

Therefore, the overall bulk state trapping noise is $n_{trap} = (n_{empty}^2 + n_{fill}^2)^{1/2} \approx 1$ electrons.

4.8.4 Output Noise

Actually, the output noise is the main noise source in the GaAs RGCCD X-ray detector. The detail of the output noise will be discussed in Chapter 5.

Chapter 5

CCD Output Structure Comparisons

5.1 Charge Sensing Techniques

Once a charge packet is injected into a CCD, its propagation in the channel will be under the control of the clock voltages applied to the gate electrodes. The charge packet will be detected at the CCD output. If the charge is directly sensed at the output of CCD, then it will be destructive because the signal charge will be removed from the CCD channel completely. In some analog applications, it is often desirable to repeatedly measure the output charge using a non-destructive charge-sensing method. Another option in charge sensing depends on whether a voltage output or a current output is required. Both these considerations will affect the choice of the sensing technique and give rise, consequently, to a variety of sensing circuits. In this chapter we will discuss and compare three different CCD output circuits for signal charge sensing.

5.2 Floating Diffusion Sensing

Probably the most widely adopted scheme for detecting the output charge of a CCD is the use of a floating diffusion output structure. This is a destructive voltage-sensing scheme. The floating diffusion node is directly connected to the gate of the output transistor, and the potential of the floating diffusion node controls the output voltage. The floating diffusion node is also connected to a reference voltage V_r via a transistor, which is periodically turned on to reset the floating diffusion node to the reference voltage V_r. Alternately stated, the signal charge packet is removed from the floating diffusion node once each cycle by the reset transistor. The structure of the floating diffusion sensing technique for GaAs CCD is shown in Figure 5.1 [45].

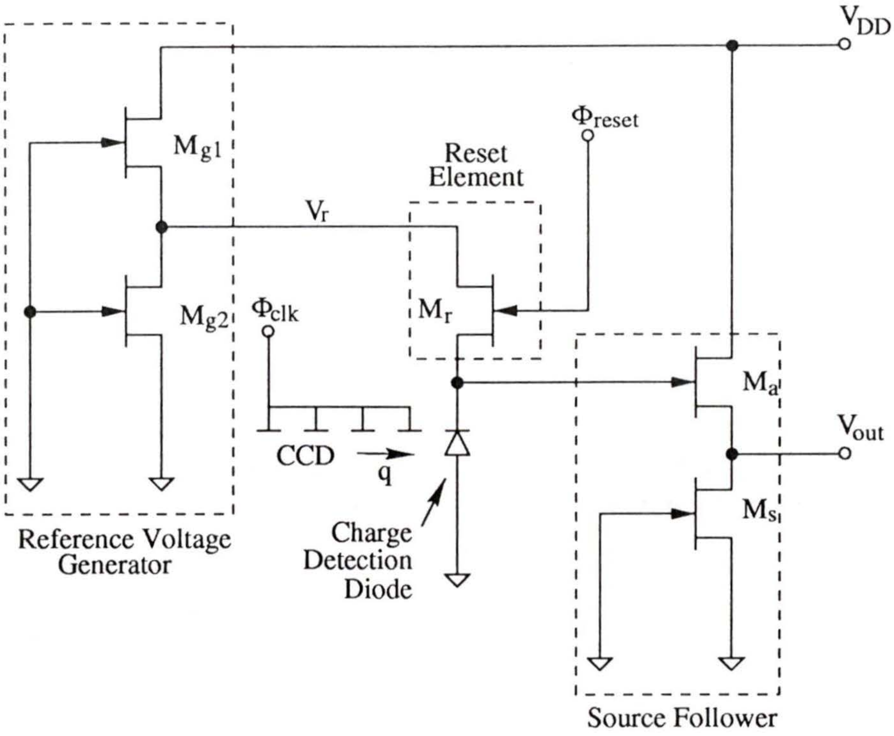

Figure 5.1 Circuit diagram of a typical floating diffusion reset technique for GaAs CCD signal charge detection

5.2.1 Noise Analysis

5.2.1.1 Floating Diffusion Reset Noise

From thermodynamic principles it is well known that the voltage on the floating diffusion capacitor is not the same after every reset, even if there is no charge packet collected in the detection node. The noise introduced by the reset will be the thermal noise of the MESFET (or MOSFET) channel resistance which is in parallel with the floating diffusion capacitance. The noise equivalent circuit diagram of floating diffusion is shown in Figure 5.2 [46]. The resistance *R* is equivalent to a noise current source which is in parallel with *R*. The noise current source is

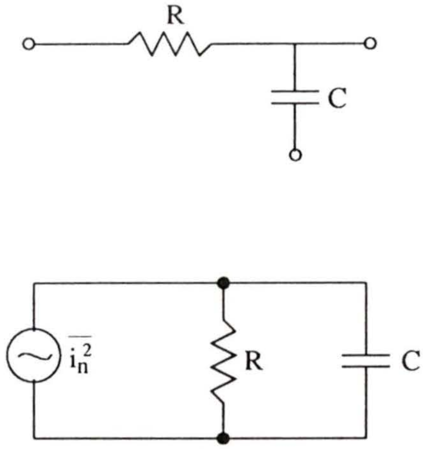

Figure 5.2 Equivalent circuit of floating diffusion reset noise

$$\overline{i_n^2} = 4kT\Delta B/R \tag{5.1}$$

where k is Boltzmann constant and ΔB is the bandwidth which is determined by the clock frequency.

The voltage fluctuations across the RC network will depend upon its frequency characteristics. The mean-squared noise voltage per unit bandwidth is given by:

$$\overline{v_n^2} = \frac{\overline{i_n^2}}{|G|^2} \tag{5.2}$$

where

$$G = \frac{1}{R} + j\omega C \tag{5.3}$$

$$|G|^2 = \frac{1}{R^2}(1 + \omega^2 R^2 C^2) \tag{5.4}$$

The total mean-squared noise voltage will be the integral over frequency of $\overline{v_n^2}$.

$$\overline{V_n^2} = \int_0^{\infty} \overline{v_n^2} df = \frac{4kT}{2\pi C} \int_0^{\infty} \frac{\frac{1}{RC}}{\frac{1}{R^2C^2} + \omega^2} d\omega = \frac{kT}{C} \tag{5.5}$$

By equating signal to the square root of the noise variance, the noise equivalent signal in number of electrons will be

$$\overline{N_e} = \frac{1}{q} C \overline{V_n} = \frac{1}{q} \sqrt{kTC} = 400 \sqrt{C_{pF}} \tag{5.6}$$

where C_{pF} here means that the capacitance is in unit of pF.

Note that although the resistance of the transistor is the source of the fluctuations, its value does not affect the total charge fluctuations. This is because, while larger values of R increase the mean-squared noise voltage per unit bandwidth, they decrease the effective bandwidth by the same factor. A larger capacitance reduces the bandwidth by $1/\sqrt{C}$, thereby reducing the noise voltage, but it also increases the charge fluctuations for a given rms noise voltage by C. This results in the $\sqrt{C}$ dependence. Since this noise is related to the product of kTC, some times it is called kTC noise [19].

The floating diffusion node capacitance consists of all the capacitances connected to this node (includes the parasitic capacitances) and its analysis is very difficult. But we can establish a model to simulate it. Assuming the total capacitance is only divided into two parts:

$$C_{fd} = C_d + C_g \tag{5.7}$$

where the C_d is the depletion capacitance of the diffusion node, C_g is the input gate capacitance of the source follower. C_g will not change when the potential of the floating diffusion node changes, but C_d will change. C_d is a function of the voltage applied on the floating diffusion node which is given by [1]

$$C_d = S\sqrt{\frac{q\varepsilon N_{Beff}}{2}}(V_{bi} - V - 2kT/q)^{-1/2} \tag{5.8}$$

where V is the voltage across on the depletion capacitance, S is the area of the diffusion node, N_{eff} is the effective dopant density which is given by [30]

$$N_{eff} = \{[N_D(1 + N_D/N_A)]^{1/2} + [N_A(1 + N_A/N_D)]^{1/2}\}^2 \tag{5.9}$$

and V_{bi} is the built-in voltage which is given by

$$V_{bi} = \frac{kT}{q}\ln\frac{N_D N_A}{n_i^2} \tag{5.10}$$

where N_D is the donor density in /cm^3, N_A is the acceptor density in /cm^3 and n_i is the intrinsic carrier density of the semiconductor in /cm^3.

For the GaAs RGCCDs we have tested, they used the floating diffusion charge sensing technique. The size of floating diffusion node is $3\mu m \times 25\mu m$ and the size of the source follower is $1\mu m \times 50\mu m$. Since the input gate capacitance of the source follower (M_a in Figure 5.1) is difficult to calculate, we simulated the circuit which is shown in Figure 5.3 to estimate the capacitance. DC voltage source *Vdc* and pulse voltage source *Vpulse* are used to provide the proper bias for the source follower. Using a small DC current $I = 1$ nA to charge the node A for t seconds and measure the voltage change V at the same node, we can get the input gate capacitance which is $C_g = \frac{I \cdot t}{V}$. The simulation result is shown in Figure 5.4. From the result we observed that the input gate capacitance of the source follower is 31 fF.

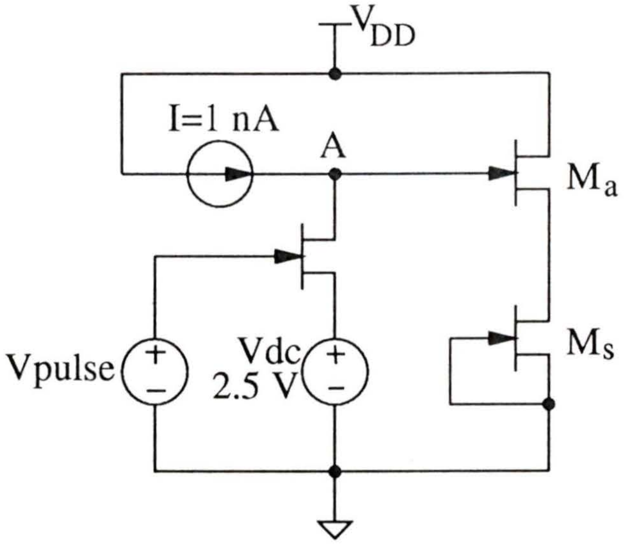

Figure 5.3 Simulation circuit to get the input gate capacitance

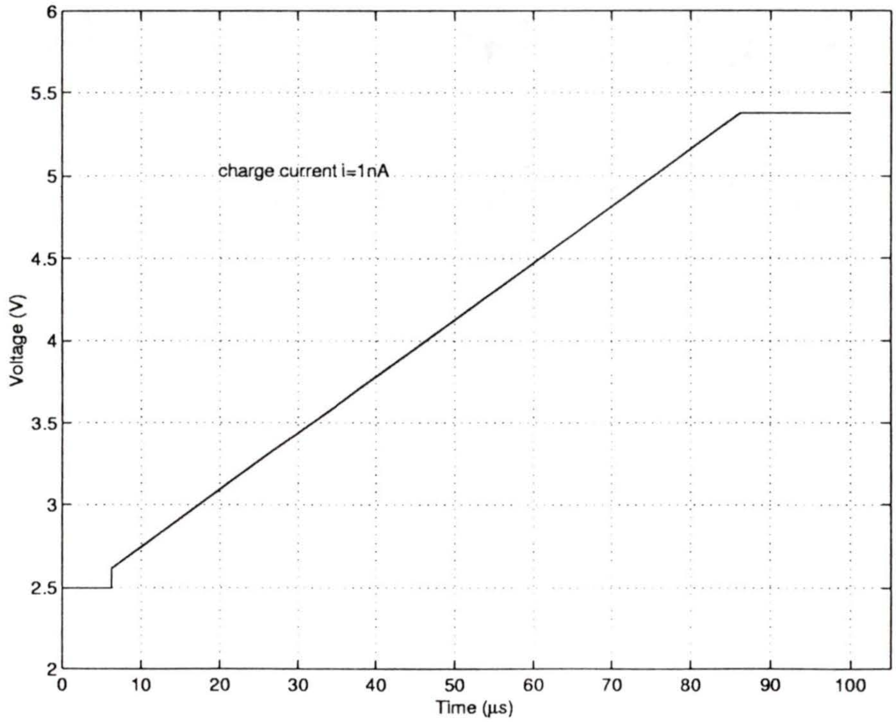

Figure 5.4 Simulation result of the input gate capacitance

Equation (5.8) is used to calculate C_d. Since C_d is a function of the applied voltage, we choose a voltage value equal to 0.5 V to obtain the mean value of C_d which is 64 fF. Therefore, the total capacitance connect to the diffusion node is about 95 fF. Thus, using Equation (5.6), the reset noise is about 123 rms electrons. This is quite a large noise source.

5.2.1.2 Flicker Noise or $1/f$ Noise

Flicker noise was discovered by Johnson in 1925 and interpreted by Schottky in 1926 [47]. Because the noise spectrum varies as $1/f^a$, with a close to unity, one often uses the name $1/f$ noise instead of flicker noise. The $1/f$ noise in a CCD is usually associated with the fast interface state trapping and can be related to the thermal noise if the characteristic frequency f^* is known [47].

$$\overline{v_n^2}_{1/f} = \overline{v_n^2}_{thermal}\left(1 + \frac{f^*}{f}\right) \tag{5.11}$$

In [46], the $1/f$ noise in CCD was simplified as

$$\overline{v_n^2}_{1/f} = \frac{4kT\Delta B\alpha}{g_m} \tag{5.12}$$

where α is a constant which depends upon the gate and drain voltages, their dopings, etc. and g_m is the transconductance of the device. For a MOSFET, g_m is given by

$$g_m = \mu C_{ox}\left(\frac{W}{L}\right)(V_{gs} - V_{th}) \tag{5.13}$$

where μ is the carrier mobility in semiconductor, C_{ox} is the oxide capacitance per unit area and V_{th} is the threshold voltage of the MOSFET.

For a MESFET, g_m is given by

$$g_m = q\mu N_D d\frac{W}{L}\left(1 - \left(\frac{V_{bi} - V_G}{V_{po}}\right)^{1/2}\right) \tag{5.14}$$

where d is the thickness of the active layer, V_G is the gate voltage and V_{po} is the pinch-off voltage which is given by

$$V_{po} = \frac{qN_D d^2}{2\varepsilon} \tag{5.15}$$

Thus, the equivalent noise in term of electrons for the CCD $1/f$ noise is

$$\overline{N_{e1/f}} = \frac{C_{total}}{q}\overline{v_{n1/f}} \tag{5.16}$$

where C_{total} is the total capacitance connected to the floating diffusion node. From Equation (5.12) and we see that an increase in g_m will decrease the noise. That is the reason why we always use a large (*W* is large) transistor as the source follower. For the GaAs RGCCD used in this study, $d = 0.24\mu\mathrm{m}$, $\mu = 8000 cm^2/V \cdot s$, $N_D = 5 \times 10^{16}/cm^3$ and $W/L = 50$. Using the Equation (5.14) and (5.15), we can find g_m of the MESFET source follower which is 74.6 *mmho*. Assuming ΔB is 100 MHz, α is 1 and C_{total} is 95 fF calculated above, therefore the $1/f$ noise is about 3 electrons,.

5.2.1.3 Correlated Double Sampling

From the analysis above, we can see that the reset noise of the floating diffusion sensing scheme is quite large. It is important to minimize this noise where low noise performance is required. The correlated double sampling signal processing method (CDS), some times called correlated clamp-sample-and-hold method (CCSH), has been developed to remove *kTC* noise from the signal in floating diffusion charge detection circuits, Figure 5.5 shows the output structure of the CCD with CDS connected to a floating diffusion charge detection node [48].

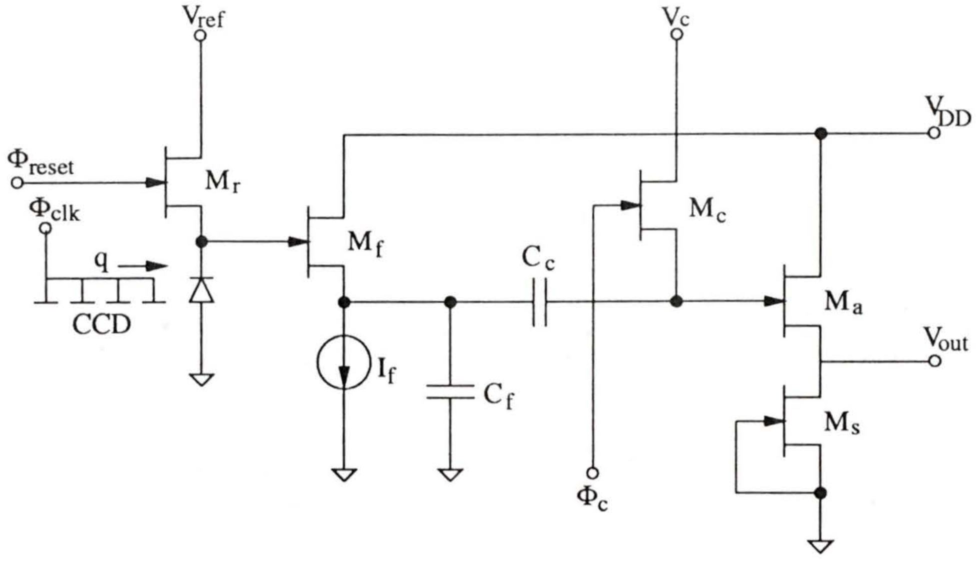

Figure 5.5 Circuit diagram of the CDS connected to a floating diffusion node

The operation of this circuit can be divided in three basic cycles: In the first cycle, the floating diffusion diode is reset by turning on the reset transistor M_r and allowing the potential of the floating diffusion diode to equalize with the reference voltage. In the second cycle, the reset transistor is turned off and the diode node is allowed to float. The potential on the floating diffusion diode in this interval corresponds to a zero signal. However, it has an added component of the thermodynamic fluctuations superimposed on this level as described by Equation (5.5). In the third cycle, charge packet from the CCD transport gate is transferred onto this diode and is sensed as it changes the diode potential. This signal together with the *kTC* noise of the detection node reset level are coupled to the gate of the source-follower M_f and further through the coupling capacitor C_c. In the meantime, the clamping transistor M_c is turned on. This changes the charge on the coupling capacitor C_c and resets the voltage on this node to the new reference level V_c. The signal from the detection node, induced by the charge transfer from the CCD, is always referenced to this reset level. By carefully designing the circuit parameters, the *kTC* noise coupled on the capacitor C_c can be made almost the same but with an opposite polarity.

This circuit therefore can remove *kTC* noise very effectively. The noise in term of electrons is given by [48]

$$N_e = \frac{1}{F}\frac{\sqrt{kTC}}{q} \tag{5.17}$$

where the factor *F* expresses how many times the CDS signal processing method reduces the *kTC* noise which would otherwise be observed on the floating diffusion alone. *F* can be as high as 70 [48]. Therefore we can see that the CDS method is very effective at removing the *kTC* noise. For example, if we add a CDS circuit to the floating diffusion output of the GaAs RGCCD as shown in Figure 5.1, the *kTC* noise can be reduced to as low as 2 electrons. But this low level is quite difficult to achieve since the timing requirement is very high. Usually after using the CDS circuits, the *kTC* noise of the floating diffusion charge sensing scheme can be reduced to about 20 electrons.

5.2.2 Linearity

The output voltage of the floating diffusion sensing scheme is

$$V_{out} = A_v\frac{Q_{sig}}{C_{fd}} \tag{5.18}$$

where Q_{sig} is the injected signal charge, C_{fd} is the total capacitance at the floating diffusion node, A_v is the voltage gain of the source follower which is less than one. In the ideal case, V_{out} should be linear with the injected signal charge Q_{sig}, but actually, it is not true. There are two elements should be considered when we discuss the linearity of the floating diffusion sensing scheme, one is the transfer characteristic of the source follower, another is the capacitance of the floating diffusion node C_{fd}.

5.2.2.1 Source Follower

The small signal gain (A_v) of source follower is given by [49]

$$A_v = \frac{g_{ma}}{\frac{g_{ma}}{\alpha_a} + \frac{1}{r_{dsa}} + \frac{1}{r_{dss}}} \tag{5.19}$$

where r_{dsa} and r_{dss} are the drain resistances associated with transistors M_a and M_s which are shown in Figure 5.1, g_{ma} is the transconductance of the transistor M_a and α_a is the body-effect gain factor which is a constant. When the signal charge packets are small, $r_{dsa} \approx r_{dss} \gg 1/g_{ma}$, therefore the gain of the source follower can remain as a constant α_a. But when the signal charge packets increase, the operating point of the source follower drops and as a result, the gain of source follower A_v will decrease. Therefore this gives the non-linearity of the source follower. Figure 5.6 shows the simulation results of the source follower using the same size as we have tested in the GaAs RGCCD. We can see that when the input voltage approaches 4 V, the output of source follower becomes non-linear. But compared to the non-linearity of the floating diffusion capacitance, this non-linearity is very small and only effects large signals.

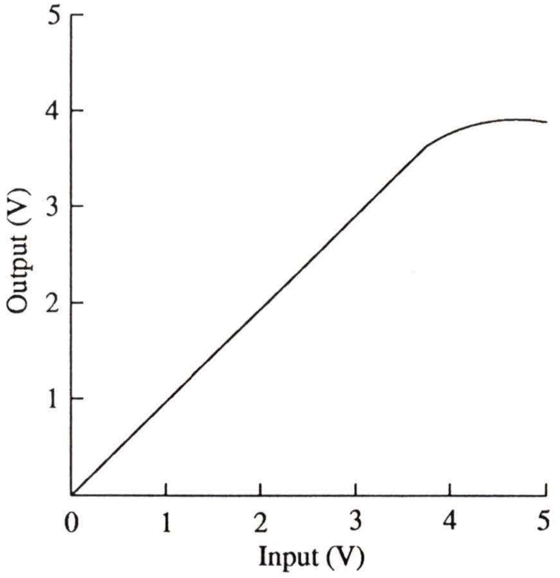

Figure 5.6 DC transfer curves of source follower

5.2.2.2 Floating Diffusion Node Capacitance

As we discussed above, the floating diffusion node capacitance includes all the capacitances connected to this node. The total capacitance C_{fd} can be computed using Equation (5.7) and (5.8). Therefore, the signal output voltage of the floating diffusion node is given by

$$V_{out} = \frac{Q_{sig}}{C_{fd}} \tag{5.20}$$

solving the Equation (5.7), (5.8) and (5.20), we can see that the capacitance becomes larger as the injected signal charge increases, therefore, the output voltage of the floating diffusion node is non-linear with the signal charge. For the floating diffusion sensing scheme shown in Figure 3.1 and the parameters of the GaAs RGCCD we tested in the Chapter 3, the simulation results of the output voltage versus signal charge are shown in Figure 5.7. If we assume that at the CCD input section, a 1 V signal input generates 1,000, 000 electrons, the output voltage versus input voltage is shown in Figure 5.8. Comparing Figure 5.8 with Figure 3.8, it shows that the measurement and the simulation results agree quite well, and shows the non-linearity of the floating diffusion sensing. Therefore, in floating diffusion sensing scheme, the main problem related to the non-linearity is the floating diffusion node capacitance.

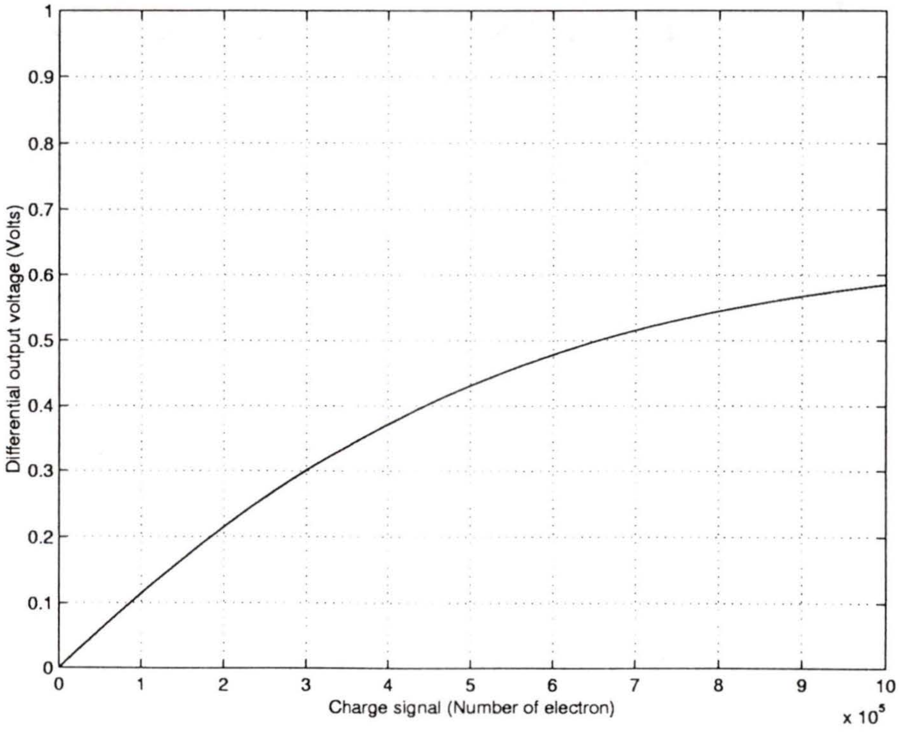

Figure 5.7 Simulation result of the signal charge and output voltage

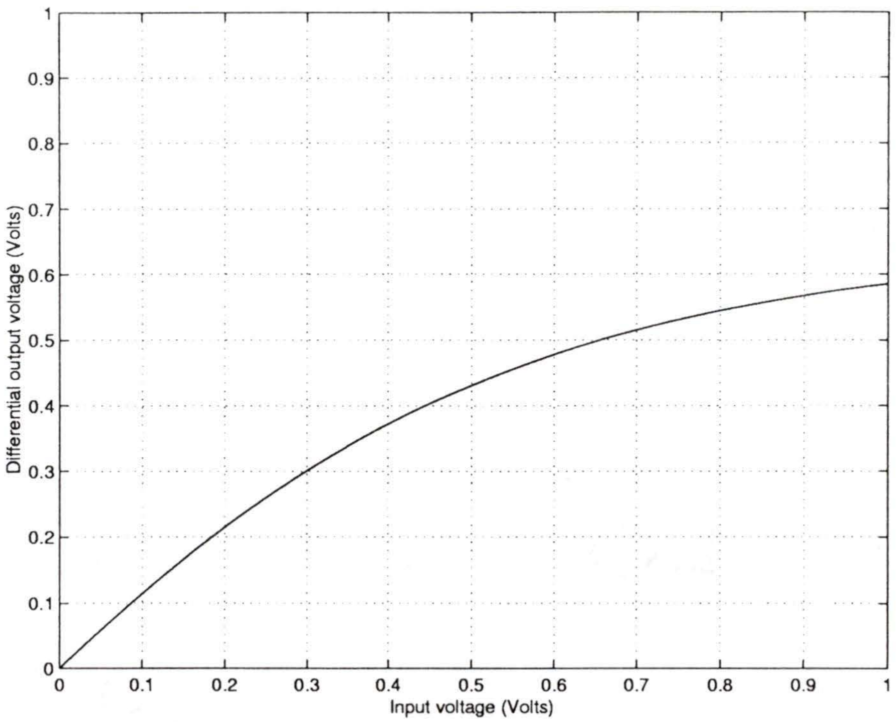

Figure 5.8 Simulation result of the input voltage and output voltage

5.3 Floating Gate Sensing

An alternative technique for sensing the size of a signal charge packet is to use a floating gate above the signal charge transferred channel which is shown in Figure 5.9. This is a non-destructive charge sensing method [19]. The charge packets transfer under the CCD electrode in the normal way, except that the CCD electrode above the floating gate is held at a fixed bias voltage rather than being clocked (thus, this method is not suitable for a three-phase CCD). When the charge packet is stored under the floating gate plate, the capacitance between the sensing plate and the substrate is increased. Since the floating gate is isolated, a fixed amount of charge is stored in the plate and the increase of the capacitance causes a decrease of the voltage. This voltage variation is then detected by an on-chip transistor. Thus this scheme can detect the signal charge without destroying them. This is the principle how the floating gate charge sensing scheme works.

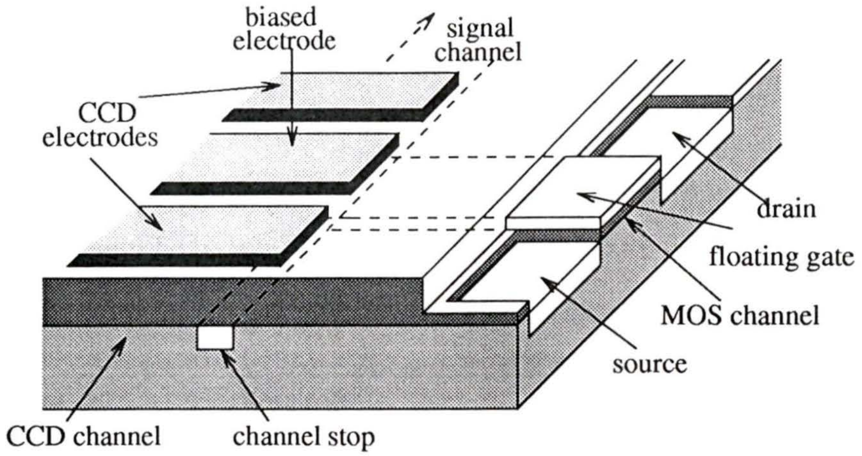

Figure 5.9 General scheme of a floating gate sensing technique

5.3.1 Noise Analysis

The floating gate charge detection is non-destructive and, therefore, does not generated *kTC* noise. It mainly has two noise sources, one is Johnson noise and, the other is $1/f$ noise. For $1/f$ noise, it is the same as we analysis in section 4.2 and can use the Equation (5.16) to calculate the noise, therefore floating gate has similar $1/f$ noise to the floating diffusion.

For Johnson noise, it is given by [47]

$$N_{ee}^2 = \frac{kTC_p}{q^2} \cdot \frac{(1 + C_g/C_p)}{C_g/C_p} \cdot \frac{\omega_b L_g^2}{\mu(V_g - V_{th})} \tag{5.21}$$

where L_g is the length of the transistor, μ is the mobility of electron in semiconductor, C_g is the input gate capacitance of the transistor, C_p is the parasitic capacitance connected to the floating gate, ω_b is the angular frequency of operation and V_g is the applied gate voltage. The minimum noise N_{ee} is reached when $C_p = C_g$. Therefore the minimum noise becomes

$$N_{ee}^2 = \left(\frac{kTC_g}{q^2}\right) \cdot \frac{4\omega_b L_g^2}{\mu(V_g - V_{th})} \tag{5.22}$$

thus the minimum noise performance of the floating gate is primarily determined by its parasitic capacitance C_p. For a typical geometry of the MOSFET used in CCD floating gate output circuit, $L_g = 1\mu\text{m}$, $C_g = 31 fF$, $f_b = 150$ MHz, the noise is about 4 electrons.

5.3.2 Linearity

The equivalent circuit of floating gate is shown in Figure 5.10. The injected signal charge Q_{sig} produces a change in potential, $\Delta\phi_s$, of value

$$\Delta\phi_s = \frac{Q_{sig}}{C_b + \dfrac{C_c(C_p + C_g)}{C_c + C_p + C_g}} \tag{5.23}$$

where C_b is the total channel bulk capacitance, C_c is the floating gate to channel capacitance, C_g is the input equivalent capacitance of the MOSFET source follower and C_p is the parasitic capacitance. The output voltage of the floating gate is then given by

$$\begin{aligned} V_{out} &= A_v \cdot \frac{C_c}{C_c + C_p + C_g} \cdot \Delta\phi_s \\ &= A_v \cdot \frac{Q_{sig}}{C_b + (C_p + C_g)(1 + C_b/C_c)} \end{aligned} \tag{5.24}$$

The effect of the source follower on linearity is the same as it in floating diffusion sensing. The capacitance connected to the floating gate plays a significant role in the linearity of the CCD output. C_c, C_g and C_p are not changed with the injected signal charge, but C_b is a voltage-dependent depletion capacitance and Equation (5.8) can be used to calculate the capacitance. Assuming the transfer gate is $3\mu\text{m} \times 10\mu\text{m}$, the source follower is the same size as it in floating diffusion sensing scheme ($1\mu\text{m} \times 50\mu\text{m}$), the simulation results of the output voltage versus signal charge is shown in Figure 5.11. From the result we can see that the floating gate charge sensing scheme also suffers from the non-linearity problem. It is the same as in the floating diffusion. Also, the floating gate has less detection sensitivity than the floating diffusion. That is for the same output voltage, it requires more injected signal charge (compare Figure 5.7 with Figure 5.11). This is because of the larger capacitance connected to the floating gate.

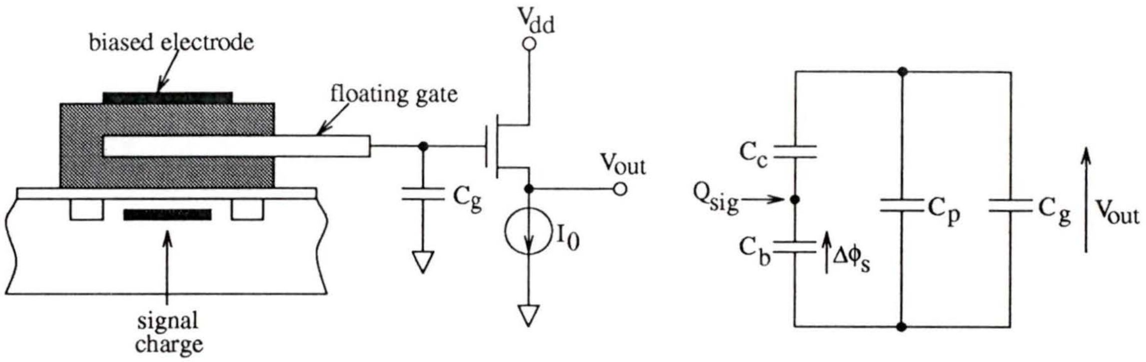

Figure 5.10 Equivalent circuit of floating gate sensing technique

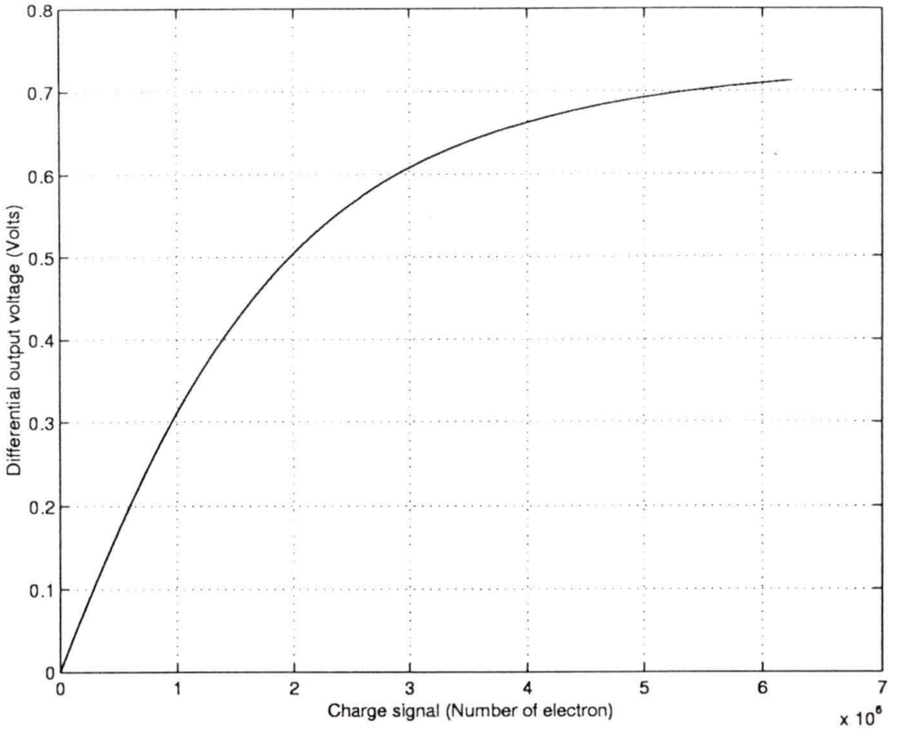

Figure 5.11 Simulation result of the signal charge and output voltage

5.4 Current Output Sensing Scheme

Another charge sensing scheme is to use a current-sensitive amplifier to connect to the floating diffusion node instead of the source follower. This sensing scheme is not commonly used in the CCD because of its complex structure [29]. I designed and simulated the current output scheme using BiCMOS 0.8 μm technology so we can compare all the different CCD output structures. Figure 5.12 shows this current output structure, it consists of a current-sensitive amplifier with a feedback capacitance C_{fb} and a reset switch S_{reset}. The detailed circuit diagram of the current-sensitive amplifier is shown in Figure 5.13 and the sizes of the transistors are listed in Table 5.1. The simulation results for open-loop gain for this amplifier is shown in Figure 5.14

Due to the Miller effect on the feedback capacitance C_{fb}, its capacitance can be made extremely small to obtain low-noise and high sensitivity performance. The operation of this circuits can be divided into two cycles. Firstly, the signal charge is transferred into the diffusion node, then it is coupled by the feedback capacitor to get the output voltage which varies with the signal charge. Secondly, the reset switch turned on to discharge the feedback capacitor to prepare for the next signal charge.

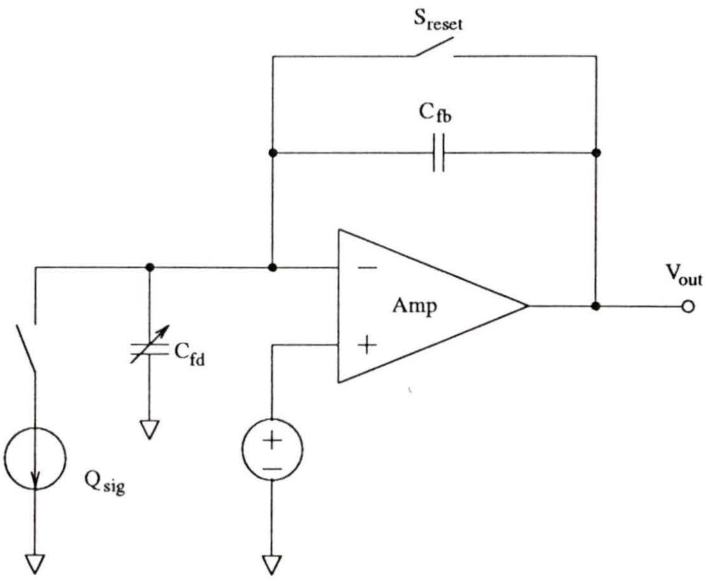

Figure 5.12 Current output sensing structure

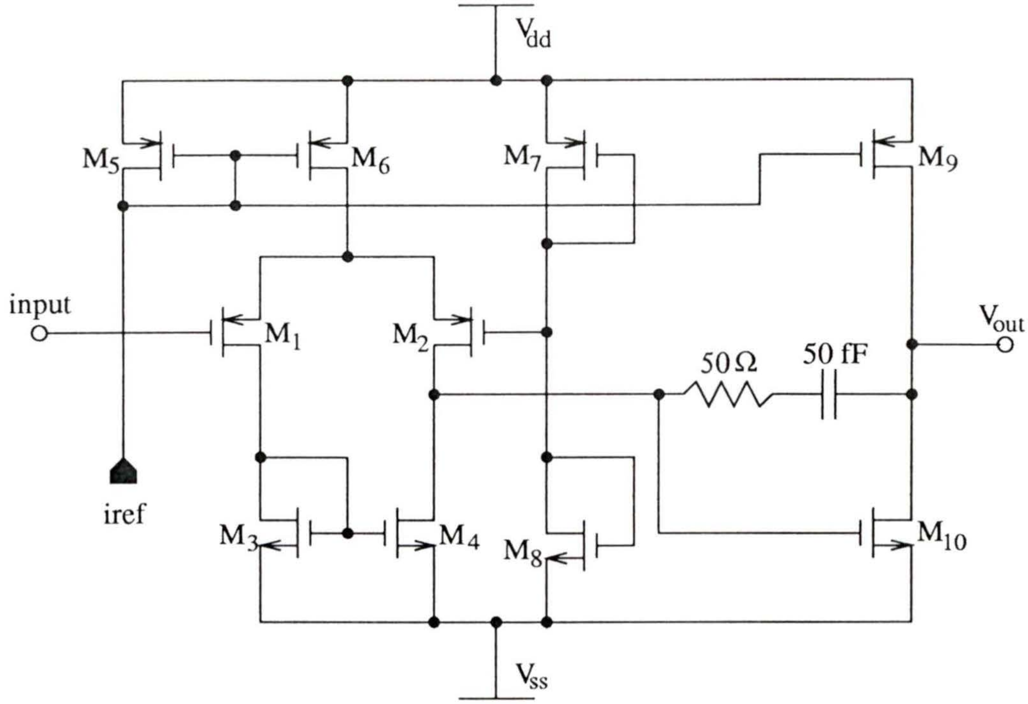

Figure 5.13 Circuit diagram of the current-sensitive amplifier

Table 5.1. The size of the transistor for current-sensitive amplifier

Name	M1	M2	M3	M4	M5	M6	M7	M8	M9	M10
W/L	10	10	5	5	10	10	45	5	10	10

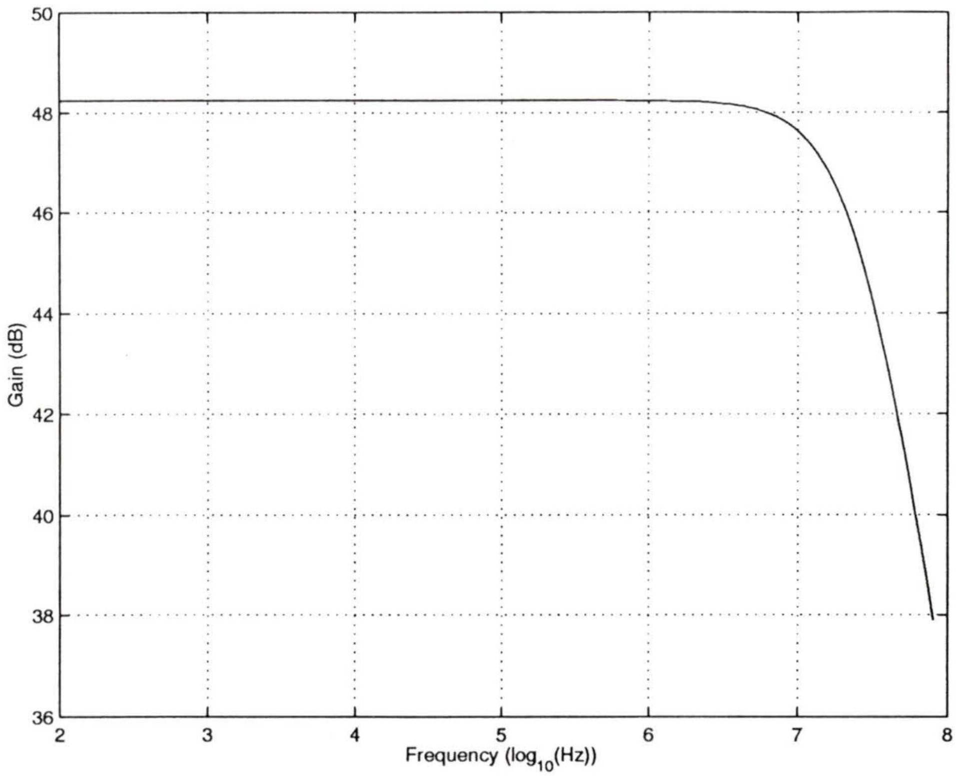

Figure 5.14 Open-loop gain of the designed amplifier

5.4.1 Noise Analysis

There are two main noise components in the current output sensing. One is the reset noise and other is the flicker noise. For the reset noise, it can be use Equation (5.6) to calculate the noise. In the circuit design, we let the $C_{fb} < C_{fd}$ to decrease the reset noise and, in the meantime, to increase the sensitivity. In this design the C_{fb} is 40 fF, therefore the reset noise is about 80 rms electrons. Compared to the floating diffusion scheme, the reset noise has been reduced. In order to further reduce the reset noise, a CDS stage can be used.

For the flicker noise in the current output circuit, we also can use Equation (5.12) and (5.16) to calculate it. Using the parameters in this design, that is g_m is 11.1 mmho, C_{total} is 40 fF, therefore the flicker noise is about 4 electrons.

5.4.2 Linearity

According to the Miller effect, the charge-to-voltage conversion of the current output circuits is

$$V_{out} = \frac{Q_{sig}}{C_{fb} \parallel C_{fd}/A} \tag{5.25}$$

where C_{fd} is the total capacitance connected to the floating diffusion node, C_{fb} is the feedback capacitance shown in Figure 5.12 and A is the charge-sensitive amplifier open-loop gain. In this design, C_{fb} is in the same order of the C_{fd}, while $A \geq 48$ dB. Thus, the capacitance C_{fd} becomes negligible compare with C_{fb}. Therefore Equation (5.25) can be rewritten as

$$V_{out} = \frac{Q_{sig}}{C_{fb}} \tag{5.26}$$

The feedback capacitor C_{fb} can be made a constant capacitance over a wide temperature and voltage range, thus the linearity has been significantly improved in the current output sensing scheme. Figure 5.15 shows the simulation results of the circuit. From the results we can see that the circuit has a good linearity over the whole range of the input charge.

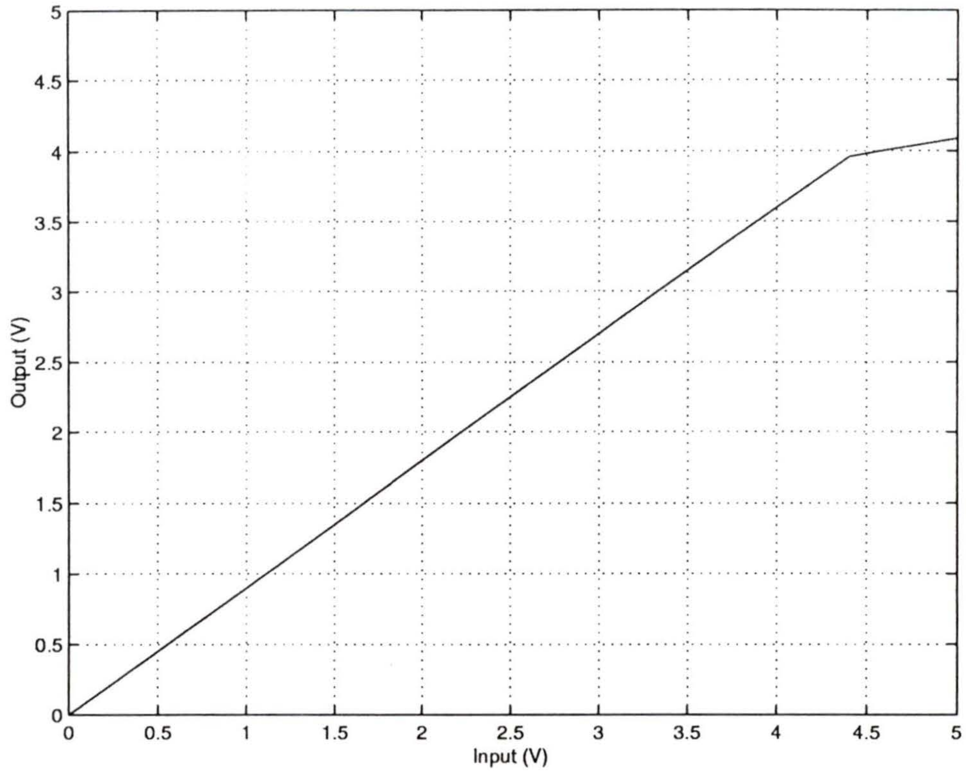

Figure 5.15 DC transfer curve of charge-sensitive amplifier

5.5 Conclusion

From the analysis we can see that the three output structures have their own advantages and disadvantages. The floating diffusion has the simplest circuit structure but has a large noise and poor linearity. The floating gate is a non-destructive charge-sensing method with low noise but also has poor linearity. The current output sensing has the best linearity and relatively low noise but has a very complex circuitry structure, the operation speed of the CCD system is also limited by the amplifier. Table 5.2 lists all the comparison results.

Table 5.2. The comparison results of the three output structures

Output	Noise	Linearity	Sensitivity	Needs CDS	Circuit complexity
Floating diffusion	Large	Poor	High	Yes	Simple
Floating Gate	Low	Poor	Low	No	Simple
Current output	Medium	Good	High	Yes	Complex

Chapter 6

Compression Circuit for CCD Imager

6.1 Introduction

This chapter describes an analog data compression circuit to reduce the amount of data captured by a CCD imager. By integrating a compression function onto the CCD imager, the image signal to be read out from the CCD is significantly reduced. The potential applications of this circuit are in high speed imaging, such as high frame-rate image sensing and high-resolution image sensing [50][51].

The compression scheme used here is a conditional replenishment scheme [52]. At the readout circuit of CCD, the output voltage of each CCD pixel is compared to that in the previous value. The value and the address of the CCD pixel are extracted if the magnitude of the difference is greater than a threshold. This is called fixed threshold compression. The circuits and simulation results are described in the following.

6.2 Conditional Replenishment

The conditional replenishment method, which was first proposed by F. W. Mounts, is used for image compression [52]. The scheme of conditional replenishment works as follows: current CCD pixel values are compared to those of the last replenished frame stored in another CCD analog memory. If the difference is greater than the threshold, then the pixel values and addresses are extracted. These values are used to update the value in the CCD analog memory. Otherwise, the pixel values and addresses are not outputted and the CCD analog memory value remains the same. Figure 6.1 shows the architecture of the circuit.

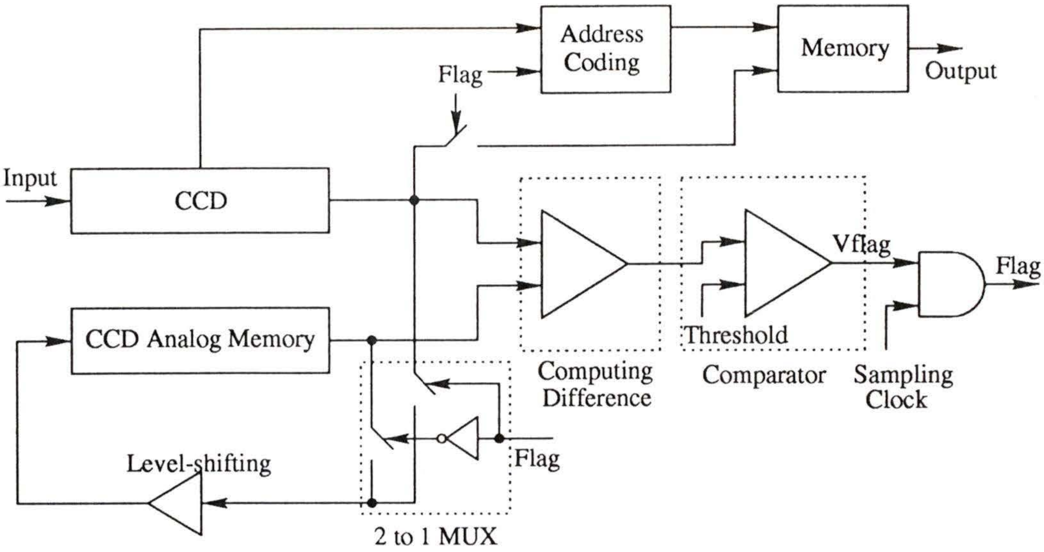

Figure 6.1 The architecture of the compress circuit

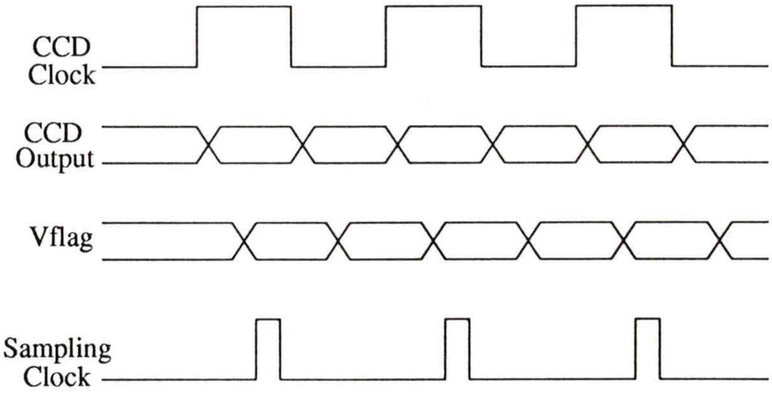

Figure 6.2 The timing of the compress circuit

There are two ways to achieve the conditional replenishment, one is called fixed threshold, the other is fixed rate. For the fixed threshold method, the threshold is fixed and the output data rate is varied. The output SNR (Signal to Noise Ratio) is kept above the value determined by the threshold. The number of pixel values that are sent to the output is changed, but it is stationary within the same scene. For the fixed rate method, the threshold are allowed to change to keep the rate, and it changes rapidly when a scene change occurs, but also tend to be stationary in the same scene [50]. In this chapter, we implement a fixed threshold compression circuit for CCD imager.

6.3 Circuit Design and Analysis

6.3.1 Voltage-to-Current Converter

The output signal of the CCD is a voltage, so a Voltage-to-Current converter is needed to convert the voltage to current first. Figure 6.3 demonstrates a simple Voltage-to-Current circuit diagram [54]. This is essentially a single-ended output differential amplifier. The analysis below shows that if the input differential voltage satisfies certain conditions, the output current will change linearly with the input voltage.

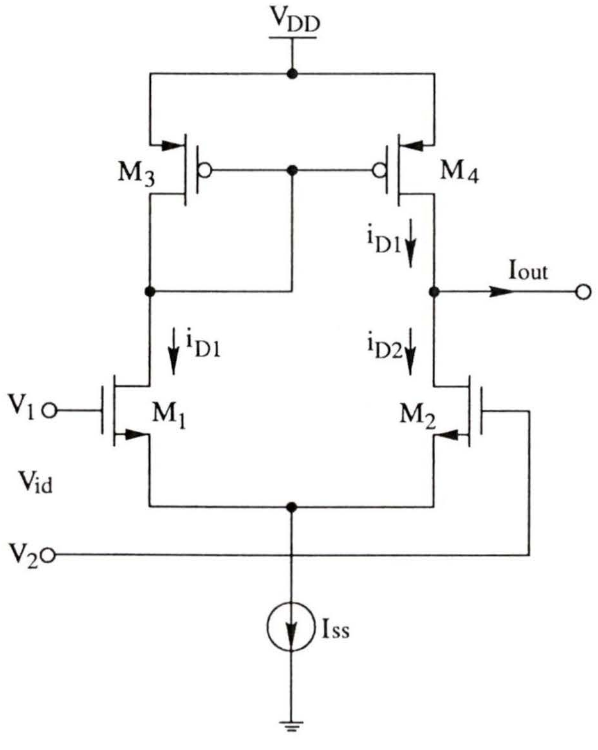

Figure 6.3 Simple Voltage-to-Current converter

M1 and M2 are the input transistors connected differentially. M3 and M4 form a current mirror. V_1 and V_2 are the input voltage signals. i_{D1} and i_{D2} are the current going through the two input transistors M1 and M2. The differential input voltage is:

$$\begin{aligned} V_{id} &= V_1 - V_2 \\ &= V_{GS1} - V_{GS2} \\ &= V_{t1} + \sqrt{\frac{2i_{D1}}{\beta_1}} - V_{t2} - \sqrt{\frac{2i_{D2}}{\beta_2}} \end{aligned} \tag{6.1}$$

where V_t is the threshold voltage and β is the transconductance parameter of the MOS transistors. Usually $V_{t1} = V_{t2}$ and $\beta_1 = \beta_2 = \beta$, so

$$V_{id} = \sqrt{\frac{2i_{D1}}{\beta}} - \sqrt{\frac{2i_{D2}}{\beta}} \tag{6.2}$$

Since

$$I_{ss} = i_{D1} + i_{D2} \tag{6.3}$$

Solving Equation (6.2) and (6.3), we can get the expressions for i_{D1} and i_{D2}

$$i_{D1} = \frac{I_{ss}}{2} + \frac{I_{ss}}{2}\sqrt{\frac{\beta V_{id}^2}{I_{ss}} - \frac{\beta^2 V_{id}^4}{4I_{ss}^2}} \tag{6.4}$$

$$i_{D2} = \frac{I_{ss}}{2} - \frac{I_{ss}}{2}\sqrt{\frac{\beta V_{id}^2}{I_{ss}} - \frac{\beta^2 V_{id}^4}{4I_{ss}^2}} \tag{6.5}$$

Since M3 and M4 form a current mirror, the current going through M4 is the same as the one going through M3 which is i_{D1}. therefore the output current is:

$$\begin{aligned} i_{out} &= i_{D1} - i_{D2} \\ &= I_{ss}\sqrt{\frac{\beta V_{id}^2}{I_{ss}} - \frac{\beta^2 V_{id}^4}{4I_{ss}^2}} \end{aligned} \tag{6.6}$$

If $\frac{\beta V_{id}^2}{I_{ss}} \gg \frac{\beta^2 V_{id}^4}{4I_{ss}^2}$, then

$$i_{out} \cong \sqrt{\beta I_{ss}} V_{id} \tag{6.7}$$

For each transistor, for example M1,

$$i_{D1} = \frac{\beta}{2}(V_{gs1} - V_{t1})^2 \tag{6.8}$$

the transconductance is $g_{m1} = \sqrt{2i_{D1}\beta}$, since $i_{D1} \approx I_{ss}/2$,

$$g_{m1} = \sqrt{I_{ss}\beta} \tag{6.9}$$

Putting Equation (6.9) into (6.7), we can get the output current

$$i_{out} \cong g_{m1} V_{id} \tag{6.10}$$

It is noted that the output current changes linearly with the change of the input voltage.

In the practical circuit, I_{ss} is chosen to be 150 μA and V_{id} should be less than 2.8V. Figure 6.4 shows the actual circuit, which is a cascode current mirror (high output impedance) instead of simply current mirror shown in Figure 6.3. The size of the transistors is shown in Table 6.1. Figure 6.5 is the transfer characteristic of the voltage-to-current converter. The range of V_{id} is from 0 to 1000 mV. When the input voltage is 0 V, the output current is about 0.1 μA and this can compensate the offset error in the current comparator stage.

Table 6.1. The size of the transistors for Voltage-to-Current converter

Transistor	M1	M2	M3	M4	M5	M6	M7	M8
W/L	4	4	50	50	50	50	20	20

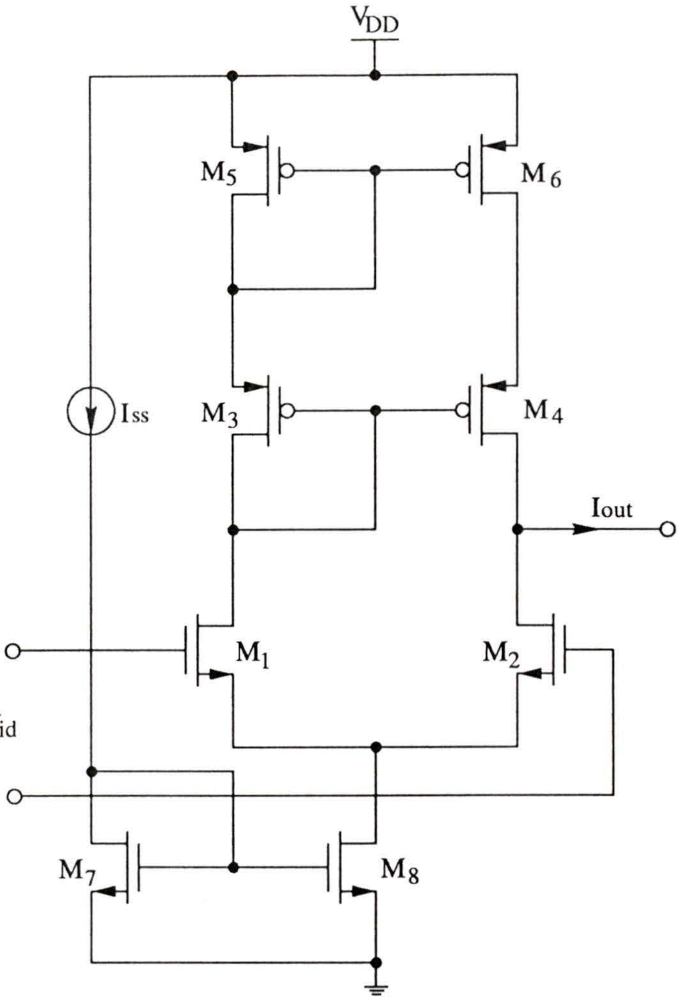

Figure 6.4 Voltage-to-Current converter

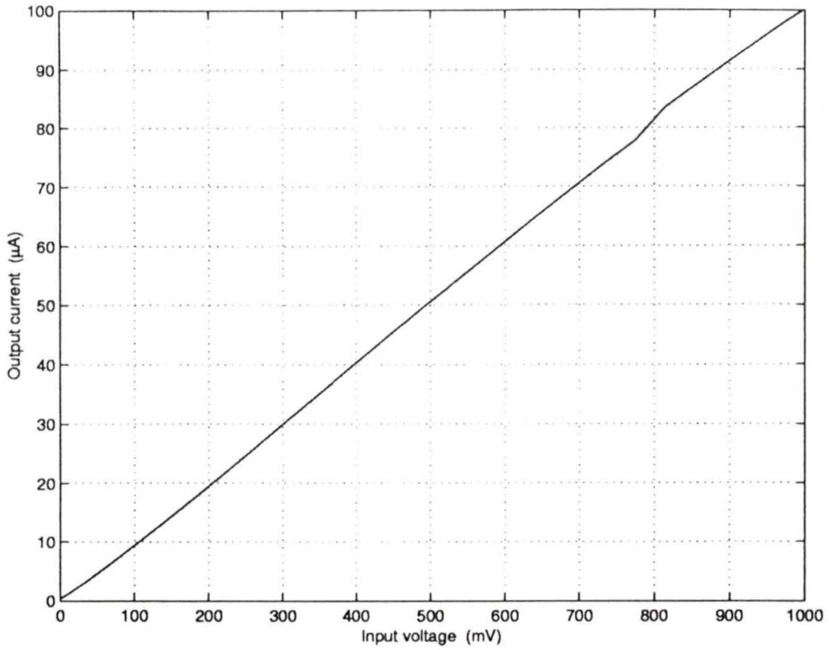

Figure 6.5 Transfer characteristic of Voltage-to-Current converter

6.3.2 Current Mirror [53]

A basic continuous-time MOS N-type current mirror is shown in Figure 6.6 [54]. It is made of two matched transistors. One transistor M1 is connected as a diode and it works in saturation region. It produces a reference current I_{ref} given by:

$$I_{ref} = \frac{\beta_1}{2}\left(\frac{W_1}{L_1}\right)(V_{gs1} - V_t)^2(1 + \lambda_1 V_{ds1}) \tag{6.11}$$

Similarly, the output current I_{out} from M2 is given by:

$$I_{out} = \frac{\beta_2}{2}\left(\frac{W_2}{L_2}\right)(V_{gs2} - V_t)^2(1 + \lambda_2 V_{ds2}) \tag{6.12}$$

where β is the transconductance parameter of the transistors, W/L is the width-length ratio of the channel region for the transistors, V_t is the threshold voltage of the transistors and λ is the channel-length modulation factor of the MOS transistors.

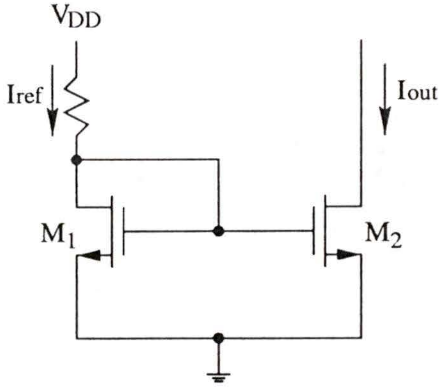

Figure 6.6 Simple current mirror

From the circuits we can see that $V_{gs1} = V_{gs2}$. Since both transistors are fabricated simultaneously, β_1 and β_2 are the same. If λ_1 and λ_2 are close to zero, the output current I_{out} will be related to input current I_{ref} as:

$$\frac{I_{out}}{I_{ref}} = \frac{W_1/L_1}{W_2/L_2} \tag{6.13}$$

Since the gate of the MOS transistor is an open circuit under DC condition, there are no current errors in MOS current mirrors if the channel length modulation factor λ is zero. But in a practical circuit, λ is not zero and is in inversely proportional to the transistor channel length L. Therefore, from Equation (6.12) we can see that the output current I_{out} also depends on the drain-source voltage V_{ds}. The changes in the V_{ds} will create an output current error. In order to reduce the channel length modulation effect, the simplest way is to increase the channel length. But, this will increase the size of the MOS device and the parasitic capacitances. The speed of the circuit can not be made very fast. The accuracy is also not very good.

In order to eliminate the side effects on the simple current mirror, a lot of current mirror structures have been proposed, such as cascode current mirror, dynamic current mirror, *etc*. Here we use a new structure of the current mirror which can greatly reduce the channel length modulation effect. It has a high speed at small current and the accuracy also meets the requirement. Figure 6.7 shows such a P-type current mirror. Table 6.2 shows the size of the transistors. M1 and M2 are mirror transistors, M3 and M5 form a loop to keep the drain-source voltage of M1 to be constant. M4 and M6 form another loop to keep the drain-source voltages of M2 to be constant [55]. M7 and M8 are used to eliminate the voltage changes at the input and output ports. Since M3 and M4 both operate in saturation region, the drain-source voltages of M1 and M2 are

$$V_{dsM_1} = V_{gsM_3} = V_t + \sqrt{\frac{2I_1L_3}{\beta W_3}} \tag{6.14}$$

$$V_{dsM_2} = V_{gsM_4} = V_t + \sqrt{\frac{2I_2L_4}{\beta W_4}} \tag{6.15}$$

If we choose $I_1 = I_2$ and $W_3/L_3 = W_4/L_4$, we can see that $V_{dsM_1} = V_{dsM_2}$. Therefore, From Equation (6.11) and (6.12) we can see that the output current I_{out} will be the same as the input current I_{ref}. Figure 6.8 shows the simulation result of the difference between the input current I_{ref} and the output current I_{out}. The maximum relative error is less than 0.34% (*i.e.* 8 bit accuracy) when the input current from 0 to 100 uA. Figure 6.9 shows the simulation results for the transient response for the pulse input, from the results we can see that, the delay between the output current and the input current is less than 50 ns for the small current from 0 to 10 μA. I also simulated other kinds current mirrors such as cascode current mirror, Wilson current mirror *etc.* [49][54], these current mirrors all work very slowly (several hundreds of microseconds) with small currents. Therefore, this circuit is much faster than other kinds of current mirrors with a small current input.

Table 6.2. The size of transistors for current mirror

Transistor	M1	M2	M3	M4	M5	M6	M7	M8
W/L	2	2	18	18	22	22	2	2

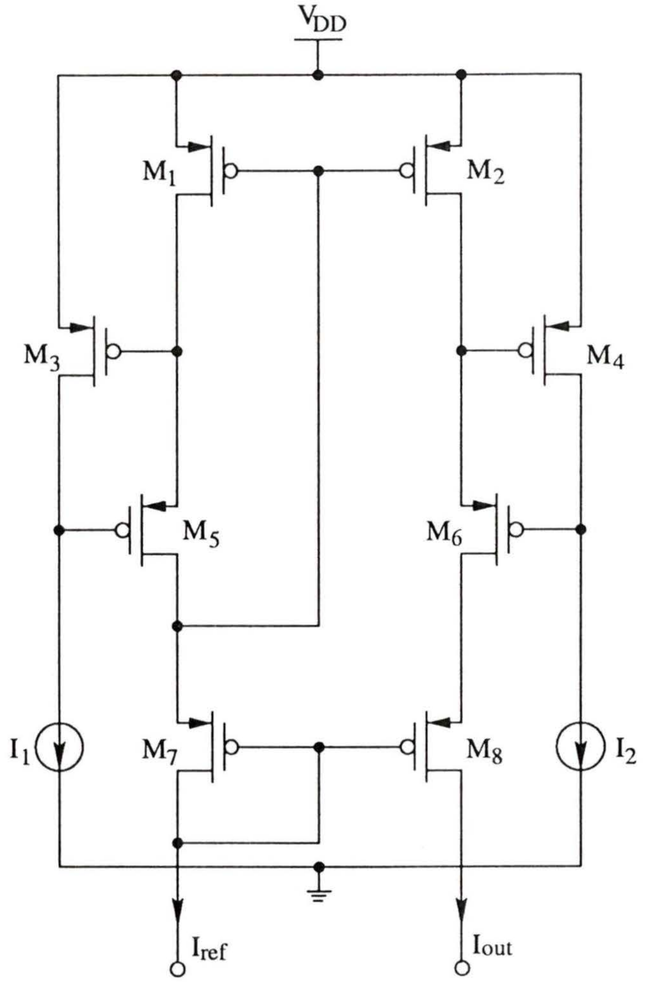

Figure 6.7 P-type current mirror

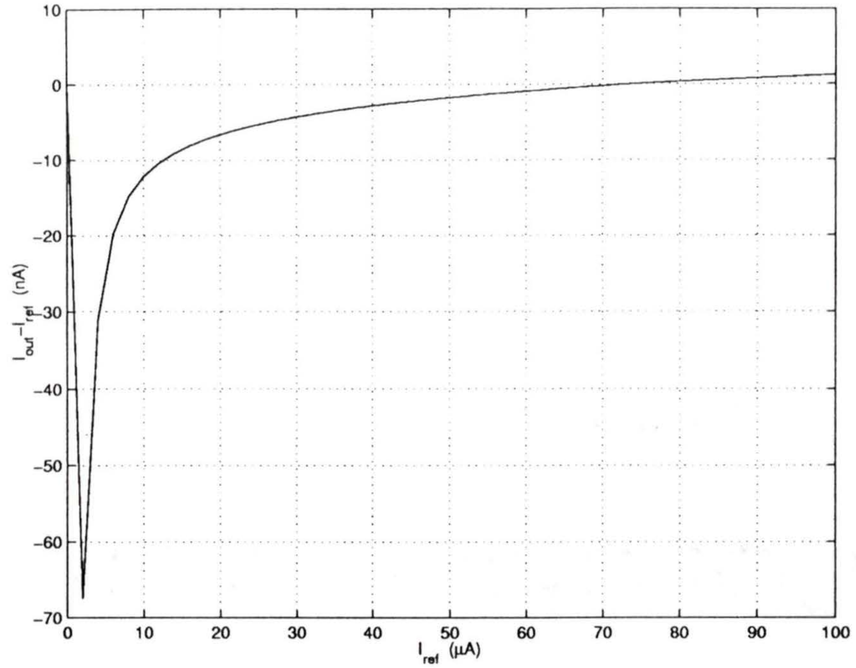

Figure 6.8 Output error versus reference current for current mirror

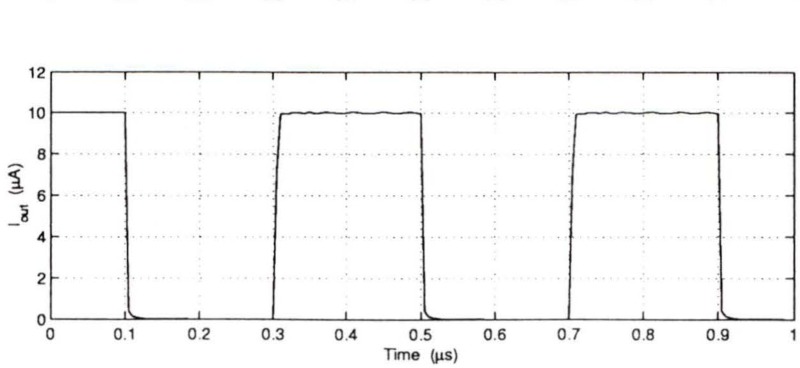

Figure 6.9 Transient response of the current mirror

6.3.3 Current Comparator

After the absolute difference value of the input is obtained, it should be compared with the threshold, therefore, a current comparator is need. The basic requirement for the current comparator in this work is its sensitivity. It should be very sensitive when the value of input current is around the value of threshold current.

Figure 6.10 shows the schematic diagram of a cascode current comparator. M1 to M4 form a P-type cascode current mirror to produce a threshold current I_{th} to the output side. M5 to M8 form another N-type cascode current mirror to reproduce the input current I_{in} to the output and compare it with the threshold current I_{th}. M9 and M10 form an inverter here used to determine the comparison result. If $I_{in} < I_{th}$, the voltage of node A will reach V_H and output of inverter will change to LOW, giving $Vflag = 0$. If $I_{in} \geq I_{th}$, the voltage of node A will reach value V_L and the output of inverter will be HIGH, giving $Vflag = 1$. Table 6.3 shows the size of transistors for the current comparator.

Table 6.3. The size of transistors for current comparator

Transistor	M1	M2	M3	M4	M5	M6	M7	M8
W/L	30	30	30	30	12.5	12.5	12.5	12.5

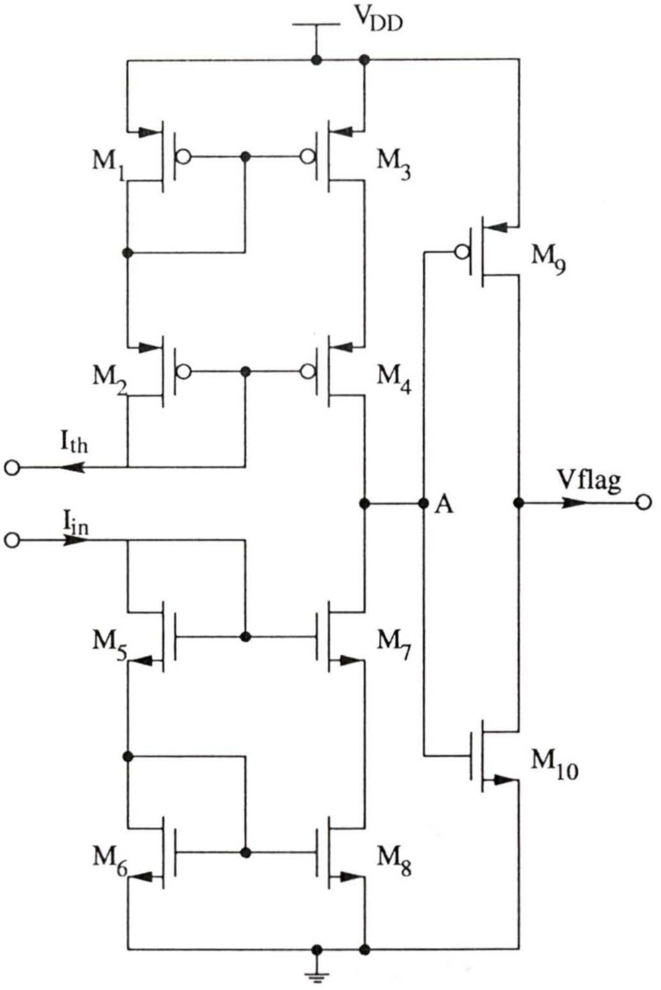

Figure 6.10 The schematic diagram of the cascode current comparator

Figure 6.11 shows the results of input-output transfer characteristics at different threshold current points. When the input current I_{in} is bigger than the threshold current I_{th}, the *Vflag* signal will change the state from the logical LOW (0 V) to logical HIGH (5 V). We inputted a triangular current with a range between I_{th} and $I_{th} - I_{th}/256$ (the resolution requirement is 8 bit) to do the sensitivity simulation. The simulation results show that when I_{th} is from 10 uA to 100 uA, the resolution of the current comparator is 8 bit, which meet the requirements. Figure 6.12 and Figure 6.13 show the simulation results for the sensitivity of the current comparator at 10 μA and 100 μA. When we apply a pulse input signal and compare with I_{th}, we can check the speed of the current comparator. From the results shown in Figure 6.14 we can see that, the delay time from the input signal to output signal is less than 60 ns.

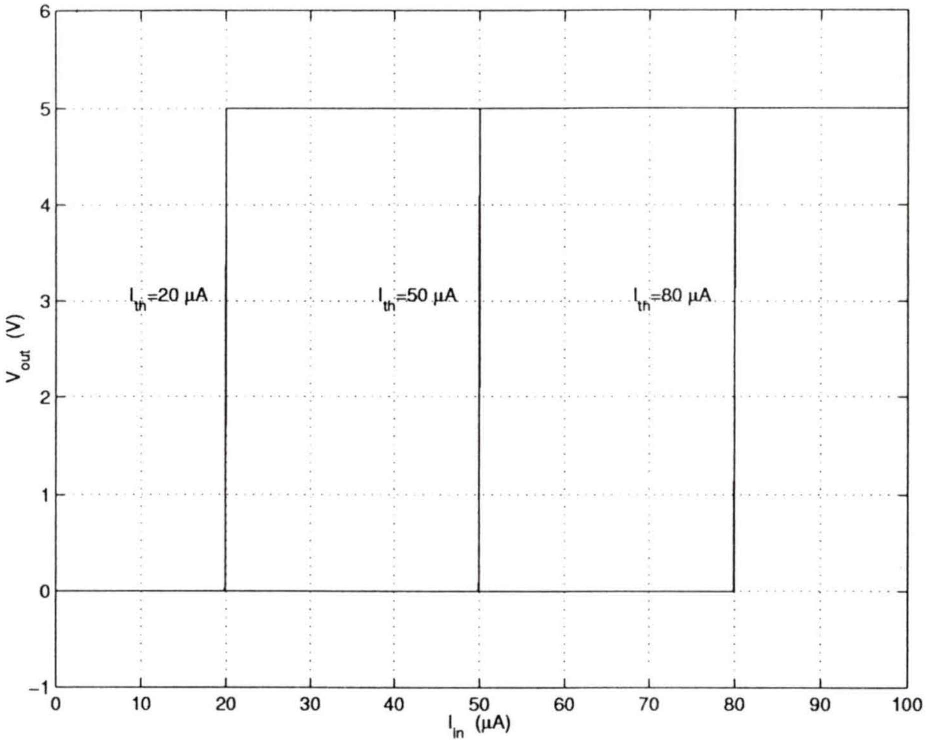

Figure 6.11 Input-output transfer characteristic of three different threshold current

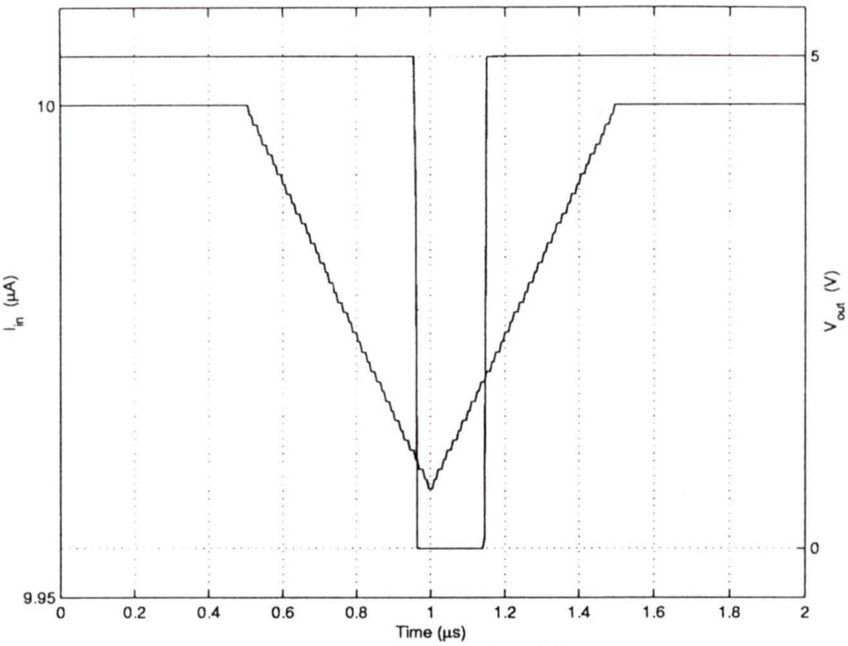

Figure 6.12 Sensitivity simulation for the I_{th}=10 µA

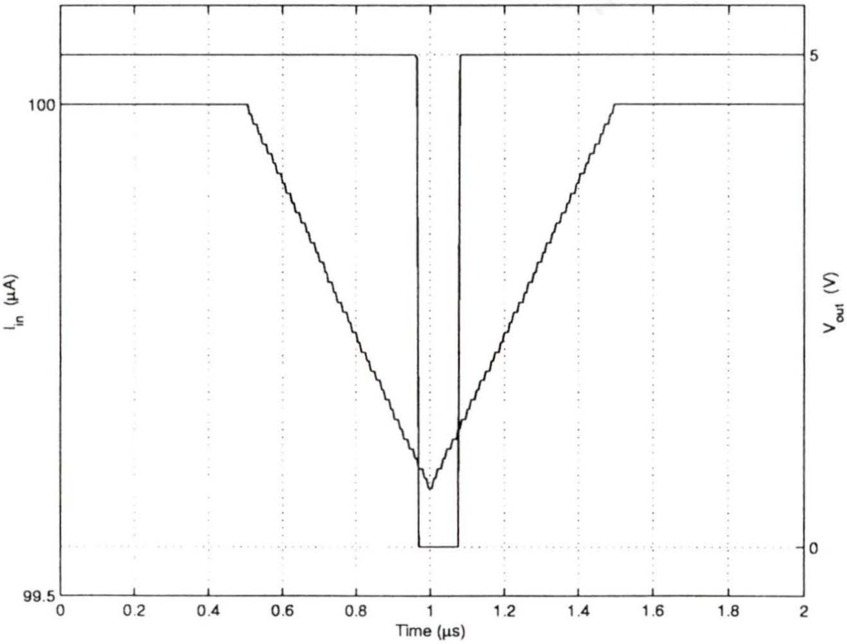

Figure 6.13 Sensitivity simulation for the I_{th}=100 µA

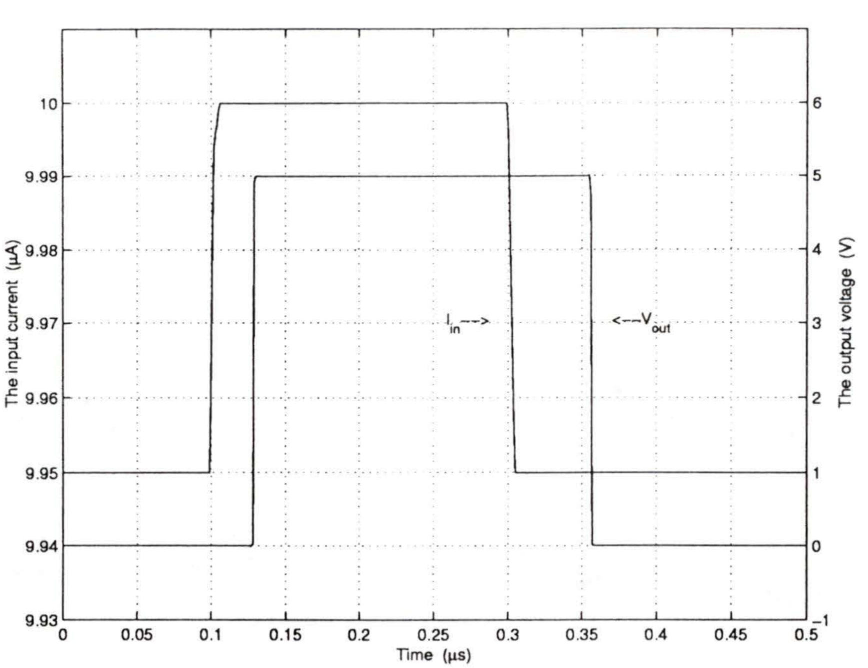

Figure 6.14 Transient response of the current comparator

6.3.4 Coding Circuit

When the *Flag* signal is HIGH, the signal in CCD pixel is transferred to the output. Therefore, we need a coding circuitry to indicate which CCD pixel has the output to go out. Since here we use a 128 pixels CCD, a 7 bit coding circuit is enough to code the addresses of all the CCD pixels. When the *Flag* signal is HIGH, the coding circuit gives a 7 bit digital number to indicate the address of the CCD pixel, otherwise, the coding circuit gives an all zero output. Figure 6.15 shows the schematic of the coding circuit, the circuit consists of inverters, NAND gates, AND gates, CMOS transfer gates and D flip-flops. Their schematic diagrams are shown in Figure 6.16 to Figure 6.19 [54][56].

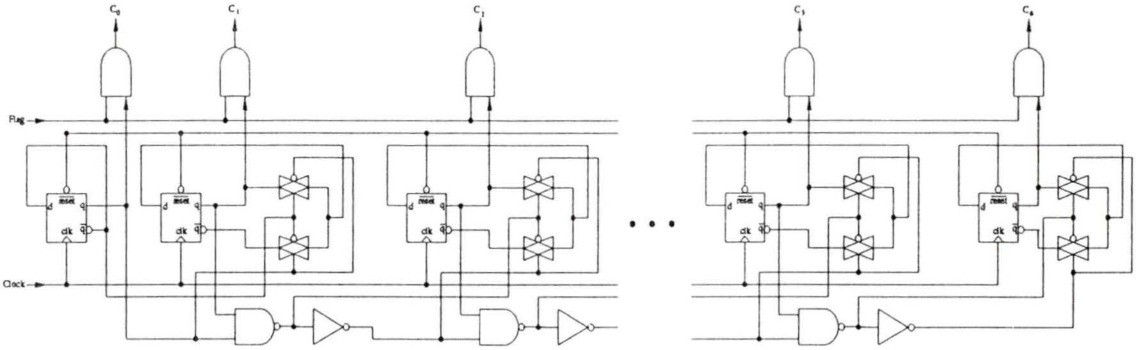

Figure 6.15 The schematic of the coding circuit

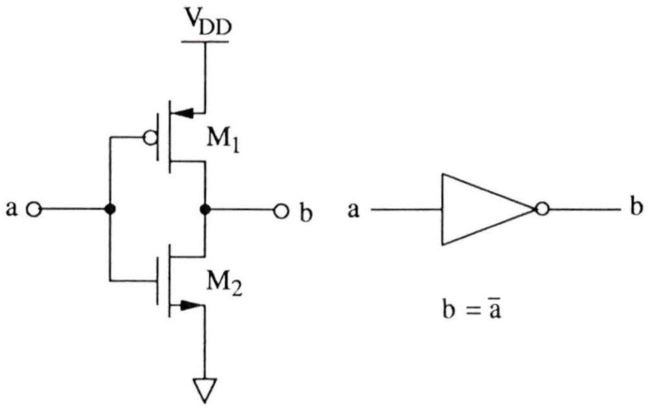

(a) (b)

Figure 6.16 Inverter (a) Schematic diagram (b) Symbol

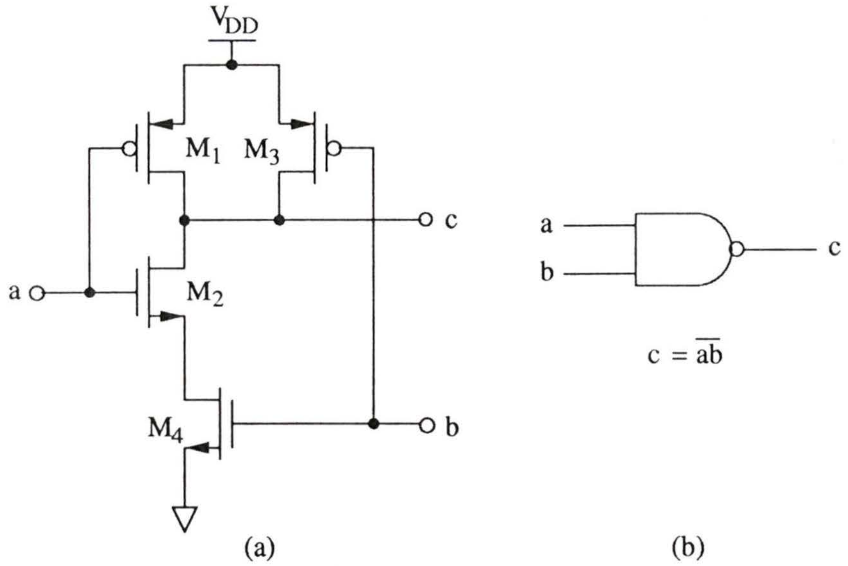

Figure 6.17 2-input nand gate (a) Schematic diagram (b) Symbol

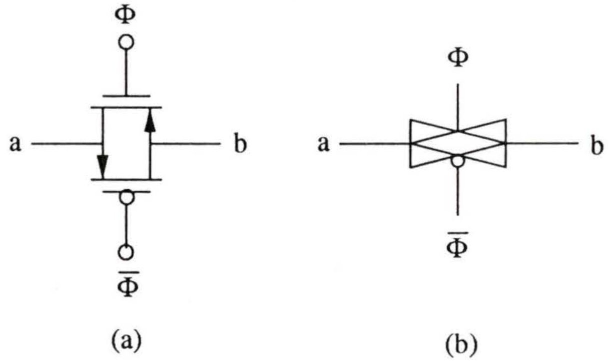

Figure 6.18 CMOS transfer gate (a) Schematic diagram (b) Symbol

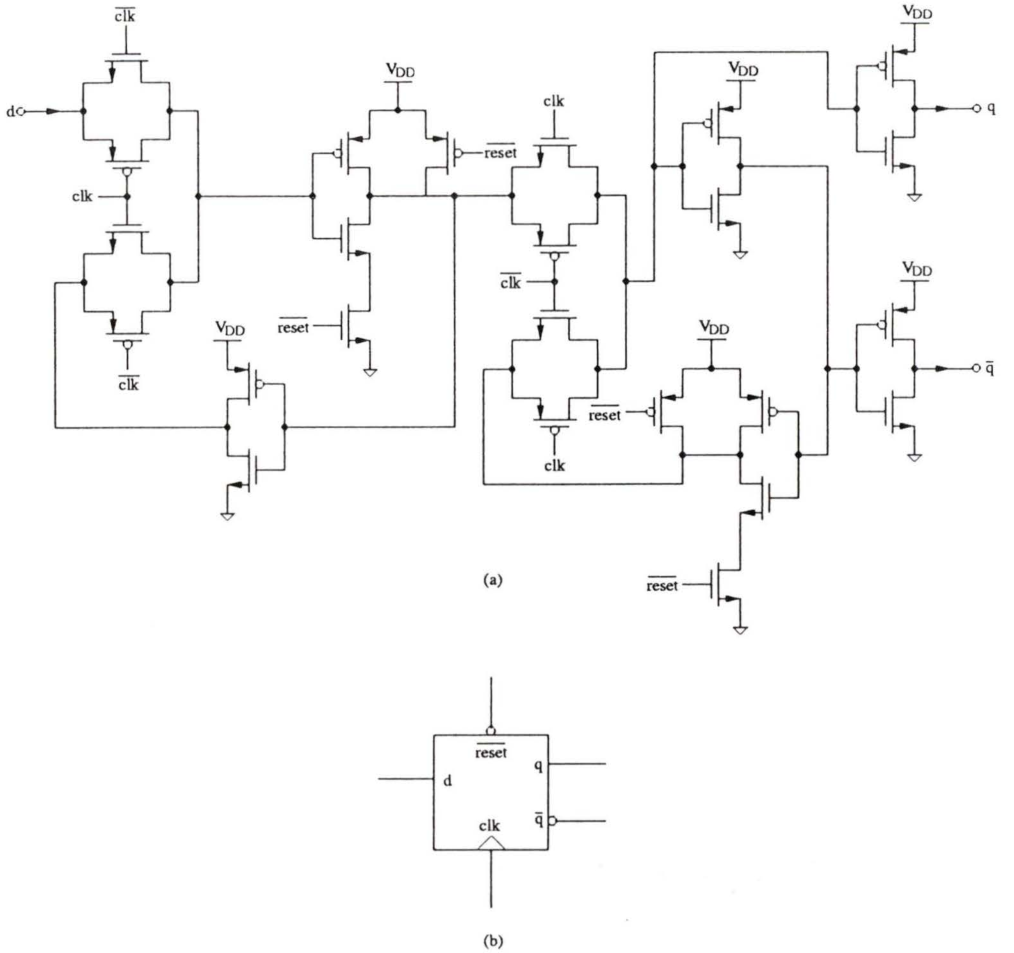

(a)

(b)

Figure 6.19 D flip-flop (a) Schematic diagram (b) Symbol

The clock used in the coding circuit is the same as the CCD drive clock. After the reset signal, all the outputs C_0 to C_6 are set to zero. Then, each clock pulse increases the output by one, each corresponding to one output signal from CCD. If the output signal from CCD is sent out, which means the *Flag* signal is HIGH, the outputs C_0 to C_6 will give the address of that CCD pixel, otherwise, the output of the coding circuit C_0 to C_6 will be set to zero by the *Flag* signal. The address and the output signal will be stored in the memory and sent out. Figure 6.20 shows the simulation results of the first four clock cycles. When the *Flag* signal is HIGH, the outputs C_0 to C_2 give the corresponding address, when the *Flag* is LOW, the outputs are zero.

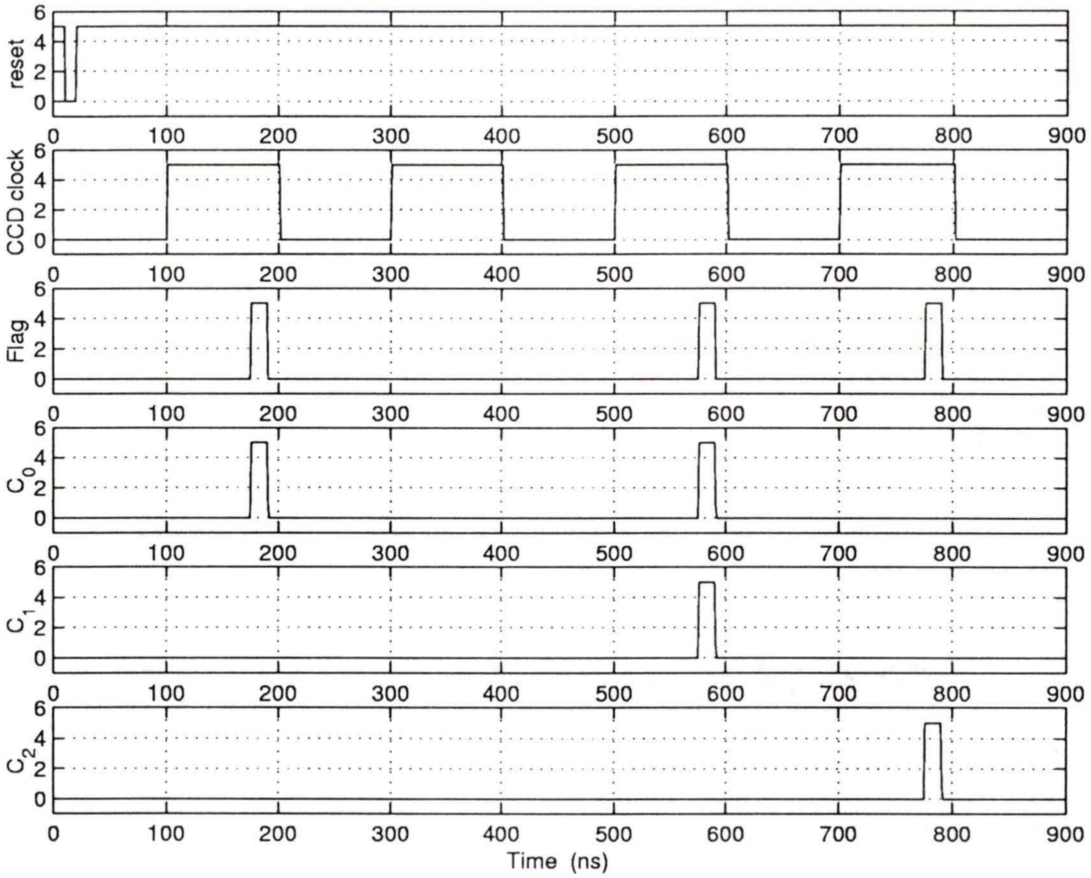

Figure 6.20 Simulation results of the coding circuit

6.3.5 System Simulation

The entire system consists of Voltage-to-Current converters, current mirrors, a current comparator and a coding circuit. The system can work at 5 MHz and the resolution of the circuit is 8 bit. Figure 6.21 shows the circuit diagram of the implement of the conditional replenishment method. Figure 6.22 shows the resolution simulation results for the circuit. When the absolute value of difference between the current CCD pixel value and the previous CCD pixel value (V_{diff}) is equal to 3.9 mV, the circuits can distinguish them and send the CCD signal out. Since the output range of the CCD is 1 V, the resolution of the circuit is 8 bit. Figure 6.23 shows the simulation results for the fixed threshold is 20 mV. When V_{diff} is bigger than 20 mV, the *Flag* signal is HIGH. When V_{diff} is lower than 20 mV, the *Flag* is LOW. Table 6.4 lists the simulation results of the first 10 CCD pixels, the threshold value is set to be 10 mV. From the simulation results we can see that the circuit meets the requirements.

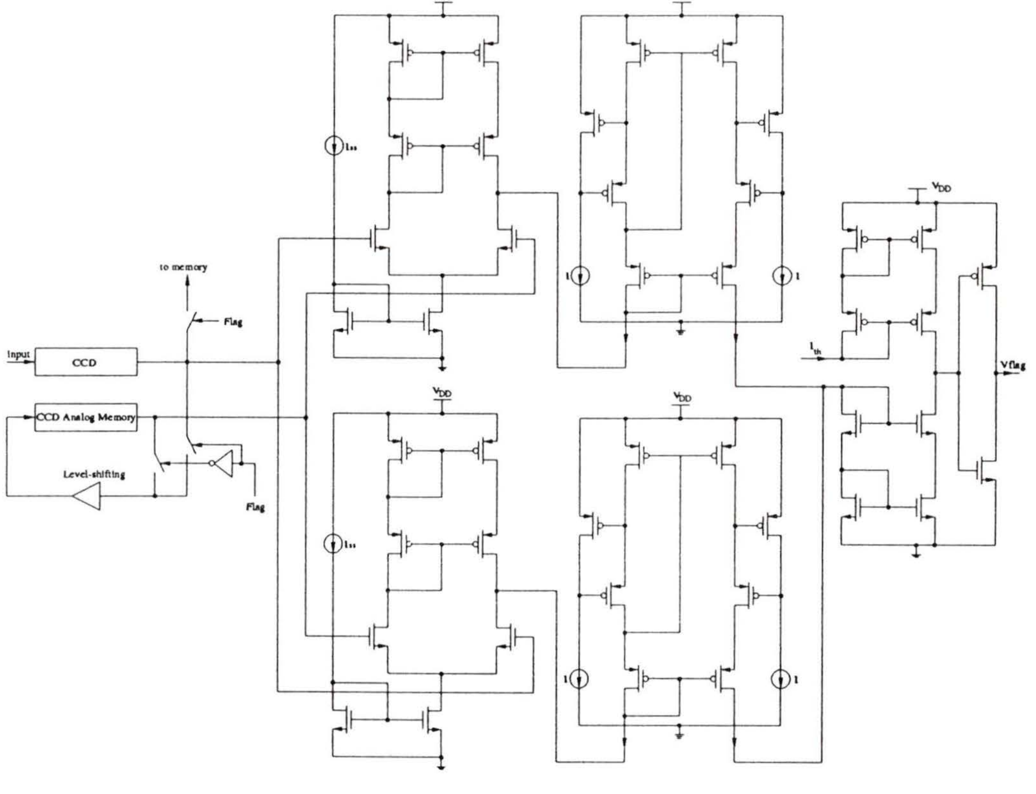

Figure 6.21 An analog circuit of the implement of conditional replenishment

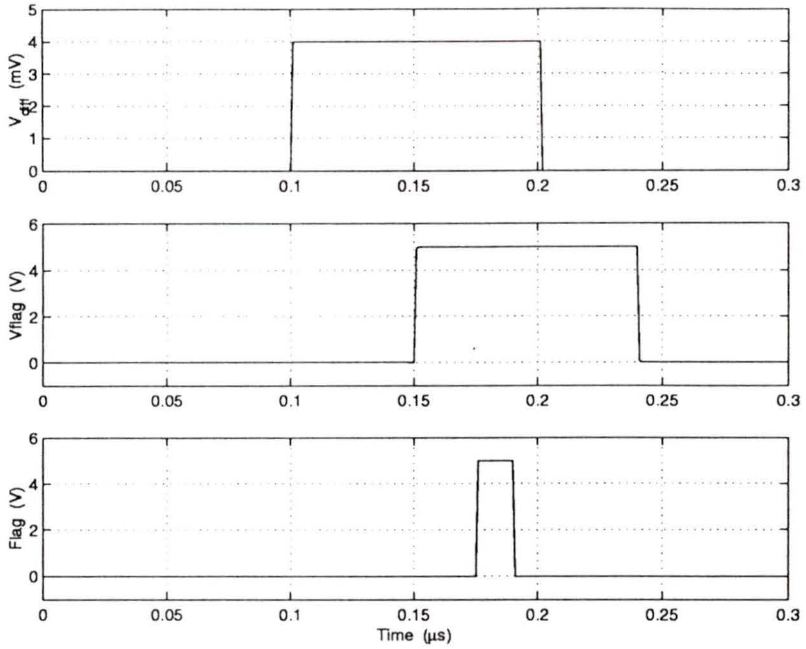

Figure 6.22 Resolution simulation for the circuit

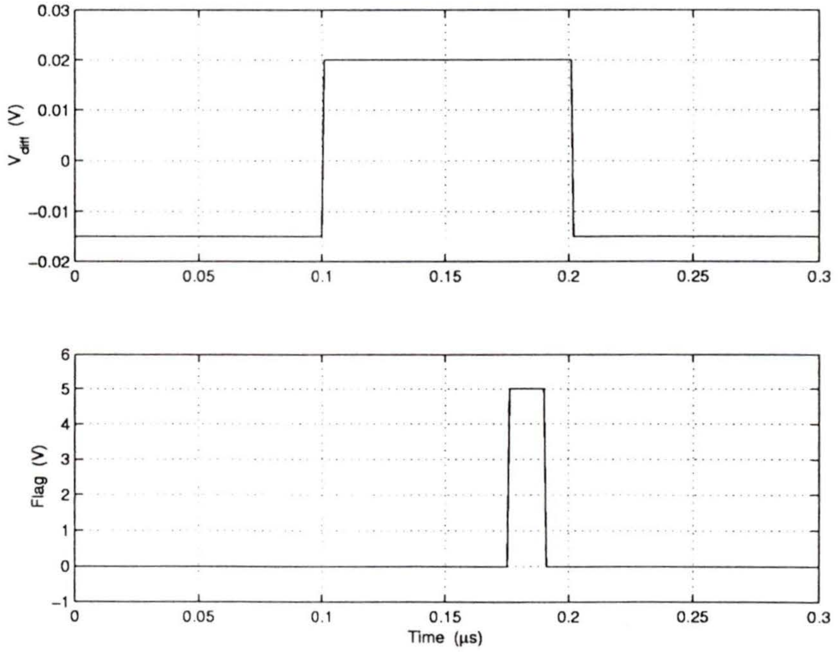

Figure 6.23 Simulation results for the circuit

Table 6.4. Simulation results of the System circuit

Precious value (V)	2.00	2.20	2.24	2.50	2.70	2.80	3.00	2.60	2.40	2.30
Current Value (V)	2.03	2.21	2.25	2.504	2.70	2.803	2.90	2.60	2.40	2.28
Flag (V)	5	5	5	0	0	0	5	0	0	5
C_0	1	0	1	0	0	0	1	0	0	0
C_1	0	1	1	0	0	0	1	0	0	1
C_2	0	0	0	0	0	0	1	0	0	0
C_3	0	0	0	0	0	0	0	0	0	1

For very high rate imaging or very high resolution imaging, the high bandwidth to transfer data from the CCD is a bottle neck. By using this compression system in CCD imager, the image signal which has to be read out from the CCD can be significantly reduced, therefore, the pixel rate of CCD can be increased. We can set different threshold value and get different compression ratio and resolution. It can achieve a 100:20 compression ratio without significant degradation of the imaging [50].

Chapter 7

Conclusions

7.1 Results

In this work, the GaAs RGCCDs have been tested and analyzed. An equivalent circuit model is used to analyze the effects of the pixel size on the charge transfer efficiency of the GaAs RGCCDs. The electrical and optical properties of the GaAs RGCCDs have been measured. An analysis model is proposed to explain the measurement results. We also discuss and analyze the possible usage of the GaAs RGCCD in an X-ray detector.

The output circuit of the CCD is very important. The three different CCD output circuits, *i.e.* floating diffusion, floating gate and current output sensing scheme, have been compared and discussed. Simulation results are given for the performance of the three different output circuits. The detailed analysis of the noise and non-linearity of the three output circuits are given.

A new architecture for a compression circuit for the CCD imager is proposed. The system circuit is designed and analyzed. Simulation results are given using Spectre under the Cadence environment. The resolution of the system design is verified to be 8-bit. The operation speed of the system circuit is 5 MHz. This novel compression circuit can be used in high rate imaging such as very high frame rate imaging or very high resolution imaging. It also can be used in large area CCD imager.

7.2 Future Work

This work focused on the GaAs RGCCD imager design and CCD related circuit design and analysis. Future work may involve the following:

1. In this work, the tested GaAs RGCCD imager is one dimensional. Two dimensional GaAs RGCCD should be fabricated and tested in future.

2. To verify the analysis, actual measurements for X-rays should be done.

3. Implementation of the three different CCD output circuits to verify the differences in the analysis.

4. Implementation of the compression circuit for the CCD to verify the operation of the circuit.

5. In this work, the speed of the current comparator is not very fast. The whole compression circuit speed is limited by the current comparator. If an adequate higher speed current comparator is designed, the operation speed of the compression circuit will be increased.

Bibliography

[1] Michael Shur, "*Physics of Semiconductor Devices*," Prentice Hall, 1990.

[2] W. W. Hopper and W. I. Lehrer, "An epitaxial GaAs field-effect transistor," *Proc. IEEE*, vol. 55, pp. 1237-1245, 1967.

[3] W. S. Boyle and G. E. Smith, "Charge coupled semiconductor devices," *Bell syst. Tech. J.*, vol. 49, pp. 587-592, 1970.

[4] G. F. Amelio, M. F. Tompsett, *et al.*, "Experimental verification of the charge-coupled devices concept," *Bell syst. Tech. J.*, vol. 49, pp. 593-600, 1970.

[5] F. L. Schuermeyer, R. A. Belt, *et al.*, "New structure for charge-coupled devices," *Proc. IEEE*, vol. 60, pp. 1444-1445, 1972.

[6] I. Deyhimy, J. S. Harris, *et al.*, "GaAs charge-coupled devices," *Appl. Phys. Lett.,* 32 (6), pp. 383-385, 1978.

[7] I. Deyhimy, R. C. Eden, *et al.*, "A 500-MHz GaAs charge-coupled device," *Appl. Phys. Lett.*, 36 (2), pp. 151-153, 1980.

[8] I. Deyhimy, W. A. Hill, *et al.*, "Continuously clocked 1 GHz CCD," *IEEE Electr. Dev. Lett.*, vol. 2, pp. 70-72, 1981.

[9] W. Kwllner, U. Ablassmeier, *et al.*, "A two-phase CCD on GaAs with 0.3-µm-wide electrode gaps," *IEEE Trans. Electron Devices*, vol. 27, No. 5, pp. 1195-1197, 1980.

[10] J. A. Higgins, R. A. Milano, *et al.*, "Resistive-gate GaAs charge-coupled devices," *GaAs IC Symp. Tech. Dig.*, pp. 49-52, 1982.

[11] E. Sovero, R. Sahai, *et al.*, "Microwave frequency GaAs charge-coupled devices," *GaAs IC Symp. Tech. Dig.*, pp. 101-104, 1984.

[12] J. I. Song and E. R. Fossum, "Inhibition of charge packet broading in GaAs charge-coupled devices," *Appl. Phys. Lett.*, vol. 51, No. 9, pp. 1539-1541, 1987.

[13] J. I. Song and E. R. Fossum, "Characterization of evaporated Cr-SiO cermet films for resistive-gate CCD applications," *IEEE Trans. Electron Devices*, vol. 36, No. 9, pp. 1575-1579, 1989.

[14] J. I. Song, D. V. Rossi, *et al.*, "A resistive-gate $Al_{0.3}Ga_{0.7}As/GaAs$ 2DEG CCD with high charge transfer efficiency at 1 GHz," *IEEE Trans. Electron Devices*, vol. 38, No. 4, pp. 930-933, 1991.

[15] V. Fronz, B. Rosner, *et al.*, "Electrical and Structural Properties of Cr-SiO Thin films," *Thin Solid Films*, Vol. 65, pp. 33-43, 1980.

[16] J. Song, E. R. Fossum, "Characterization of Evaporated Cr-SiO Cermet Films for Resistive-Gate CCD Applications," *IEEE Trans. Electron Devices*, Vol. 36, No. 9, pp. 1575-1579, 1989.

[17] R. Bertin, "A preliminary study of GaAs solid state detectors for high energy physics," *Nucl. Instr. and Meth.* A 294, pp. 211-215, 1990.

[18] S. P. Beaumont, "GaAs solid state detectors for particle physics," *Nucl. Instr. and Meth.* A 322, pp. 472-477, 1992.

[19] M. J. Howes and D. V. Morgan, "*Charge-coupled Devices and Systems*," John Wiley & Sons, 1979.

[20] J. D. E. Beynon and D. R. Lamb, "*Charge-coupled devices and their applications*," Mcgraw-hill Book Company (UK) Limited, 1980.

[21] S. Pennathur and H. H. L. Kwok, "Equivalent circuit for GaAs CCD," *IEEE Proc. Pt. G*, vol. 140, No. 6, pp. 377-382, 1993.

[22] S. Pennathur, "*Analysis and modeling of charge transport in a GaAs CCD*," M. Sc. Thesis, University of Victoria, 1991.

[23] J. M. Carxes, W. F. Kasonocky, *et al.*, "Drift-aided fringing field in charge-coupled devices," *IEEE J. Solid-state Circuits*, vol. 6, No. 10, pp. 322-326, 1971.

[24] L. Chen, "*Design and Implementation of GaAs CCD/MESFET ICs for Artificial Network Application*," Ph. D Dissertation, University of Vicrtoria, 1995.

[25] D. A. Bryman, M. Constable, *et al.*, "500 MHz Transient Digitizers Based on GaAs CCDs," *TRIUMF Technical Report*, 1997.

[26] B. E. Burke, R. W. Mountain, *et al.*, "An Abuttable CCD Imager for Visible and X-Ray Focal Plane Arrays," *IEEE Trans. Electron Devices*, Vol. 38, No. 5, pp. 1069-1076, 1991.

[27] H. Yamashita, M. Sasaki, *et al.*, "A 2/3-in 2 Million Pixel STACK-CCD HDTV Imager," *IEEE J. Solid-State Circuits*, Vol. 30, No. 8, pp. 881-886, 1995.

[28] J. Hyencek, "Low-Noise and High-Speed Charge Detection in High-Resolution CCD Image Sensors," *IEEE Trans. Electron Devices*, Vol. 44 No. 10, pp. 1679-1688, 1997.

[29] T. Miida, Y. Hasegana, *et al.*, "A CCD Video Delay Line with Charge-Integrating Amplifier," *IEEE J. Solid-State Circuits*, Vol. 26, No. 12, pp. 1915-1919, 1991.

[30] S. M. Szc, "*Physics of Semiconductor Devices*," John Wiley $ Sons, 1981.

[31] A. G. Milnes, "*Deep Impurities in Semiconductors*," John Wiley & Sons, 1973.

[32] G. F. Knoll, "*Radiation Detection and Measurement (Second Edition),*" John Wiley & Sons, 1979.

[33] S. Patten, "*A Gallium Arsenide CCD X-ray Detector,*"M. Sc. Thesis, Simon Fraser University, 1997.

[34] L. Berlutti, C. Canali, *et al.*, "Gallium Arsenide particle detectors: a study of the active region and charge-collection efficiency," *Nucl. Instr. and Meth. in Phys. Res.* A 354, pp. 364-367, 1995.

[35] J. E. Eberhardt, R. D. Ryan, *et al.*, "Evaluation of epitaxial n-GaAs for unclear radiation detection," *Nucl. Instr. and Meth.* 94, pp. 463-476, 1971.

[36] M. O. Krause, "Atomic radiative and radiationless yields for K and L shells," *J. Phys. chem. Ref. Data*, Vol. 8, pp. 307, 1979.

[37] H. A. Bethe and J. Ashkin, "*Experimental Nuclear Physics*," John Wiley, 1953.

[38] M. J. Berger and S. M. Seltzer, "Additional stopping power and range tables for protons, sensors and electrons," *Nat. Acad. Sci. - Nat. Res. Council Publ.* No. 1133, pp. 205, 1964.

[39] T. E. Everhart and P. H. Hoff, "Determination of Kilovolt Electron Energy Dissipation vs Penetration Distance in Solid Materials," *J. App. Phys.*, Vol. 42, No. 13, pp. 5837-5846, 1971.

[40] G. C. Messenger, "Collection of Charge on Junction Nodes from Ion Tracks," *IEEE Trans. Uncl. Sc.* Vol. NS-29, No. 6, pp. 2024-2031, 1982.

[41] Mckelvey, "*Solid-State and Semiconductor Physics,*" Harper and Row, 1966.

[42] G. R. Hopkinson, "Analytic modeling of charge diffusion in charge-coupled-device imagers," *Optical Engineering*, Vol. 26, No. 8, pp. 766-772, 1987.

[43] J. R. Janesick, T. Elliott, *et al.*, "CCD advances for X-ray scientific measurement in 1985," *Proc. SPIE*, Vol. 597, pp. 364-372, 1985.

[44] R. W. Brodersen and S. P. Emmons, "Noise in Buried Channel Charge-Coupled Devices," *IEEE J. Solid-State Circuits,* Vol. SC-11, No. 1, pp. 147-155, 1976.

[45] J. Hynecek, "Spectral Analysis of Reset Noise Observed in CCD Charge-Detection Circuits," *IEEE Trans. Electron Devices*, Vol. 37, No. 3, pp. 640-647, 1990.

[46] Edited by R. Melen and D. Buss, "*Charge-Coupled Device: Technology and Applications*," IEEE Press, 1977.

[47] A. van der Ziel, "*Noise in Solid State Devices and Circuits,*" John Wiley & Sons, 1986.

[48] J. Hynecek, "Theoretical Analysis and Optimization of CDS Signal Processing Method for CCD Image Sensors," *IEEE Trans. Electron Devices*, Vol. 39, No. 11 pp. 2497-2507, 1992.

[49] A. B. Grebene, "*Bipolar and MOS analog integrated circuits design,*" John Wiley & Sons, 1984.

[50] K. Aizawa, H. Ohno, *et al.*, "On Sensor Image Compression," *IEEE Trans. Circuits and Sys for Video Tech.* Vol. 7, No. 3, pp. 543-548, 1997.

[51] K. Aizawa, Y. Egi, *et al.*, "Computational Image Sensor for on Sensor Compression," *IEEE Trans. Electron Devices*, Vol. 44, No. 10, 1997.

[52] F. W. Mounts, "A Video Encoding System with Conditional Picture-Element Replenishment," *Bell Sys. Tech. J.* pp. 2545-2554, 1969.

[53] Z. Wang, "*Pixel Compression for Integrated Image Sensor Array,*" M.A.Sc. thesis (to be submitted), University of Victoria, 1999

[54] R. J. Baker, H. W. Li, *et al.*, "*CMOS Circuit Design, Layout, and Simulation,*" IEEE Press, 1997.

[55] M. Li, "*The application of current mode circuits in the design of an A/D converter,*" M.A.Sc. thesis, University of Victoria, 1997.

[56] N. H. E. Weste and K. Eshraghian, "*Principles of CMOS VLSI Design,*" Addison-Wesley Publishing Company, 1993.

[57] Edited by D. E. Newbury, "*Advanced Scanning Electron Microscopy and X-ray Microanalysis,*" Plenum, 1986.

Appendix A

Equivalent Circuit Model of RGCCD in SPICE

Following is the SPICE code for the equivalent circuit model of an unit cell of the RGCCD. The model is actually defined in SPICE as a subcircuit and one pixel of the RGCCD consists of a number of such unit cells.

```
******ccd equivalent circuit******

.subckt ccdcell 1 2 201 202 k1

v1 1 101 0

b1a 101 0 v=v(201)*(1-1e14*v(201))/(0.579675e-15)

b1b 0 201 i=i(v1)

c1 201 0 1

b1x j1 0 v=4.77e7*exp((-1)*sqrt(v(k1)^2+(1e-40))/1644)

+       +3.24e7/(1+(sqrt(v(k1)^2+(1e-30))/130.5)^0.32)

b1u l1 0 v=5000/sqrt(1+(5000*v(k1)/v(j1))^2)

b1z m1 0 v=129.5

+       +312*exp(-1*(ln(sqrt(v(k1)^2+(1e-30))/3394.8)/ln(1.82))^2)

b1c 1 2 i=4e4*v(l1)*v(k1)*v(201)

b1d 1 2 i=16e8*v(l1)*v(101)*(v(201)-v(202))

b1e 1 2 i=16e8*v(m1)*(v(201)-v(202))

.ends ccdcell
```

```
vin 10 0 pulse(0.2 0.8 0 0 0 30n 80n)

vid 4 0 pulse(0 1 0 0 0 50p 650p)

vphase1 1 0 pulse(0 1 50p 0 0 200p 650p)

vphase2 2 0 pulse(0 1 250p 0 0 200p 650p)

vphase3 3 0 pulse(0 1 450p 0 0 200p 650p)

******input stage******

bis 0 1001 i=v(10)*v(4)

s01 1001 1003 4 0 sm

s02 1003 0 2 0 sm

c0 1003 0 50p

binput 1003 10001 i=v(1003)*v(1)


******transport segment in ccd******

bkx1 20001 0 v=1.8174e3*(v(1)-v(10))

x1 10001 10002 201 202 20001 ccdcell

cout 10002 0 20.4f

v202 202 0 1

.model sm sw vt=250m ron=0.0001

.options abstol=1e-40 vntol=1e-40 chgtol=1e-40 gmin=1e-50

.tran 0.1p 1300p

.end
```

Appendix B

Escape of Photo-electrons

The length of the depletion region in the GaAs RGCCD is 11 μm. If we assume all the electrons in the this region will be collected and all the electrons in the FFR will not be collected, we can calculated the chance of escape of photo-electrons with different energy and different incident angle using Monte-Carlo simulation.

Figure 4.4 shows the mean path length for an electron in GaAs. For a 10 KeV electron in GaAs, the mean path length is about 1 μm. The chance of escape of an electron of this energy from the GaAs RGCCD X-ray detector is very small if the electron starts more than 1 μm from the edge of the depletion region. However, for a 50 KeV electron, the mean path length is about 14 μm, the electron will always easily to pass through the depletion region and escape. Therefore, the chance of escape of a high energy photo-electron from the RGCCD X-ray detector must be taken in account.

A Monte-Carlo simulation was done to model the escape of the photo-electrons. The simulation used Equation (4.3) to find the path length of the electron. The path length was then divided up into 50 equal segments, and an elastic scattering event was generated for each of these segments [57]. The X-ray incident positions are chosen randomly along the GaAs RGCCD and 1000 electron paths are simulated. The simulation was done by using MATLAB code. Figure B.1 shows the five typical tracks when the incident angle is π/4. Table B.1 and B.2 list the simulation results.

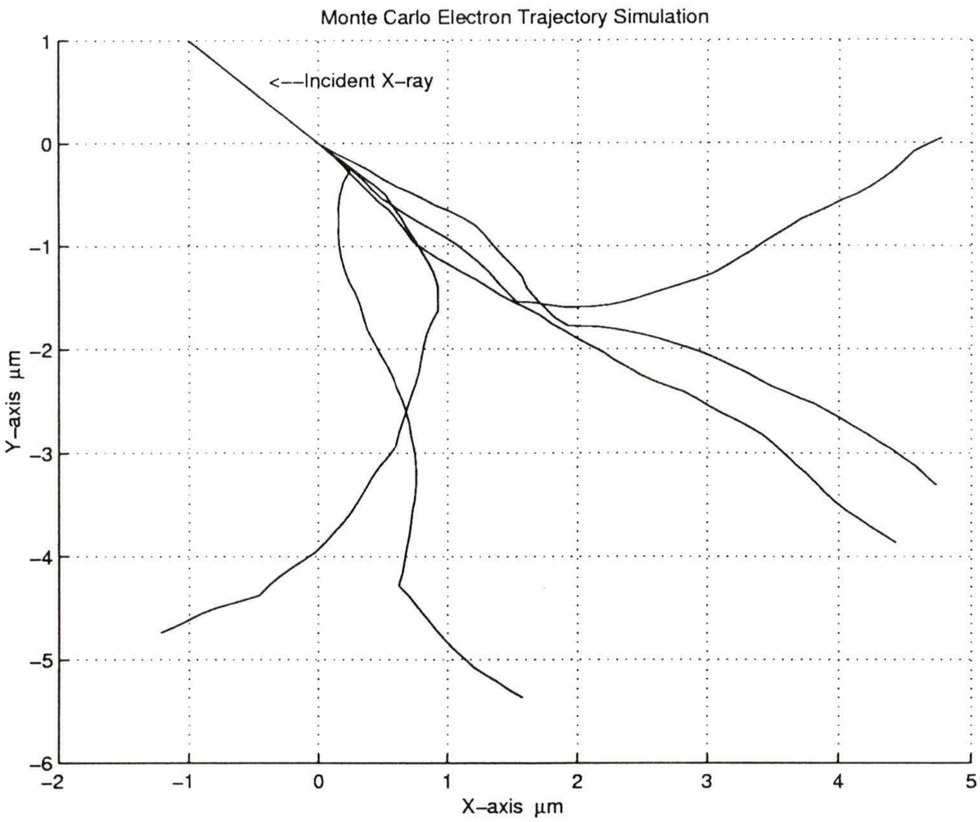

Figure B.1 Five typical electron tracks created by the Monte Carlo simulation when the incident angle is p/4. The energy of photo-electron is 30 KeV

Table B.1. Chance of escape of photo-electrons in the GaAs RGCCD for various electron energies when X-ray incident normal to the surface

Photo-electron energy (KeV)	10	20	30	40	50
Chance of escape (%)	5	5	7	10.6	60

Table B.2. Chance of escape of photo-electrons in the GaAs RGCCD for various electron energies when X-ray incident angle is π/4

Photo-electron energy (KeV)	10	20	30	40	50
Chance of escape (%)	7	8	10.5	12	36.4

From the simulation results we can see that, when the electron energy below 40 KeV, the chance of escape of photo-electron is smaller when the X-ray is incident normal to the surface. It is because the mean path length of the electron with an energy below 40 KeV is within 10 μm, therefore all the electron travel in the GaAs RGCCD are in the depletion region and the only chance of the escape of the photo-electron is through the surface of the detector. Therefore, the bigger the incident angle of the X-ray, the more chance of the escape of the photo-electron. On the other hand, for the electron with an energy of 50 KeV, the chance of escape is much lower when the incident angle is π/4. When the electron energy is 50 KeV, the mean path length is about 14 μm which is longer than the length of depletion region (about 11 μm). Therefore, the penetration of the depletion region is the main chance for the electron to escape. When the X-ray is incident normal to the surface of the detector, most of the photo-electron will pass through the depletion region and escape from the detector. When increase the angle of the incident X-ray, the length required to pass the depletion region becomes longer, therefore, the chance of escape is lower.

VITA

Surname: Hu Given Name: Shengli

Place of Birth: Xi'an, Shaanxi, P. R. China

Educational Institutions Attended:

University of Victoria	1997-1999
University of Electronic Science and Technology of China	1991-1994
Xi'an Jiaotong University	1987-1991

Degree Awarded:

M. Eng.	University of Electronic Science and Technology of China	1994
B. E.	Xi'an Jiaotong University	1991

Honors and Awards:

Victoria Canada-China Friendship Association Scholarship	1997
University of Victoria Research Assistantship	1998-1999
University of Victoria Graduate Teaching Fellowship	1997-1999
University of Electronic Science and Technology of China Scholarship	1991-1994
Xi'an Jiaotong University Scholarship	1987-1991

Publications:

B. Jiang, S. Hu, *et al.*, "Study on composite PTC thermistor", *J. UESTC*, vol. 23, no. 5, 1994

Partial Copyright License

I hereby grant the right to lend my thesis (or dissertation) to users of the University of Victoria Library, and to make single copies only for such users or in response to a request from the Library of any other university, or similar institution, on its behalf or for one of its users. I further agree that permission for extensive copying of this thesis for scholarly purposes may be granted by me or a member of the University designated by me. It is understood that copying or publication of this thesis for financial gain shall not be allowed without my written permission.

Title of Thesis/Dissertation: **A Study of High-speed GaAs CCDs and Their Potential Application as an Imager**

Author [redacted]

(Signature)

Shengli Hu

April 12, 1999

(Date)